

© 2019 by Daniel Twiss

HIGH LIFT CONFIGURATION OF A
SLOTTED NATURAL LAMINAR FLOW AIRFOIL

BY

DANIEL C. TWISS

THESIS

Submitted in partial fulfillment of the requirements
for the degree of Master of Science in Aerospace Engineering
in the Graduate College of the
University of Illinois at Urbana-Champaign, 2019

Urbana, Illinois

Adviser:

Assistant Professor Phillip J. Ansell

Abstract

Experiments were performed on a slotted natural laminar flow airfoil, the S414. The slotted natural laminar flow airfoil concept was developed to satisfy design constraints of high maximum lift and low profile drag. A two-element natural laminar flow configuration allows the typical rapid trailing-edge pressure recovery associated with NLF airfoils to be greatly reduced on the fore element, allowing for laminar flow across the entire airfoil upper surface. The slot provides a favorable injection of momentum to the flow over the aft-element upper surface, improving lift generation. However, an unfortunate side effect of the S414 is an abrupt, leading-edge stall type. This investigation focused on the development of a high-lift configuration of the S414 by altering the position of the aft element in order to characterize the feasibility of utilizing the aft element as a high-lift device.

Computational analysis was performed on the S414 to determine suitable aft-element positions for high lift. Two basic repositioning approaches were used; one that deflected the aft element to increase the airfoil camber while maintaining the slot width of the original airfoil, and one that targeted the utilization of the fore-element dumping velocity. In addition, a plain flap was incorporated into the aft element. Performance predictions for the new aft-element configurations were generated using the computational flow solver MSES, and four alternative aft-element riggings were selected for experimental testing. Tests were performed in the University of Illinois 2.8 ft \times 4 ft wind tunnel at $Re = 1.8 \times 10^6$, $M = 0.18$. Using knowledge gained from the experimental tests, a fifth, empirically-derived configuration was developed. Both computational and experimental results indicated that effective utilization of the fore-element dumping velocity results in the largest increase in C_l . Orienting the aft element such that the flow off the fore element was discharged into a region of low pressure over the aft-element upper surface reduced the pressure recovery requirements at the fore-element trailing edge, allowing for enhanced lift production. In addition, a momentum injection was provided to the flow over the aft-element upper surface, promoting increased lift generation by the aft element as well. These techniques coupled with the deflection of the aft-element plain flap resulted in a 34% increase in $C_{l,max}$.

Acknowledgements

I cannot thank my advisor, Dr. Phil Ansell, enough for his mentorship and assistance throughout this study. The completion of this project would not have been possible without his guidance. He has taught me not just about experimental aerodynamics, but also about leadership and dedication, and has been an ideal role model for me. I would also like to thank Dr. Kenneth Van Treuren, my undergraduate advisor, for providing my first exposure to aerodynamics research, and patiently fielding all my aerospace-related questions.

I also want to thank my family for their love and support while I was away at graduate school, particularly my parents. They encouraged me from a young age to explore what I was passionate about and raised me into the person I am today. I wish to thank Mallory Hightower as well, for her invaluable advice and support when I needed it most.

Finally, I wish to thank all my office mates and friends that I made during my time at Illinois. Chris Colletti, for the long hours spent working with me on design and wind tunnel testing; Rohit Gupta and Georgi Hristov, for selflessly lending me their expertise and assistance any time I needed it, as well as the countless stimulating conversations; Armando Collazo, for his knowledge on all things horological and aeronautical; and Ignacio Andreu, for being an excellent ambassador to Spain as well as a decent sports partner. My friends have made my experience in graduate school something I will always remember with great fondness.

This work was supported by NASA University Leadership Initiative contract #NNX17AJ95A “Advanced Aerodynamic Design Center for Ultra-Efficient Commercial Vehicles.” I wish to thank James Coder of the University of Tennessee, Knoxville for helpful interactions, and Koushik Datta from NASA Research Park at Ames Research Center for serving as the Technical Monitor for the ULI program.

To God be the glory

Table of Contents

List of Figures	vii
List of Tables	x
Nomenclature	xi
Chapter 1: Introduction	1
1.1 Literature Review	1
1.2 Research Motivation and Objectives	3
1.3 Chapter 1 Figure	4
Chapter 2: Computational and Experimental Methods	5
2.1 Theoretical Analysis	5
2.2 MSES	7
2.2.1 MSES Solution Methods	7
2.2.2 Input Files	10
2.2.2.1 Airfoil Coordinates	10
2.2.2.2 MSES Run File	10
2.2.2.3 Polar Sweep Parameters	10
2.2.3 Execution of MSES and its Associated Programs	11
2.2.3.1 AIRSET	11
2.2.3.2 MSET	11
2.2.3.3 MSES and MSIS	11
2.2.3.4 MPLOT	12
2.2.3.5 MPOLAR	12
2.3 Aerodynamic Testing Environment	13
2.3.1 Wind Tunnel	13
2.3.2 Airfoil Model	15
2.3.3 Wake Survey System	17
2.3.4 Vacuum Suction System	17
2.4 Data Acquisition	18
2.4.1 Pressure Measurements	19
2.5 Airfoil Performance	20
2.5.1 Airfoil Performance from Surface Pressure Measurements	20
2.5.1.1 Surface Pressure Coefficient (C_p)	20
2.5.1.2 Airfoil Lift and Pitching Moment Coefficients	21

2.5.1.3 Drag Calculation from Wake Pressures	23
2.6 Airfoil Model Diagnostics	25
2.6.1 Fluorescent Oil Surface Flow Visualization	25
2.7 Wind Tunnel Corrections.....	25
2.8 Chapter 2 Tables and Figures	28
Chapter 3: Results and Discussion.....	37
3.1 Theoretical Results.....	37
3.1.1 S414 Theoretical Characterization.....	37
3.1.2 Slot-Based Approach	38
3.1.3 Dumping Velocity-Based Approach.....	38
3.1.4 Expanded Dumping Velocity-Based Approach.....	39
3.2 Selection of Aft Element Positions for Experimental Testing.....	40
3.3 Sidewall Suction System.....	41
3.4 Experimental Validation of the S414 Airfoil Model	42
3.5 Alternative Aft Element Rigging Experiments.....	44
3.5.1 Baseline Case	45
3.5.2 Case 1	47
3.5.3 Case 2.....	47
3.5.4 Case 3.....	48
3.5.5 Case 4.....	48
3.5.5 Case 5.....	49
3.6 Chapter 3 Tables and Figures	50
Chapter 4: Summary and Conclusions.....	74
Chapter 5: Uncertainty Analysis.....	76
5.1 Uncertainty in Performance Measurements	77
5.1.1 Uncertainty in Flow Conditions.....	77
5.1.2 Uncertainty in Pressure and Performance Coefficients	78
5.1.3 Chapter 5 Tables	79
Appendix A: Additional MSES Material.....	80
A.1 Sample Input/Run Files.....	80
A.2 MSES Tips	81
A.3 Appendix A Tables and Figures.....	83
References.....	88

List of Figures

Fig. 1.1 The S414 airfoil, after Coder et al. ¹²	4
Fig. 2.1 Sample aft element positions for the slot-based repositioning approach.	29
Fig. 2.2 Sample aft element positions for the dumping velocity based-repositioning approach. .	29
Fig. 2.3 Sample aft element positions for the expanded dumping velocity-based repositioning approach.	29
Fig. 2.4 Sample MSES grid for the S414 generated using MSET.....	30
Fig. 2.5 Schematic of the University of Illinois 2.8-ft × 4-ft subsonic wind tunnel.	30
Fig. 2.6 S414 geometry demonstrating spar locations, the aft element plain flap, and the 3D printed fore element trailing-edge.....	31
Fig. 2.7 Exploded view of the S414 airfoil model. Aluminum parts are depicted in light gray, steel spars in dark gray, and the 3D printed parts in gold.	31
Fig. 2.8 The S414 airfoil model installed in the wind tunnel test section.....	32
Fig. 2.9 Inserts used to set the alternate aft element locations. From top left: Case 1, Case 2, Case 3, Case 4, Case 5.	33
Fig. 2.10 Wake rake installed in the test section downstream of the S414 airfoil model.	34
Fig. 2.11 Custom turntable with holes configured to provide sidewall suction.	35
Fig. 2.12 Vacuum suction system with ducting attached to the plenum boxes on the top and bottom of the test section.	36
Fig. 3.1 Theoretical performance predictions generated by MSES at $Re = 1.5 \times 10^6$, $M = 0.17$	50
Fig. 3.2 MSES results for the slot-based approach at $Re = 1.5 \times 10^6$, $M = 0.17$, $\delta_f = 0^\circ$	51
Fig. 3.3 MSES results for the slot-based approach for a) $\delta_f = 5^\circ$ and b) $\delta_f = 10^\circ$ at $Re = 1.5 \times 10^6$, $M = 0.17$	52
Fig. 3.4 MSES results for the dumping velocity-based approach at $Re = 1.5 \times 10^6$, $M = 0.17$, $\delta_f = 0^\circ$	53
Fig. 3.5 MSES results for the dumping velocity-based approach for a) $\delta_f = 5^\circ$ and b) $\delta_f = 10^\circ$ at $Re = 1.5 \times 10^6$, $M = 0.17$	54
Fig. 3.6 Sample C_l contour map generated using the expanded dumping-velocity approach that demonstrates how regions of high performance were iteratively identified.....	55
Fig. 3.7 Sample aft-element effectiveness plot generated by the expanded dumping-velocity approach.....	55

Fig. 3.8 Alternate positions for the S414 aft element.	56
Fig. 3.9 Aft element spanwise pressure distributions for various VFD operating frequencies for a) $\alpha = 5^\circ$ and b) $\alpha = 15^\circ$ at $Re = 1.8 \times 10^6$, $M = 0.18$	57
Fig. 3.10 Lift-curve comparison with the suction system on (VFD at 45 Hz) and off at $Re = 1.0 \times 10^6$, $M = 0.10$	58
Fig. 3.11 C_p comparison with the suction system on (VFD at 45 Hz) and off at $Re = 1.0 \times 10^6$, $M = 0.10$	58
Fig. 3.12 Comparison of S414 performance data from the current study to Somers & Maughmer ² and MSES 3.05 ³ at $Re = 1.0 \times 10^6$, $M = 0.10$	59
Fig. 3.13 Comparison of S414 C_p data from the current study to Somers & Maughmer ² and MSES 3.05 ³ for a) $\alpha = 0^\circ$, b) $\alpha = 5^\circ$, c) $\alpha = 10^\circ$, d) $\alpha = 15^\circ$ at $Re = 1.0 \times 10^6$, $M = 0.10$	60
Fig. 3.14 Surface oil flow visualization and the corresponding C_p distribution for $\alpha = 3^\circ$ at $Re = 1.0 \times 10^6$, $M = 0.10$	62
Fig. 3.15 Performance of the S414 airfoil model at $Re = 1.8 \times 10^6$, $M = 0.18$	63
Fig. 3.16 Effect of deflecting the aft element plain flap on C_l at $Re = 1.8 \times 10^6$, $M = 0.18$	63
Fig. 3.17 C_p distributions for the S414 at various angles of attack at $Re = 1.8 \times 10^6$, $M = 0.18$	64
Fig. 3.18 Surface oil flow visualization and the corresponding C_p distribution for $\alpha = 0^\circ$ at $Re = 1.8 \times 10^6$, $M = 0.18$	65
Fig. 3.19 Surface oil flow visualization and the corresponding C_p distribution for $\alpha = 15^\circ$ at $Re = 1.8 \times 10^6$, $M = 0.18$	66
Fig. 3.20 Performance comparison between the S414 airfoil and the Case 1 rigging at $Re = 1.8 \times 10^6$, $M = 0.18$	67
Fig. 3.21 Performance comparison between the S414 airfoil and the Case 2 rigging at $Re = 1.8 \times 10^6$, $M = 0.18$	68
Fig. 3.22 Performance comparison between the S414 airfoil and the Case 3 rigging at $Re = 1.8 \times 10^6$, $M = 0.18$	69
Fig. 3.23 Performance comparison between the S414 airfoil and the Case 4 rigging at $Re = 1.8 \times 10^6$, $M = 0.18$	70
Fig. 3.24 Performance comparison between the S414 airfoil and the Case 5 rigging at $Re = 1.8 \times 10^6$, $M = 0.18$	71

Fig. 3.25 Performance between the S414 and the alternate rigging cases for $\delta_f = 0^\circ$ at $\text{Re} = 1.8 \times 10^6$, $M = 0.18$	72
Fig. 3.26 Performance between the S414 and the alternate rigging cases for $\delta_f = 20^\circ$ at $\text{Re} = 1.8 \times 10^6$, $M = 0.18$	73
Fig. A.1 Annotated MSET run file used to automate grid generation and MSES set up.	83
Fig. A.2 Grid parameter file generated using MSET.....	84
Fig. A.3 Sample mses.XXX input file containing example boundary conditions.....	85
Fig. A.4 Annotated run file used to execute the flow solver MSES.....	85
Fig. A.5 Sample spec.XXX input file used to specify parameter to sweep over in MPOLAR....	86
Fig. A.6 Sample polar.XXX file containing results from polar sweep program MPOLAR.....	87

List of Tables

Table 2.1 Surface pressure tap locations on the S414 airfoil model.....	28
Table 3.1 Alternate aft-element positions compared to the gap (x/c), overhang (x/c), and aft-element deflection angle ($^\circ$) of the S414.	56
Table 5.1 Example uncertainties for the test conditions of the S414 airfoil model experiments at $Re = 1.8 \times 10^6$ and $\alpha = 5^\circ$	79
Table 5.2 Example uncertainties for the airfoil pressure and performance coefficients of the S414 airfoil model experiments at $Re = 1.8 \times 10^6$ and $\alpha = 5^\circ$	79

Nomenclature

List of Symbols

α	airfoil angle of attack
α_{stall}	airfoil stall angle of attack
α_{zL}	airfoil zero-lift angle of attack
A_{ss}	cross-section area of the wind tunnel settling section
A_{ts}	cross-section area of the wind tunnel test section
b	span of the airfoil model
c	airfoil chord length
c_p	specific heat capacity
C_a	coefficient of axial force
C_d	airfoil drag coefficient
$C_{d,min}$	airfoil minimum drag coefficient
C_l	airfoil lift coefficient
$C_{l,\alpha}$	airfoil lift-curve slope
$C_{l,max}$	airfoil maximum lift coefficient
C_m	airfoil quarter-chord pitching moment coefficient
$C_{m,LE}$	airfoil pitching moment coefficient about the leading edge
C_n	coefficient of normal force
C_p	airfoil surface pressure coefficient
$C_{p,min}$	minimum airfoil surface pressure coefficient
δ_{aft}	airfoil aft-element deflection angle
δ_f	airfoil aft-element plain-flap deflection angle
D'	airfoil sectional drag
ε	tunnel blockage velocity increment factor
F	aerodynamic forces
h	test section height or enthalpy
h_t	stagnation enthalpy
k	thermal conductivity
μ	dynamic viscosity

\dot{m}	mass flow rate
M	Mach number
\hat{n}	normal unit vector
p_e	pressure at the edge of the boundary layer
P	static pressure
P_o	total pressure
Pr	Prandtl number
q	dynamic pressure
ρ	density
R	universal gas constant
Re	chord-based Reynolds number
σ	streamline curvature compensation factor
S	airfoil reference area
t	airfoil thickness
T	static temperature
T_u	turbulence intensity
U	velocity or uncertainty
V_m	volume of the airfoil model
x	airfoil chordwise direction
y	airfoil chord-normal direction
z	airfoil spanwise direction

List of Abbreviations

AFC	active flow control
CFM	cubic feet per minute
DTC	digital temperature compensation
LSB	laminar separation bubble
NLF	natural laminar flow
SLA	stereolithography
SNLF	slotted natural laminar flow
VFD	variable frequency drive

Chapter 1

Introduction

Rising oil prices, economic recessions, and the perpetual desire for increased profitability have motivated aircraft manufacturers to explore various methods to reduce operational costs of aviation as greatly as possible. One such method involves the reduction of drag during cruise. It has been found that for transport aircraft, wing profile drag contributes to roughly 1/3 of the total drag¹, thus investigating ways to reduce wing profile drag during cruise warrants exploration. There are several techniques for reducing wing profile drag, namely, the utilization of natural laminar flow (NLF) airfoils, improving the efficiency and decreasing the weight of high-lift systems, and incorporating laminar flow control². While it has been demonstrated that the incorporation of such flow control systems can decrease profile drag by up to 75%, the present study focuses primarily on natural laminar flow and the use of a high-lift system.

1.1 Literature Review

NLF airfoils exploit the lower skin friction produced by laminar-flow boundary layers as compared to turbulent flows. Through tailoring of the airfoil geometry, and the pressure distribution as a result, it is possible to extend the laminar flow portion of the airfoil up to ~70% of the airfoil chord, which is limited by the pressure recovery gradient³. The remaining chord is typically used for a rapid, concave-type pressure recovery, which allows the external potential

flow region to be decelerated to freestream values across shorter distances. Previous studies have shown the use of increased laminar flow to be capable of producing drag reductions of up to 50% over conventional designs^{1,3}. However, one side effect of NLF airfoils is the tendency to separate early as a result of the strong adverse pressure gradient at high angles of attack required to satisfy the rapid pressure recovery requirements. The consequence of such tendencies is rapid stall and a reduction in $C_{l,max}$. Another negative aspect of NLF airfoils is the effect of leading edge contamination, such as fouling from insects or environmental debris, resulting in premature transition and separation, which in turn leads to potentially dangerous takeoff and landing conditions⁴. Additionally, the application of NLF airfoils is limited by wing sweep as the corresponding crossflow instability typically causes early transition⁵.

In addition to NLF airfoils, high-lift systems also work to reduce profile drag during cruise by providing additional lift at low speeds, allowing wing surfaces to have a smaller wetted area when high-lift systems are stowed during cruise. Typically, high lift is accomplished through the implementation of different combinations and types of slats and flaps. From a simplified perspective, slats work to reduce negative pressure peaks at the leading edge in order to delay boundary layer separation while flaps act to increase $C_{l,max}$ by increasing the camber of the airfoil. Deployable flaps that act as separate individual elements, such as a Fowler flap, can also increase the circulation about the main element and thus the total lift generated by the multielement airfoil. The aft element circulation effectively places the trailing edge of the fore element at a higher angle of attack. For the Kutta Condition to be met, the circulation of the fore element must increase, resulting in increased lift. The aft element circulation also causes the velocity of the flow off the trailing edge of the fore element (known as the dumping velocity) to be increased. This, in turn, reduces the pressure recovery load on the fore element, which can be performed much more rapidly in the fore-element wake. The primary functions of multielement high-lift airfoils are described in detail in the classic publication by A.M.O. Smith⁶. These techniques have the ability to decrease wing profile drag by up to 50% as compared to airfoils without high-lift systems^{1,3}. In addition, reducing the complexity of high-lift systems can lead to substantial reductions in aircraft weight and, as a result, reduced drag. A study by Rudolph et al.⁷ demonstrated that a reduction in high-lift system weight scales to aircraft weight reduction by a factor of 1.5 to 2.5. This benefit of simplifying high-lift systems can be seen through the historical shift towards fewer individual high-lift elements and simpler actuation methods. This gradual change can be observed, for

example, by comparing the triple-slotted flap system utilized on both the inboard and outboard flap sections for the early Boeing 747-100 aircraft, to the inboard double-slotted and outboard single-slotted flaps used on the modern Boeing 747-8. As such, maintaining a highly-efficient, yet lightweight high-lift system is highly desirable for the integration of modern airfoil concepts into new aircraft designs.

In an attempt to utilize the drag reductions of NLF with increasing high-lift capabilities, a slotted natural laminar flow (SNLF) airfoil was designed by Somers⁸, dubbed the S414. The Eppler Design and Analysis Code^{9,10} was used to create the initial airfoil shapes and MSES¹¹ was used to refine them. During the initial design phase, constraints were placed on the $C_{l,max}$ produced by the airfoil, such as it not differing significantly with fixed transition at the leading edge. Additionally, a docile stall process was desired. The result was a 14.22% thick, multielement SNLF airfoil intended for rotorcraft use. The aft element allows the fore element to maintain laminar flow across its entire surface at design conditions, resulting in large reductions in drag. The aft element is also capable of significant portions of laminar flow because the fore element wake does not obtrude upon it. The S414 was tested theoretically and validated experimentally by Coder et al.¹² at the Pennsylvania State University Low-Speed, Low-Turbulence Wind Tunnel. A rendering of the S414 airfoil is shown in Fig. 1.1, after Coder et al.¹². All constraints were satisfied except the stall characteristic, which was found to be quite aggressive⁸.

Maughmer et al.¹³ performed a study investigating interactions between the S414 fore and aft element. In order to ascertain the feasibility and practicality of using the S414 aft element as a control surface and/or a high-lift system, the aft element was translated and rotated. In addition, a tab was extended from the aft element trailing edge to simulate the effects of a simple flap. It was found that rotating the aft element resulted in large increases in profile drag with minimal effect on $C_{l,max}$. Translating the aft element yielded similar results. When the aft element was translated and rotated simultaneously, $C_{l,max}$ increased. However, the addition of the tab provided the greatest increase in high-lift performance, with a significant increase in $C_{l,max}$ without unacceptable increases in drag.

1.2 Research Motivation and Objectives

Previous studies on the S414 airfoil have focused on analyzing performance computationally and characterizing the experimental behavior at low speeds. Very little work has

been done on the utilization of the S414 aft element as an unconstrained high-lift device. The abrupt stall characteristic of the S414 further necessitates this study, as the use of the aft element for high-lift generation reduces the geometric complexity required for satisfactory high-lift performance. As such, during future development of SNLF airfoil concepts, the abrupt stall issues typical of SNLF can be addressed during the design phase, with the knowledge that high-lift may be achieved through actuation of the aft element rather than the airfoil geometry. Furthermore, previous investigations involving manipulation of the aft-element position primarily involved a parametric approach, with little prior knowledge of the performance of each alternative position before testing. Instead, this study focuses on the design of a high-lift configuration of the S414, in which computational methods and physics-based aft-element positioning schemes are employed to analytically determine effective aft element positions. In addition, a greater understanding of the physics governing the interactions between the S414 fore and aft element is anticipated through this approach. Finally, the performance effects of fully integrating a plain flap into the aft-element trailing edge has yet to be studied thoroughly. Thus, the primary objectives for the current investigation can be summarized as follows:

- Understand the governing physics behind the flow interactions between the fore and aft element.
- Design and test alternative aft element positions for high lift.
- Investigate the effects of integrating a plain flap into the aft element trailing edge.

1.3 Chapter 1 Figure



Fig. 1.1 The S414 airfoil, after Coder et al.¹²

Chapter 2

Computational and Experimental Methods

This chapter details the computational methods, experimental methods, test equipment, and facilities used throughout this investigation. It describes in detail the computational systems, programs, and routines, as well as the experimental setup, measurement systems, data acquisition practices, and data reduction techniques.

2.1 Theoretical Analysis

As mentioned previously, the primary objective of this study was to create a high-lift configuration of the S414 airfoil by identifying alternative aft element positions that result in large amounts of lift generation. Aft element repositioning schemes were coupled with low order simulations to quickly develop and analyze the performance of these alternative aft element riggings. All theoretical analysis was performed using the airfoil analysis tool and flow solver MSES¹⁴, discussed in detail below.

Variation of the aft element rigging for high lift presented a four degree of freedom (DOF) problem, as the aft element gap, overhang, deflection angle (δ_{aft}), and plain flap deflection angle were all unconstrained. A physics-based approach was used to constrain these studies and reduce the number of variables required to survey the design space. The primary physical parameters of interest were the fore element dumping velocity and the slot geometry, as they were found to have the greatest impact on the airfoil system performance at high angles of attack. In order to analyze various aft element riggings, several programs were developed using MATLAB as a shell to

interface with MSES, allowing for rapid evaluation of a large parametric space. These programs used various repositioning schemes to create new aft element riggings, then analyzed the new geometry performance using MSES.

The first approach to reconfiguring the aft element position was to exploit the slot feature of the S414. The aft element in its nested configuration is positioned such that a constant gap is maintained between the upper surface of the aft element and the cove of the fore element. A program was written that rotates and translates the aft element such that this nested gap is preserved. As discussed by Pfeiffer¹⁵, rotating the aft element such that the design slot width is preserved allows the circulation about the aft element to be increased while minimizing the negative effects of altering the optimized slot geometry. For the current study, this was done by taking advantage of the circular nature of the aft element upper surface. This circular-arc slot provided an ideal tradeoff between modified slot width and curvature, as discussed by Whitcomb¹⁶. A circle fit was calculated from the aft element coordinates, such that the radius and center of the circle was found. The aft element was then rotated about the center of a circle fit made relative to the surface, as seen in Fig. 2.1, and MSES was executed to generate a C_l vs α polar. The aft element was then rotated again and another polar was created. This process was repeated with aft element flap deflections of $\delta_f = 0^\circ, 5^\circ$ and 10° . The results were then stored and plotted in MATLAB for further study.

The second aft element positioning program was used to investigate the effects of placing the aft element downstream of the fore element such that the flow from the trailing edge of the fore element forms a tangent line with the aft element. This was done by creating a best fit line from the trailing edge of the fore element, then selecting a chord-wise point on the aft element where the tangency condition should be enforced. Next, an iterative rotation matrix was used to find the necessary δ_{aft} for the flow line to be tangent to the aft element flow tangency point. Once the aft element had been properly positioned, MSES was executed to generate a C_l vs α polar. The aft element was then translated along the tangent line and another polar created. This process was repeated with aft element flap deflections $\delta_f = 0^\circ, 5^\circ$ and 10° . The results were stored and plotted in MATLAB. Fig. 2.2 demonstrates this process.

This program was also extended to include positions along a line parallel but offset from the fore element trailing edge flow tangency line. However, in this program the user specifies the desired δ_{aft} , and the necessary flow tangency point is calculated. Once the aft element was aligned

to be tangent with the flow line, it was parametrically swept downstream. In addition, offset flow lines were calculated, and the aft element was swept along those as well. The aft element deflection angle was varied from $\delta_{aft} = 0^\circ$ to $\delta_{aft} = 15^\circ$ at 1° increments. Due to the high number of cases required to cover the full parametric space, the new airfoil geometries were all analyzed at a constant system angle of attack to save time. Once the runs were completed, contours of C_l were created to determine which locations provided the most lift across the δ_{aft} range. In addition, aft element effectiveness plots were created to provide insight into which ranges of aft element deflections were able to retain flow attachment, and at what values nonlinear influences began to dominate. The results were stored and plotted in MATLAB. Fig. 2.3 demonstrates this process, which produced a simple parametric optimization routine for positioning the aft element.

2.2 MSES

The MSES suite of programs is a coupled viscous-inviscid flow solver, written in the Fortran¹⁷ programming language by Drela from MIT, capable of multielement analysis and inverse design¹⁸. It is functionally similar to XFOIL¹⁹, but differs slightly in that it can handle multielement airfoils, gives the user much more control over the flow solving methods, and uses an Euler equation solver instead of a panel method. MSES grants the user direct authority over subroutines and parameters that allow for the modification of global constants, specification of boundary conditions and solution methods, user-controlled grid generation, and much more. The introduction of these added capabilities results in the potential for higher fidelity low order modeling solutions at the risk of higher complexity, reduced robustness, and reduced ease-of-use.

2.2.1 MSES Solution Methods

MSES solves the flow-field by assuming potential flow everywhere except a thin viscous boundary layer. To solve the potential flow region, the Euler equations are solved. The Euler equations for inviscid, steady, flow can be expressed in surface integral form using a control volume approach,

$$\oint \rho(\vec{u} \cdot \hat{n}) ds = 0 \quad (2.1)$$

$$\oint \rho \vec{u}(\vec{u} \cdot \hat{n}) + p \hat{n} ds = 0 \quad (2.2)$$

$$\oint \rho(\vec{u} \cdot \hat{n}) h_t ds = 0 \quad (2.3)$$

where ρ is the density, \vec{u} is the velocity field vector, \hat{n} is a normal unit vector, p is the local pressure acting on the surface, and h_t is the stagnation enthalpy. Eqs. 2.1, 2.2, and 2.3 correspond to the conservation of mass, momentum, and energy, respectively, and are discretized and solved using an intrinsic grid. An intrinsic grid uses a set of coordinate lines as the streamlines around the body and allows the viscous grid and flow solution to be solved simultaneously²⁰.

To solve the viscous boundary layer region of the flow, MSES uses a displacement body model, which assumes that the primary effect of the boundary layer is to displace the inviscid portion of the flow²¹. It then solves the Prandtl boundary layer equations to calculate this viscous region. Assuming steady, 2D flow and applying the perfect gas assumption, the Prandtl boundary layer equations reduce to,

$$\frac{\partial}{\partial x}(\rho u) + \frac{\partial}{\partial y}(\rho v) = 0 \quad (2.4)$$

$$\rho u \frac{\partial u}{\partial x} + \rho v \frac{\partial v}{\partial x} = -\frac{\partial p_e}{\partial x} + \frac{\partial}{\partial y} \left(\mu \frac{\partial u}{\partial y} \right) \quad (2.5)$$

$$\rho u \frac{\partial h}{\partial x} + \rho v \frac{\partial h}{\partial x} = u \frac{\partial p_e}{\partial x} + \frac{\partial}{\partial y} \left(\frac{\mu}{\text{Pr}} \frac{\partial h}{\partial y} \right) + \mu \left(\frac{\partial u}{\partial y} \right)^2 \quad (2.6)$$

where p_e is the pressure at the edge of the boundary layer, μ is the dynamic viscosity, h represents the enthalpy, and Pr is the Prandtl Number²². The Prandtl Number can be calculated using,

$$\text{Pr} = \frac{c_p \mu}{k} \quad (2.7)$$

where c_p is the specific heat, and k is the thermal conductivity. To solve the boundary layer region, MSES integrates Eqs. 2.4, 2.5, and 2.6 from the wall to infinity and assumes an adiabatic freestream with no cross stream pressure variation. In addition, many empirical relations are

applied to the boundary layer solution. For a detailed breakdown of the empirical corrections and derivations, see Ref. 20.

Finally, the solutions are coupled by using the viscous solution as a boundary condition for the inviscid flow. The system is then solved using a multidimensional Newton iteration scheme, which can solve both the viscous and inviscid flow simultaneously. A Newton iteration scheme, or Newton-Raphson method, is an iterative root finding algorithm. It begins by evaluating the system about an initial solution guess, which for MSES is the fully inviscid potential flow-field with no viscous effects, using,

$$x_1 = x_0 - \frac{f(x_0)}{f'(x_0)} \quad (2.8)$$

where x_0 is the initial solution guess, and x_1 is the root of the tangent line of the system at the initial guess. The root x_1 is then used as the next solution guess, and the process is repeated using,

$$x_{n+1} = x_n - \frac{f(x_n)}{f'(x_n)} \quad (2.9)$$

until a tolerance on the solution accuracy is reached. In MSES, the function $f(x)$ contains all the discretized Euler and boundary layer equations, as well as boundary conditions and global constants. An additional benefit of using a Newton-Raphson method is the added speed while performing polars. Once a MSES has converged upon a solution, a nearby solution can be rapidly converged upon due to the quadratic convergence property of the Newton-Raphson method.

MSES predicts transition using the Orr-Sommerfield envelope e^n method²³, also used in XFOIL, or the full frequency tracking e^n transition model²⁴, which solves for the critical Tollmien-Schlichting frequency using the previously discussed Newton solver. The envelope e^n method only tracks whichever frequency is most amplified at a given point on the airfoil surface, rather than tracking the Tollmien-Schlichting waves for many frequencies. The model predicts transition when the integrated amplitude reaches an empirically determined value.²⁵ The envelope e^n method was used for all simulations in the current study.

2.2.2 Input Files

The following sections describe the input files required to run the MSES suite of programs. For further insights into the contents and specifics of the input files, see Ref. 14. Additionally, sample input files used in the current study can be found in Appendix A.

2.2.2.1 Airfoil Coordinates

The execution of the MSES flow solver involves several input files and subroutines. First, an airfoil coordinate file must be created and saved in the proper format. Typically, the coordinate file contains the name of the airfoil on the first line, the estimated size of the required control volume on the second, and then the geometric airfoil coordinates. If it is a multielement airfoil, the coordinates “999 999” serve as a delimiter between two airfoil elements. The proper coordinate file naming convention is “blade.XXX”, where XXX represents the name of the airfoil. However, if no such file is found in the program directory, MSES will search for and open a file saved simply as the name of the airfoil, or in this example “XXX”. A coordinate file is required to run any MSES flow solver.

2.2.2.2 MSES Run File

To run an MSES flow solver, an input file containing run parameters is required. The MSES run file, saved as “mses.XXX”, specifies conditions such as Reynolds number, Mach number, angle of attack, boundary conditions, critical amplification factor, and so on. Proper configuration of the mses.XXX run file is essential for run convergence.

2.2.2.3 Polar Sweep Parameters

To run a polar in MSES, as discussed below, a parameter sweep input file is required. This input file, saved as “spec.XXX”, specifies the parameter to sweep across and lists the values through which the sweep should occur. It is recommended that small increments are used when sweeping between parameter values as smaller jumps allow MSES to take greater advantage of the quadratic convergence of the flow solver being used, which in turn reduces computation time.

2.2.3 Execution of MSES and its Associated Programs

The following sections detail the programs used by MSES to generate and plot a flow solution. For a more in-depth analysis and discussion of the details and techniques used by MSES, see Ref. 14.

2.2.3.1 AIRSET

The airfoil can be edited by a built-in MSES program called AIRSET. Geometric modifications, such as the addition of a simple trailing edge flap, application of a finite trailing edge, translation and rotation of a user-specified airfoil element, and more can all be performed from within AIRSET. Once modifications are complete, AIRSET can write the new airfoil coordinates to a “blade.XXX” file. AIRSET requires an airfoil coordinate input and is run by typing “airset blade.XXX” or “airset XXX” into the terminal.

2.2.3.2 MSET

To prepare MSES for execution, the program MSET, a grid and flow-field initializer, is used. MSET imports the airfoil coordinate file, asks the user to specify the airfoil system angle of attack to run, and then uses a panel solution to generate the stagnation streamlines above and below each airfoil element. Then, the user specifies desired grid node spacing and MSET generates an initial grid. An elliptic grid smoother is then used, and the resulting initialized grid is saved as “mdat.XXX”. MSET requires the airfoil coordinate input file and is run by typing “mset blade.XXX” or “mset XXX” into the terminal.

MSET also allows the user to modify grid parameters to values other than the default, which is where the majority of grid customization and troubleshooting occurs. If a satisfactory grid has been generated by the user, MSET offers the option to save the current grid parameters in a separate optional input file title “gridpar.XXX”. It is also possible to view the fully initialized grid, as well as the inviscid solution to the flow-field (which are one and the same) from within MSET, allowing for visual inspection and alteration of the grid as well. A sample MSES grid can be seen in Fig. 2.4.

2.2.3.3 MSES and MSIS

Once the grid has been initialized using MSET, MSES can be run. MSES is the main program used to generate flow solutions using the methods described previously. The user inputs

how many iterations to run the solver, which serves as an iteration limit that queries the user for another iteration limit if reached without convergence. If MSES converges on a solution before reaching the iteration limit, it will terminate and print “converged on tolerance”, followed by the same iteration limit prompt. After each iteration, the current solution is saved to the mdat.XXX file. In addition, MSES allows the user to coarsen or refine the grid based on user commands. To coarsen the grid x times, enter “ $-n$ ” into the iteration limit prompt. To refine the grid n times, enter “ $+n$ ” into the iteration limit prompt. To exit the MSES program, enter 0 into the iteration limit prompt. MSES requires the airfoil coordinate, mses.XXX, and mdat.XXX files and is run by typing “mSES blade.XXX” or “mSES XXX” into the terminal.

The program MSIS can also be used in an identical manner to generate flow solutions as well. MSIS is functionally equivalent to MSES but replaces a momentum equation with the isentropic flow condition. This allows solutions to be generated much faster, and for predictions to be made at very low Mach numbers ($M \leq 0.001$). However, MSIS can only be run if the entire flow-field remains subsonic.

2.2.3.4 MPLOT

After MSES has converged to plotting accuracy, the program MPLOT can be used as a solution plotter. Using MPLOT, plots of the airfoil performance coefficients, streamlines, wake profiles, and more can all be created and saved. Because MPLOT reads the mdat.XXX file to plot solutions, it can plot results generated using both MSES and MSIS. Note that while it is technically possible to plot solutions that have not converge, such results are physically meaningless and at best should only be used for insight as to how the solution or grid is diverging (though even this is dangerous as the unconverged solutions can be misleading as to how the grid should be modified for higher probability of convergence). MPLOT requires the mdat.XXX input file and is executed by entering “mplot XXX” into the terminal.

2.2.3.5 MPOLAR

In order to easily sweep across a user specified parameter to create a polar, the program MPOLAR can be used. MPOLAR takes full advantage of the quadratic convergence of the Newton-Raphson method to quickly generate and store solutions to a range of airfoil system operating conditions. MPOLAR will automatically subdivide the incremental change in airfoil system operating conditions if a solution is not converged upon at the subsequent operating point

specified in the spec.XXX input file. Once MPOLAR does converge upon a solution, the resulting performance values are output to a polar.XXX file. MPLOT requires all input files necessary to run MSES, as well as the spec.XXX input file and is executed by entering “mpolar XXX” into the terminal.

MPOLIS is functionally equivalent to MPOLAR, but uses MSIS as its flow solver, rather than MSES. To view the resulting polar created by MPOLAR or MPOLIS, the program PLOT can be used. PLOT is able to superimpose multiple polars onto one plot.

2.3 Aerodynamic Testing Environment

2.3.1 Wind Tunnel

All experiments were performed in the Aerodynamics Research Laboratory at the University of Illinois at Urbana-Champaign. The tests were conducted in an open return type, low-speed low-turbulence wind tunnel which had a 2.8 ft × 4 ft rectangular cross section that extended 8 feet in length in the streamwise direction. The cross sectional area of the test section increased linearly downstream in order to reduce the effects of boundary layer growth, allowing the freestream velocity to remain constant through the test section length. The inlet of the wind tunnel contained a four-inch thick honeycomb flow straightener as well as four anti-turbulence screens. This flow preconditioning configuration reduced the empty test section turbulence intensity to less than 0.1%. The contraction area ratio between the between the flow settling section and the upstream end of the wind tunnel was 7.5:1. A schematic of the wind tunnel can be seen in Fig. 2.5.

A five-bladed fan, driven by a regulated 125-horsepower motor, was housed near the end of the tunnel diffuser. Power was provided to the motor via an ABB ACS 800 Low Voltage AC Drive. The maximum empty test section freestream velocity was approximately 165 mph (242 ft/s), which corresponded to a maximum motor setting of 1200 rpm. The chord-based Reynolds number of the airfoil test model was calculated using,

$$\text{Re} = \frac{\rho U_{\infty} c}{\mu} \quad (2.10)$$

where ρ is the air density, U_∞ is test section freestream velocity, c is the airfoil chord, and μ is the dynamic viscosity of the air. The chord-based Reynolds number was computer controlled to within 0.5% of the desired value through an iterative routine during all tests.

The test-section freestream velocity was implicitly determined by measuring the difference in static pressures (ΔP) between the inlet settling section and the test-section inlet ($P_{ss} - P_{ts}$), which was done using a Setra 239 15 in. WC differential pressure transducer. The average settling section static pressure, P_{ss} , was measured using a set of four pressure probes, one on each wall, downstream of the anti-turbulence screen. Similarly, four pressure probes just upstream of the test section, one on each wall, provided an average test section static pressure, P_{ts} . By assuming steady, inviscid, incompressible flow, the law of conservation of mass (Eq. 2.11) and Bernoulli's equation (Eq. 2.12) can be used to calculate test section airspeed (Eq. 2.13).

$$A_{ss}U_{ss} = A_{ts}U_{ts} \quad (2.11)$$

$$\frac{1}{2}\rho U_{ts}^2 + P_{ts} = \frac{1}{2}\rho U_{ss}^2 + P_{ss} \quad (2.12)$$

$$U_{ts} = \sqrt{\frac{2(P_{ss} - P_{ts})}{\rho_{amb} \left(1 - \left(\frac{A_{ts}}{A_{ss}}\right)^2\right)}} \quad (2.13)$$

In Eq. 2.13, the term ρ_{amb} represents the ambient air density and A_{ts}/A_{ss} represents the reciprocal of the contraction area ratio. The ambient air density was calculated using the ideal gas law,

$$\rho_{amb} = \frac{P_{amb}}{RT_{amb}} \quad (2.14)$$

where P_{amb} and T_{amb} represent the ambient air pressure and temperature, respectively, and R represents the specific ideal gas constant for air. P_{amb} was measured by a Setra 270 absolute pressure transducer and T_{amb} was measured by an Omega thermocouple.

2.3.2 Airfoil Model

The multielement S414 airfoil was used in this investigation. The airfoil model had an 18-inch chord and a 34.1-inch span and was composed of both polished aluminum and components fabricated from stereo-lithographically (SLA) fabricated thermosetting plastic. The S414 fore element comprises 80% of the full airfoil chord and the aft element is 33% of the full airfoil chord. The S414 has 13% overhang, 3% gap, and was nested at an aft element deflection angle of $\delta_{aft} = -3^\circ$. The airfoil model fore and aft element were designed and constructed independently. Both the fore and aft element were composed of seven aluminum parts split in the spanwise direction. The aluminum pieces were constructed from a solid block of aluminum using a wire EDM. Of the seven pieces per element, three had an 8-inch span and four had a 2.53-inch span. All aluminum pieces were built to be hollow to save weight and allow easier access to instrumentation, with the 8-inch span pieces having a 0.1875-inch wall thickness and the 2.53-inch span pieces having a 0.375-inch wall thickness. The fore element trailing edge was composed of three SLA parts also split in the spanwise direction. The trailing edge pieces were roughly 1.8 inches long in the chordwise direction, or $0.1 x/c$, and were constructed from SLA to assist in instrumentation installation. The cross section of the S414 wind tunnel model is shown in Fig. 2.6.

The aft element had a 10% full airfoil chord trailing edge plain flap. It was constructed from 3 SLA fabricated parts which were fastened together to create the full-span flap. A removable circular spar was fitted through the flap and secured via external fasteners. The aluminum aft element had a circular cut out centered at the flap hinge location that the flap fit in, called the cove. There were two circular rings inside the aft element cove that the spar passed through to couple the flap to the aft element. The aft element plain flap was able to be deflected from $\delta_f = -20^\circ$ to $\delta_f = 30^\circ$ once fully installed. An exploded view of the full S414 airfoil wind tunnel model can be seen in Fig. 2.7.

In order to configure the aft element plain flap to a given flap setting for testing, alignment jigs were used. Using the known geometry of the turntable and the aft element, deflected flap templates were designed, then laser cut out of acrylic plexiglass. The jig was then used as a stencil to position the flap at the desired δ_f and affixed to each turn table via book tape, allowing the jigs to serve as load bearing structural supports as well. The tested settings were $\delta_f = 0^\circ, 5^\circ, 10^\circ, 15^\circ,$ and 20° . In order to match theoretical simulation conditions and reduce the influence of the aft

element plain flap slot, a seal was placed such that the aluminum portion of the aft element and the plain flap maintained a continuous upper and lower surface for all flap deflections.

The model was fitted with 92 taps distributed along the upper and lower surfaces of both the fore and aft element to acquire time averaged static pressure measurements. Of the 92 taps, 6 were located at $x/c = 0.873$ and distributed across the span to evaluate spanwise flow uniformity. These spanwise taps were distributed such that a higher resolution was provided at the airfoil model tips, where spanwise flow was most likely due to boundary layer separation from the wind tunnel floor and ceiling or other 3D wall interactions. To mitigate the potential influence of bypass transition induced by the tap orifices on downstream measurements, the taps were aligned with a 14° angle with respect to the midspan chord line. The locations and layout of the airfoil model pressure taps are documented in Table 2.1.

The model was installed vertically in the wind tunnel test section such that it spanned the tunnel floor to the tunnel ceiling, making the airfoil model test span 33.6 inches. Two custom floor and ceiling turntables were manufactured that had airfoil shaped cutouts, allowing the ends of the airfoil model to fit inside of a slot within each turntable, such that there was no gap between the model and the wind tunnel floor and ceiling. The fore element had two load bearing steel spars, centered at $0.29 x/c$ and $0.51 x/c$, respectively, while the aft element had one, centered at $0.79 x/c$ (Fig. 2.6). The spars were pinned in place using L-shaped mounting brackets on the outside of the floor and ceiling turntables. The wind tunnel floor turntable was mounted to a 3-component force balance manufactured by Aerotech ATE Limited. No data were acquired by the force balance as it was only used to set the S414 airfoil model angle of attack, which was swept from $\alpha = -15^\circ$ to $\alpha = 20^\circ$ for these tests. A picture of the model installed in the test section can be seen in Fig. 2.8.

In order to reposition the aft element of the S414 airfoil model, multiple turntable inserts were created. The floor and ceiling turntables were designed such that an aluminum insert could be slotted into the turntable location where the aft element was pinned. The insert itself then had an aft element cutout that the aft element could slot into. To reconfigure the aft element location, new inserts were created with the S414 aft element cutout corresponding to the desired location of the aft element with respect to the fore element. The turntable inserts were installed into the floor and ceiling turntable in the same way as the original inserts with the default S414 aft element location. The aft element then was slotted into the new insert, resulting in the aft element being

reconfigured. A picture of the various inserts used to reposition the aft element for this study can be found in Fig. 2.9.

2.3.3 Wake Survey System

A traversable wake rake system, consisting of a wake rake mounted to a two-axis traverse, was used to survey wake pressures. The wake rake, shown installed in the test section in Fig. 2.10, extended 9.75 inches and had 59 total pressure probes, which were constructed out of tubing that had an outer diameter of 0.04 inches. In order to capture total pressure deficits in the wake created by the model, the probes were aligned horizontally and parallel to the freestream flow direction, with 0.135-inch spacing near the middle and 0.27-inch spacing for the last six probes at each end. There were also three static pressure probes mounted above the total pressure probes, however they were not used in this study. Two Zaber linear traverse axes, controlled by stepper motors, were used to traverse the wake rake in the vertical (z -axis) and horizontal (y -axis) directions. Wake pressure data were collected across a plane approximately 1.2 chord lengths downstream of the airfoil model at three vertical locations. To find the wake tail in this plane, an automated LabView routine that compared the gradient of the total pressure deficit across the edges of the wake was used.

2.3.4 Vacuum Suction System

With the intended goal of the current study being the development of a high-lift configuration of the SNLF airfoil, the possibility of spanwise flow due to wall interactions is increased. At high angles of attack, the pressure gradients along the upper surface of the S414 wind tunnel model can be severe enough to cause the boundary layer on the wind tunnel floor and ceiling to separate. Thus, a custom side wall suction system was developed to remove part of the boundary layer that forms on each turntable in order to reduce wall-separation induced spanwise flow and maintain 2D test conditions for the airfoil.

According to Catalano et al²⁶, sidewall suction is most effective when the suction system mass flow reaches roughly 0.4% of the total mass flow through the wind tunnel test section. In their study, increasing the suction system mass flow further resulted little additional decrease in spanwise flow, translating to marginal change in airfoil performance. The mass flow rate for an empty test section with the wind tunnel operating at $Re = 1.8 \times 10^6$ was $\dot{m} = 1.4 \times 10^5 \text{ ft}^3/\text{min}$

(CFM). In order to provide a factor of safety, the mass flow rate of the sidewall suction system was chosen to be 0.45% of the total mass flow rate, or 630 CFM. To account for additional head losses and leakages from the suction supply and plenum system, the target design mass flow rate of the suction system was selected to be $\dot{m}_{ss} = 700$ CFM.

A Dayton 2MXW3 electric motor capable of supplying 25 HP at 3550RPM and a Grainger-Speedaire 2EPR9 positive displacement blower (PDB) capable of up to 953 CFM were chosen to generate the suction used by the system. To control the suction systems, a WolfAutomation LSIS-LSLV0185H100-2Conn Variable Frequency Drive (VFD) was used. The motor and PDB were coupled using 4 type A v-belts. The motor and PDB assembled on a steel pallet and covered by a plywood box to increase user safety. In order to reach the design suction system mass flow of $\dot{m}_{ss} = 700$ CFM, the v-belts were configured to achieve a pulley ratio of 0.867 and 0.832, respectively, such that the PDB operated at 2000 RPM. This required the motor to supply 19.4 HP, which corresponded to a VFD operating frequency of 46.7 Hz at 45 A. The sidewall suction system was tested experimentally to verify these theoretical operational values, as discussed later in Chapter 3.

As mentioned previously, two custom turntables were designed for this study. Porous hole patterns were designed and drilled into each turntable based on Paschal et al.²⁷ The pores follow the contour of the airfoil model upper surface and extend behind the airfoil model to the end of each turntable. In addition, there is a region upstream of the airfoil model in which pores were drilled to follow the curvature of the edge of the turntable. These porous regions were designed to achieve 10% porosity and can be seen in Fig. 2.11. On the top and bottom of the turntables (i.e. directly above and below the test section), plenum boxes that follow the porous patterns were attached. 10 ft-long, 4 in-diameter PVC tubing was used to supply suction generated by the PDB to the plenum boxes, and in turn the test section. The fully assembled and installed sidewall suction system is shown in Fig. 2.12.

2.4 Data Acquisition

A Dell Precision T3400 containing 4 GB of RAM, a 2.83 GHz Intel quad-core processor, and Windows XP 32-bit operating system was used for all data acquisition and wind tunnel control. Several LabView routines containing graphical user interfaces were run on this computer to automate the data acquisition process. These routines allowed the user to specify the desired test

Reynolds number, output data filenames, and calibration procedures. The LabView program required a tap location input file containing information about the airfoil model geometry, an alpha schedule input file containing the angles of attack to be tested, and wake rake input files containing information about which pressure probes to collect data from and the physical wake rake location to survey the wake. The wind tunnel VFD and force balance were controlled using analog signals sent through RS-232 communication. These analog signals were converted using a National Instruments PCI 6052E 16-bit analog to digital converter board. The wake survey system was controlled using digital signals sent through a USB connection. Pressure data signals were transmitted via a TCP/IP ethernet connection.

2.4.1 Pressure Measurements

Time averaged pressure data were acquired from both the airfoil model surface and the wake rake. The pressure measurement system consisted of a Digital Temperature Compensation (DTC) Initium Data Acquisition System connected to five model ESP-32HD miniature electronically-scanned pressure units, manufactured by Esterline, Inc. The ESP-32HD scanners have 32 available pressure ports, as well as a reference pressure port and five calibration ports. Pressure taps/probes were connected to the scanners via urethane pressure tubing. To acquire pressure data, the scanners converted the pressure read by the ports to a proportional voltage using an array of silicon piezo-resistive sensors connected in a Wheatstone bridge configuration. The scanners transmitted the output voltage signals to the DTC/Initium system, which in turn transmitted them to the Dell T3400 master computer.

Three ESP-32HD scanners were used to acquire static pressure data from the taps drilled into the airfoil model surface. To measure pressure at the leading edge of the fore and aft element, a ± 5.0 psid ESP scanner was used due to the expected large pressure differentials across this region. The remaining taps were connected to two ± 1.0 psid ESP scanners. The surface static pressure measurements were zero-referenced against the test section static pressure. Additionally, one of these two scanners had a dedicated pressure tube connected to the settling section pressure probe, allowing for direct measurement of $(P_{ss} - P_{ts})$. Two ESP-32HD ± 0.35 psid (± 10.0 in. WC) were connected to the total pressure probes on the wake rake to acquire wake total pressure data. The wake total pressure measurements were zero-referenced against the ambient air pressure inside the control room to minimize the effects of air circulation from the wind tunnel. All pressure

measurements were sampled at 50 Hz and time-averaged over a two second period. The ESP-32HD scanners were calibrated before every test. Each scanner contained a two position calibration manifold. To switch between run and calibration mode, a controlled pressure pulse was applied.

2.5 Airfoil Performance

As mentioned in section 2.4, all data collected from the airfoil model during testing were acquired from the pressure measurement system, with no data being collected from the force balance. The following section details the data reduction techniques used to calculate the coefficient of lift, drag, and quarter-chord pitching moment.

2.5.1 Airfoil Performance from Surface Pressure Measurements

2.5.1.1 Surface Pressure Coefficient (C_p)

As discussed in section 2.4.1, ($P_{ss} - P_{ts}$) was directly measured by the pressure measurement system, providing greater accuracy than when measured using the Setra 239 pressure transducer detailed in section 2.3.1. Thus, for all freestream data reduction, pressure measurements from the pressure measurement system were used. However, the Setra transducer was used to set the tunnel speed based on the user input test Reynolds number.

Before calculating the pressure distribution about the airfoil surface, which can then be used to calculate the coefficient of lift, pressure drag, and pitching moment, the freestream dynamic pressure (q_∞) must be calculated using Eq. 2.15.

$$q_\infty = \frac{1}{2} \rho_\infty U_\infty^2 \quad (2.15)$$

By employing similar methods used to derive Eq. 2.13, Eq. 2.15 becomes,

$$q_\infty = \frac{1}{2} \rho_\infty U_{ts}^2 = \frac{P_{ss} - P_{ts}}{1 - \left(\frac{A_{ts}}{A_{ss}} \right)^2} \quad (2.16)$$

Note that the low freestream velocity ($M_\infty \leq 0.3$) allows for the assumption of incompressible flow, thus ρ_∞ is taken to be equal to ρ_{amb} . Once the freestream dynamic pressure has been found, the surface pressure coefficient (C_p) can be calculated using Eq. 2.17,

$$C_p = \frac{P_s - P_\infty}{q_\infty} \quad (2.17)$$

where P_s is the local pressure on the airfoil surface measured by the pressure taps, and P_∞ is the freestream static pressure measured at the inlet of the test section, which was assumed to be constant throughout the test section. Because the static pressure measurements from the airfoil taps were referenced to the freestream static pressure such that the quantity measured by the ESP transducers represented $(P_s - P_\infty)$, the surface pressure coefficients were able to be calculated directly by dividing these measurements by the freestream dynamic pressure.

2.5.1.2 Airfoil Lift and Pitching Moment Coefficients

The static pressures measured on the airfoil were used to calculate the airfoil lift and pitching moment coefficients using a panel method. Using this technique, the airfoil contour was approximated by creating nodes at the x and y location of the airfoil surface pressure taps, then linearly interpolating between adjacent nodes to create a panel. Thus, a total of $(n - 1)$ panels are generated for n pressure taps. The pressure across the panel was taken to be the average of the pressures measured by the pressure taps at the bordering nodes and was assumed to act normal to the panel surface. The static pressure vector was then decomposed into the normal force coefficient and the axial force coefficient. These normal and axial force coefficients were computed using Eqs. 2.18 and 2.19,

$$C_{n_i} = \frac{C_{p_i} + C_{p_{i+1}}}{2} (x_{i+1} - x_i) \quad (2.18)$$

$$C_{a_i} = -\frac{C_{p_i} + C_{p_{i+1}}}{2} (y_{i+1} - y_i) \quad (2.19)$$

where C_{n_i} and C_{a_i} represent the chord-normal and chord-axial force coefficients across each panel, respectively, x represents the x -location of the panel, and y represents the y -location of the panel.

The total chord-normal and chord-axial sectional force coefficients were found by summing the chord-normal and chord-axial force coefficients on each individual panel, as seen in Eqs. 2.20 and 2.21,

$$C_n = \sum_{i=1}^{n-1} C_{n_i} \quad (2.20)$$

$$C_a = \sum_{i=1}^{n-1} C_{a_i} \quad (2.21)$$

These normal and axial sectional forces were then used to calculate the coefficient of lift (C_l) of the airfoil using,

$$C_l = C_n \cos(\alpha) - C_a \sin(\alpha) \quad (2.22)$$

where α is the airfoil model angle of attack. The sectional pitching moment about the airfoil leading edge ($C_{m_{LE}}$) was found using,

$$C_{m_{LE}} = \frac{1}{c^2} \left[\sum_{i=1}^{n-1} C_{p_{u,i}} x_{u,i} dx_{u,i} - \sum_{j=1}^{m-1} C_{p_{l,j}} x_{l,j} dx_{l,j} + \sum_{i=1}^{n-1} C_{p_{u,i}} \left(\frac{dy_u}{dx_u} \right)_i y_{u,i} dx_{u,i} - \sum_{j=1}^{m-1} C_{p_{l,j}} \left(\frac{dy_l}{dx_l} \right)_j y_{l,j} dx_{l,j} \right] \quad (2.23)$$

where c is the airfoil model chord, x is the chordwise-location of the center of the airfoil panel, dx change in x across the airfoil panel, dy is the change in y across the airfoil panel, and y is the y -location of the center of the airfoil panel, n is the number of upper surface pressure taps, and m is the number of lower surface pressure taps. The subscripts u and l denote the upper lower surface of the airfoil model, respectively. The pitching moment about the airfoil quarter-chord was then calculated using,

$$C_m = C_{m_{LE}} + x_{c/4} C_l \quad (2.24)$$

where $x_{c/4}$ is the airfoil model quarter-chord.

2.5.1.3 Drag Calculation from Wake Pressures

The drag of the airfoil was determined by integrating across the wake using standard two-dimensional momentum deficit theory, as detailed by Jones²⁸ and Schlichting²⁹. Steady, uniform, 2D incompressible flow was assumed, and a control volume analysis was performed about the body. The in-flow plane was placed arbitrarily upstream of the model such that the plane was still in the test section, and the out-flow plane was placed adequately downstream such that the wake static pressure (P_w) was assumed to be equal to the freestream static pressure (P_∞). This assumption allowed the sectional drag to be calculated using Eq. 2.25,

$$D' = \rho \int u_w (U_\infty - u_w) dy \quad (2.25)$$

Because the flow was assumed to be incompressible ($M_\infty \leq 0.3$), the flow velocities could be expressed using the static and total pressures using,

$$P_\infty + \frac{1}{2} \rho U_\infty^2 = P_{0,\infty} \quad (2.26)$$

$$P_\infty + \frac{1}{2} \rho u_w^2 = P_{0,w} \quad (2.27)$$

U_∞ and u_w can both be solved for in terms of their respective static and total pressures. Substituting those expressions back into Eq. 2.25 resulted in,

$$D' = 2 \int \sqrt{P_{0,w} - P_\infty} \left(\sqrt{P_{0,\infty} - P_\infty} - \sqrt{P_{0,w} - P_\infty} \right) dy \quad (2.28)$$

Combining Eqs. 2.26 and 2.27 allows the dynamic pressure at the wake plane to be expressed in terms of the wake total pressure, freestream total pressure and the freestream dynamic pressure as follows,

$$q_w = q_\infty - (P_{0,\infty} - P_{0,w}) \quad (2.29)$$

Rearranging and substituting Eq. 2.29 into Eq. 2.28 yielded an expression that calculated the sectional drag of the airfoil model from the wake total pressure deficit,

$$D' = 2 \int \sqrt{q_\infty - (P_{0,\infty} - P_{0,w})} \left(\sqrt{q_\infty} - \sqrt{q_\infty - (P_{0,\infty} - P_{0,w})} \right) dy \quad (2.30)$$

Eq. 2.30 proved to be more beneficial as the freestream dynamic pressure is known and the difference between the freestream total pressure and the wake total pressure could be measured directly by the wake rake. However, the ESP scanners used to acquire the total pressure measurements were referenced against the stable atmospheric pressure in the control room to improve repeatability. Thus $(P_{0,w} - P_{atm})$ was measured directly from the airfoil model wake, and $(P_{0,\infty} - P_{atm})$ was measured directly in the region outside the airfoil model wake. To find $(P_{0,\infty} - P_{0,w})$, Eq. 2.31 was used,

$$P_{0,\infty} - P_{0,w} = (P_{0,\infty} - P_{atm}) - (P_{0,w} - P_{atm}) \quad (2.31)$$

With the pressure difference $(P_{0,\infty} - P_{0,w})$ and q_∞ both known, the expression for sectional drag provided by Eq. 2.30 could then be solved by numerically integrating using the trapezoid method. The sectional drag could then be calculated using,

$$D' = \sum_{i=1}^{n_{rake}-1} \left[\frac{\sqrt{q_\infty - (P_{0,\infty} - P_{0,w_i})} \left(\sqrt{q_\infty} - \sqrt{q_\infty - (P_{0,\infty} - P_{0,w_i})} \right) + \sqrt{q_\infty - (P_{0,\infty} - P_{0,w_{i+1}})} \left(\sqrt{q_\infty} - \sqrt{q_\infty - (P_{0,\infty} - P_{0,w_{i+1}})} \right)}{2} \right] (y_i - y_{i+1}) \quad (2.32)$$

where n_{rake} represents the total number of probes that were used to measure the wake. While the vacuum suction system discussed in section 2.3.4 greatly reduced the amount of spanwise flow on the airfoil, there was still a component of spanwise flow due to imperfections on the surface of the model. To provide a spanwise flow invariant estimate of the drag, the wake was surveyed at three spanwise locations, allowing for an average sectional drag to be calculated. The result was an estimate of the drag more characteristic of an infinite span airfoil model. Finally, the drag coefficient of the airfoil model was calculated using,

$$C_d = \frac{D'}{q_\infty c} \quad (2.33)$$

2.6 Airfoil Model Diagnostics

2.6.1 Fluorescent Oil Surface Flow Visualization

In order to visualize the flow over the airfoil model upper surface, fluorescent oil surface flow visualization³⁰ was used. This flow visualization technique provided the means to visually survey the time-averaged surface flow-field characteristics of the airfoil model, such as laminar flow and turbulent flow, transition, spanwise flow, separation, and the formation of a laminar separation bubble (LSB), which was of particular interest in this study as the formation of an LSB along the aft element upper surface has been well documented^{8,12}.

To perform oil surface flow visualization, the following steps were taken. First, the airfoil model upper surface was covered with black contact paper, which served both as a high contrast background for the fluorescent oil and protection for the airfoil model surface pressure taps from the fluorescent oil. Next, strips of orange tape were applied to the model at four streamwise locations. The tape was then marked at regular 10% chord intervals to assist in mapping chordwise locations of flow-field characteristics of interest. A thin layer of 5W-30 motor oil was then applied to the surface of the contact paper, which improved the flow of the fluorescent oil along the upper surface. Next, fluorescent oil was created by mixing mineral oil and an oil-based leak detector dye, which was then evenly applied to the oil-covered contact paper via an airbrush.

Once preparation for oil surface flow visualization was completed, the airfoil model was set to the desired angle of attack and the wind tunnel was run at the desired test condition. After several minutes, the wind tunnel was turned off, and the model was rotated back to $\alpha = 0^\circ$. All lights in the laboratory were shut off, and black lights were used to illuminate the fluorescent dye. Images of the fluoresced dye were acquired using a Nikon D3100 DSLR camera mounted on a tripod. The shutter speed was set to 30 seconds, the ISO to 3200, and the camera was manually focused. To rerun fluorescent oil surface flow visualization, the contact paper on the model upper surface was wiped clean with industrial grade cleaner, and the preparations documented in the previous paragraph were repeated.

2.7 Wind Tunnel Corrections

Due to the inability of the wind tunnel to perfectly recreate an unbounded freestream testing environment as a result of local wall boundary effects, wind tunnel corrections were performed

following Barlow et al.³¹ for 2D, low-Reynolds number wind tunnel testing. These corrections were applied during the calculation of the airfoil performance coefficients and correct for three primary effects: solid blockage, wake blockage, and streamline curvature. Note that these corrections are only valid for steady, incompressible flow.

The first of these effects, solid blockage, results in an increase in local flow velocity near the airfoil model due to an effective reduction in the test-section cross-sectional area. When a wind tunnel model is installed in the test section, the thickness and angle of attack of the model serve to reduce the cross-sectional area of the test section. For continuity to be satisfied, the flow must accelerate. The effects of this increased airspeed near the model were accounted for using the solid-blockage-velocity increment, ε_{sb} ,

$$\varepsilon_{sb} = \frac{K_I V_m}{C^{3/2}} \quad (2.34)$$

where K_I is a constant parameter based on the airfoil configuration, C is the empty test-section area, and V_m is the volume of the airfoil model. For this study, $K_I = 0.52$, as defined by Barlow et al.³¹ for airfoil models that span the height of the test-section. V_m was estimated using,

$$V_m = \frac{3}{4} tcb \quad (2.35)$$

where t , c , and b are the dimensional thickness, chord, and span of the airfoil model, respectively.

Another cause of the increase in the local airspeed about the airfoil model is the wake blockage effect. As mentioned in section 2.5.1.3, the wake of the airfoil is characterized by a region of decreased velocity. For the mass flow rate to remain constant, the velocity of the air in the potential flow region outside the wake of the airfoil must increase. Because the wake velocity deficit is directly related to the profile drag of the airfoil model, the local flow velocity outside the wake scales proportionally with the airfoil model drag. As such, the resulting increase in local flow velocity due to the wake blockage effect, ε_{wb} , can be estimated using,

$$\varepsilon_{wb} = \frac{1}{2} \frac{c}{h} C_{d,u} \quad (2.36)$$

where h is the height of the wind tunnel test section and $C_{d,u}$ is the uncorrected airfoil drag coefficient calculated using Eq. 2.33. To find the total local velocity increment near the airfoil model as a result of these blockage effects, the respective estimated velocity increments were simply summed together,

$$\varepsilon = \varepsilon_{sb} + \varepsilon_{wb} \quad (2.37)$$

In addition to blockage effects, the bounded nature of the flow through the test section causes streamwise curvature effects. The result of these streamwise curvature effects is an increase in the apparent camber of the airfoil model, which leads to greater lift and quarter-chord pitching moment generation than if the model were tested in a true unbounded flow-field. An empirically derived constant, σ , can be used to correct for these effects. The constant σ was calculated using,

$$\sigma = \frac{\pi^2}{48} \left(\frac{c}{h} \right)^2 \quad (2.38)$$

With the correction factors calculated using Eqs. 2.34, 2.36, 2.37, and 2.38, the airfoil model angle of attack and performance coefficients were able to be corrected using a set of empirically-derived equations. The airfoil model angle of attack, lift coefficient, drag coefficient, and quarter-chord pitching moment coefficient were corrected using,

$$\alpha_{cor} = \alpha_u + \frac{57.3\sigma}{2\pi} (C_{l,u} + 4C_{m,u}) \quad (2.39)$$

$$C_{l,cor} = C_{l,u} (1 - \sigma - 2\varepsilon) \quad (2.40)$$

$$C_{d,cor} = C_{d,u} (1 - 3\varepsilon_{sb} - 2\varepsilon_{wb}) \quad (2.41)$$

$$C_{m,cor} = C_{m,u} (1 - 2\varepsilon) + \frac{1}{4} \sigma C_{l,u} \quad (2.42)$$

$$C_{p,cor} = \frac{C_{p,u}}{(1 + \varepsilon)^2} \quad (2.43)$$

2.8 Chapter 2 Tables and Figures

Table 2.1 Surface pressure tap locations on the S414 airfoil model.

Fore Element			
Upper Surface		Lower Surface	
x/c	z/b	x/c	z/b
0	0.607	0	0.607
0.002	0.606	0.001	0.393
0.005	0.606	0.006	0.394
0.011	0.605	0.011	0.395
0.018	0.604	0.021	0.396
0.028	0.603	0.031	0.397
0.038	0.602	0.041	0.399
0.048	0.6	0.066	0.402
0.073	0.597	0.091	0.405
0.098	0.594	0.116	0.409
0.123	0.59	0.166	0.416
0.148	0.587	0.241	0.426
0.186	0.582	0.316	0.436
0.242	0.574	0.391	0.446
0.298	0.567	0.466	0.456
0.348	0.56	0.528	0.464
0.414	0.551	0.558	0.468
0.483	0.542	0.591	0.472
0.546	0.534	0.616	0.476
0.583	0.529	0.626	0.477
0.612	0.525	0.636	0.478
0.634	0.522	0.646	0.48
0.653	0.519	0.656	0.481
0.669	0.517	0.666	0.482
0.683	0.515	0.676	0.484
0.693	0.514	0.686	0.485
0.713	0.579	0.696	0.486
0.723	0.58	0.706	0.602
0.733	0.58	0.716	0.599
0.799	0.586	0.726	0.596
		0.736	0.594
		0.799	0.586

Aft Element			
Upper Surface		Lower Surface	
x/c	z/b	x/c	z/b
0.667	0.455	0.667	0.455
0.669	0.544	0.673	0.456
0.672	0.544	0.68	0.457
0.676	0.543	0.69	0.459
0.683	0.542	0.71	0.461
0.693	0.541	0.73	0.464
0.718	0.538	0.755	0.467
0.743	0.534	0.79	0.472
0.773	0.53	0.83	0.477
0.803	0.526	0.87	0.483
0.838	0.522	0.921	0.489
0.873	0.517	0.956	0.494
0.927	0.509	1	0.5
0.962	0.505		
1	0.5		

Spanwise	
x/c	z/b
0.873	0.963
0.873	0.877
0.873	0.746
0.873	0.517
0.873	0.254
0.873	0.123
0.873	0.037

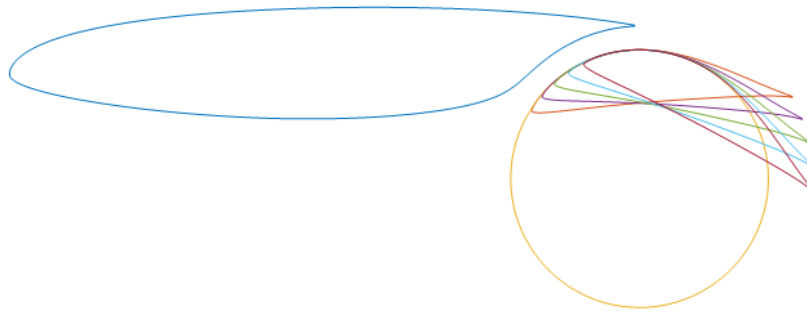


Fig. 2.1 Sample aft element positions for the slot-based repositioning approach.

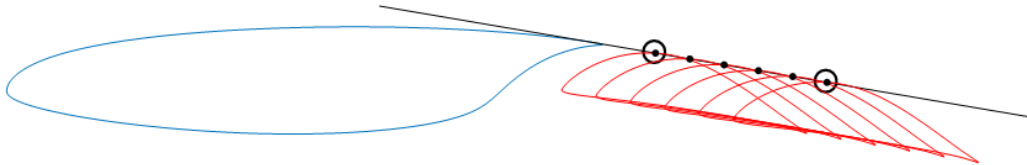


Fig. 2.2 Sample aft element positions for the dumping velocity-based repositioning approach.

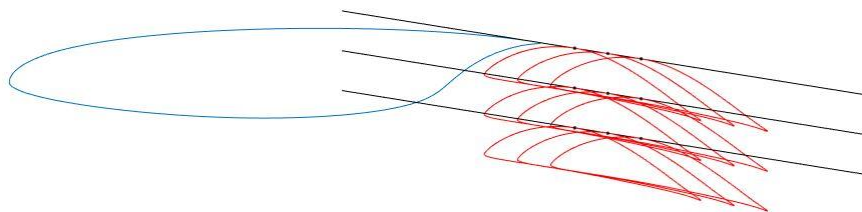


Fig. 2.3 Sample aft element positions for the expanded dumping velocity-based repositioning approach.

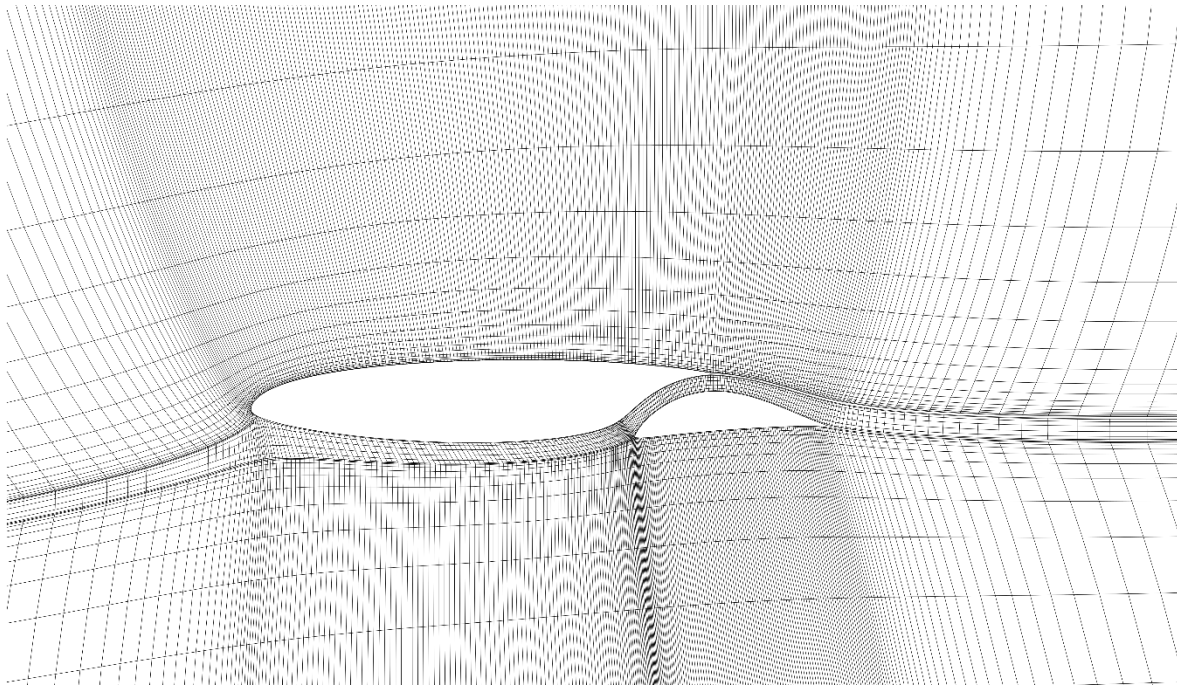


Fig. 2.4 Sample MSES grid for the S414 generated using MSET.

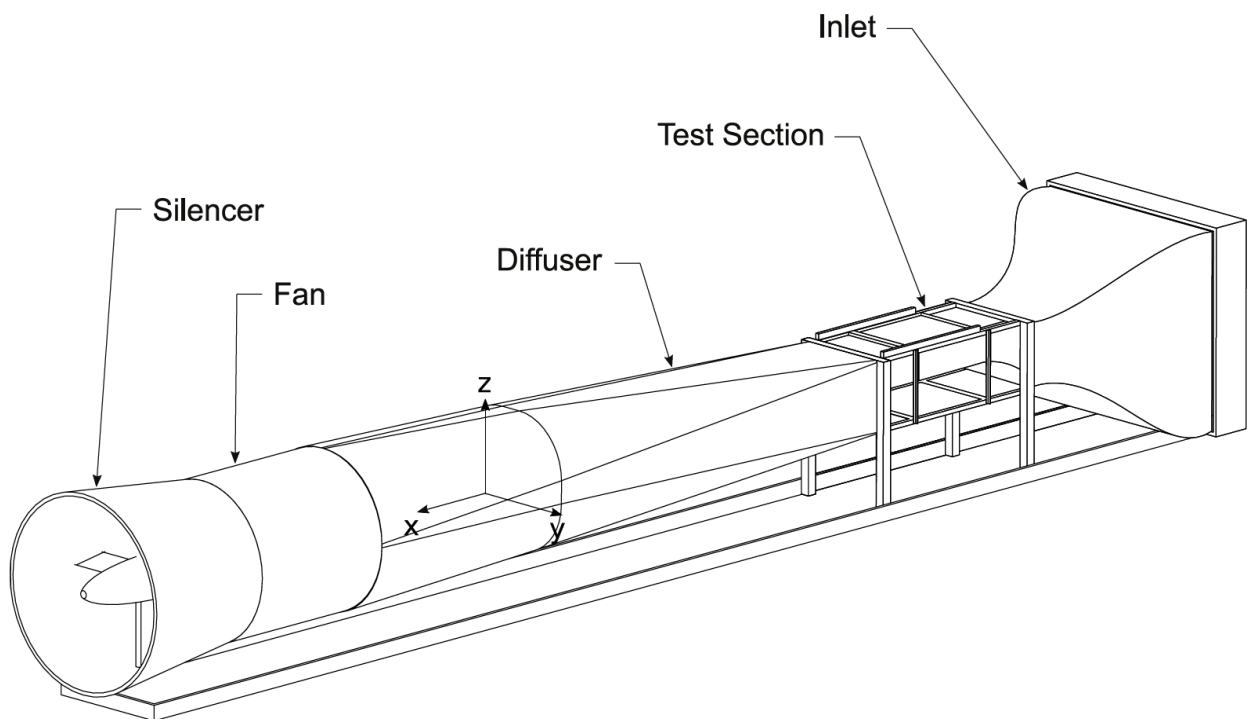


Fig. 2.5 Schematic of the University of Illinois 2.8-ft \times 4-ft subsonic wind tunnel.

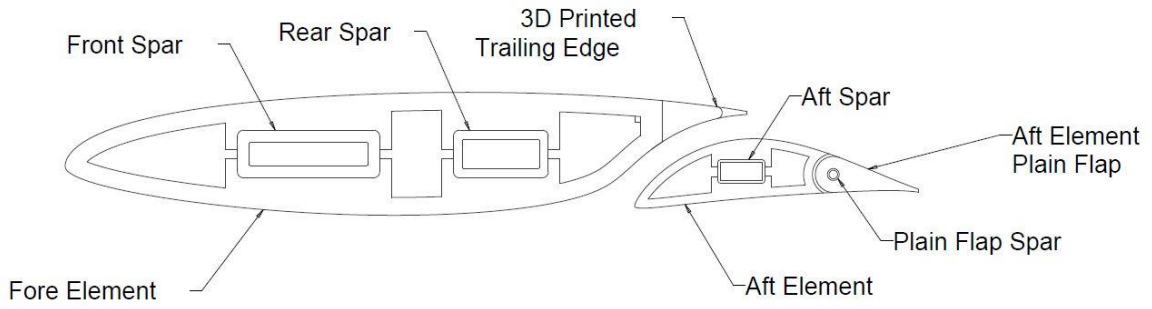


Fig. 2.6 S414 geometry demonstrating spar locations, the aft element plain flap, and the 3D printed fore element trailing-edge.

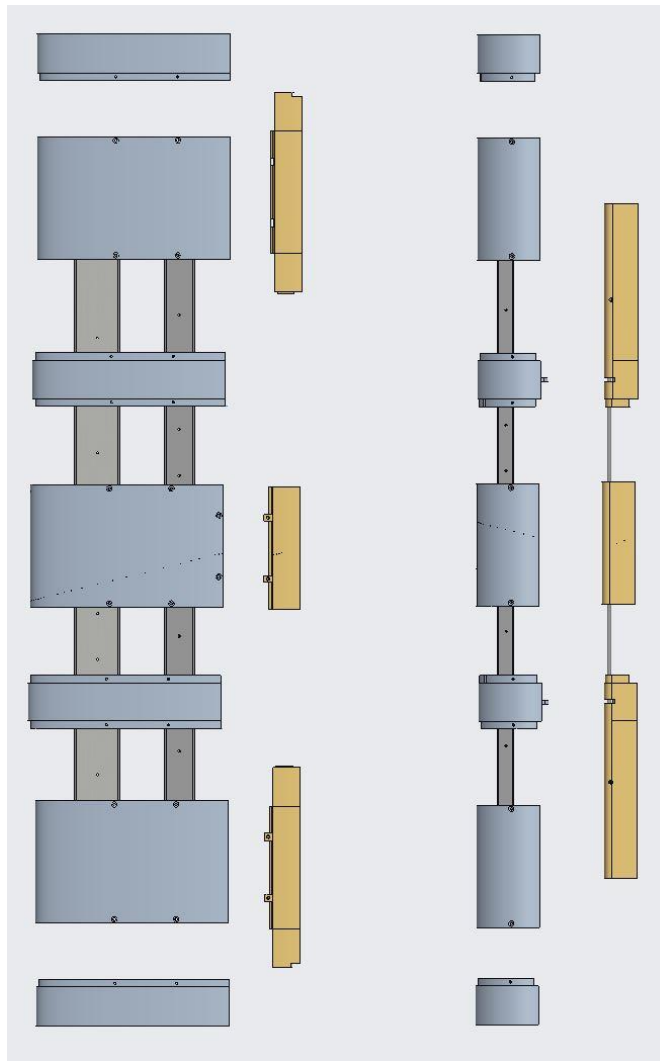


Fig. 2.7 Exploded view of the S414 airfoil model. Aluminum parts are depicted in light gray, steel spars in dark gray, and the 3D printed parts in gold.



Fig. 2.8 The S414 airfoil model installed in the wind tunnel test section.



Fig. 2.9 Inserts used to set the alternate aft-element locations. From top left: Case 1, Case 2, Case 3, Case 4, Case 5.



Fig. 2.10 Wake rake installed in the test section downstream of the S414 airfoil model.

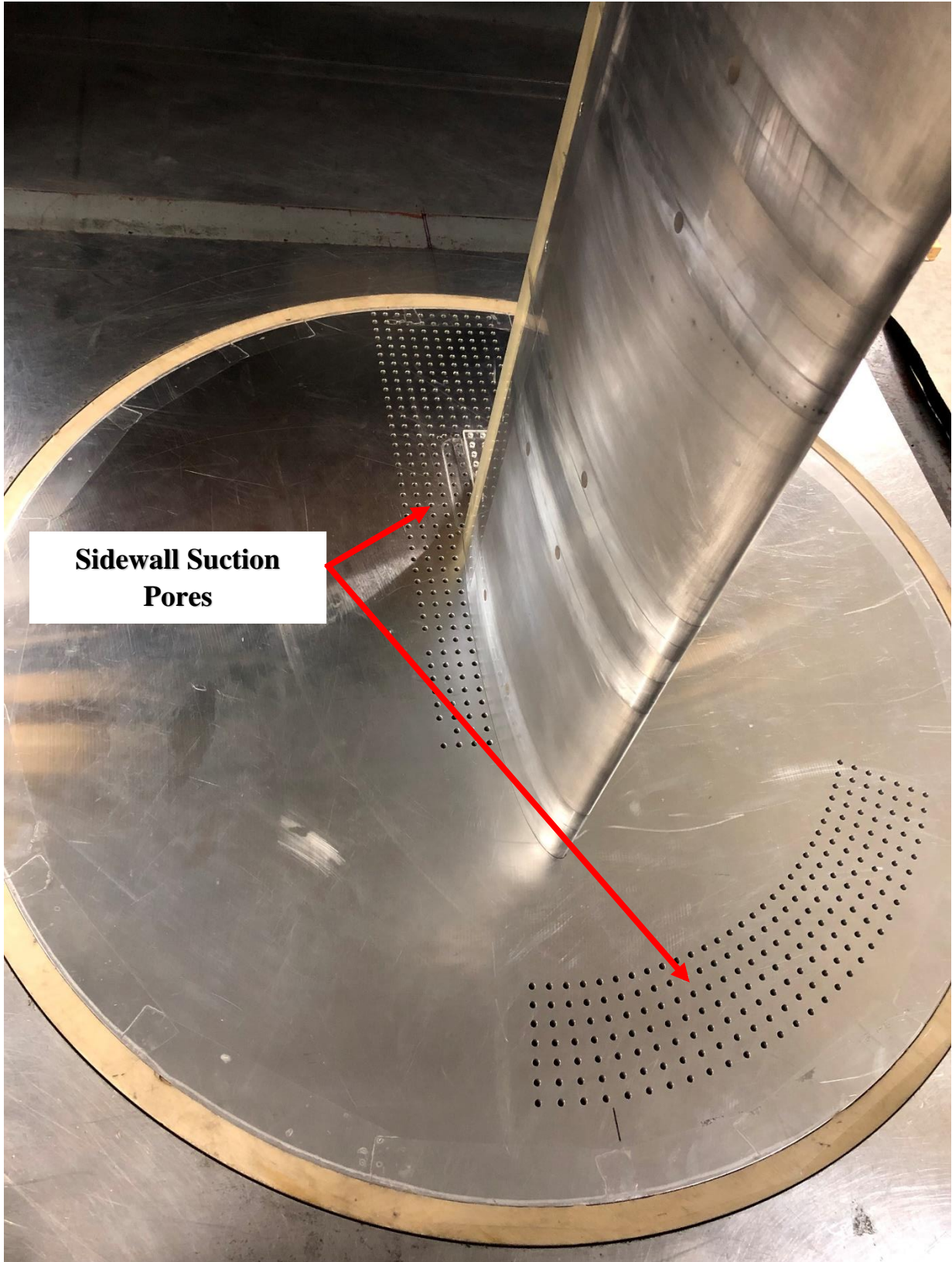


Fig. 2.11 Custom turntable with holes configured to provide sidewall suction.

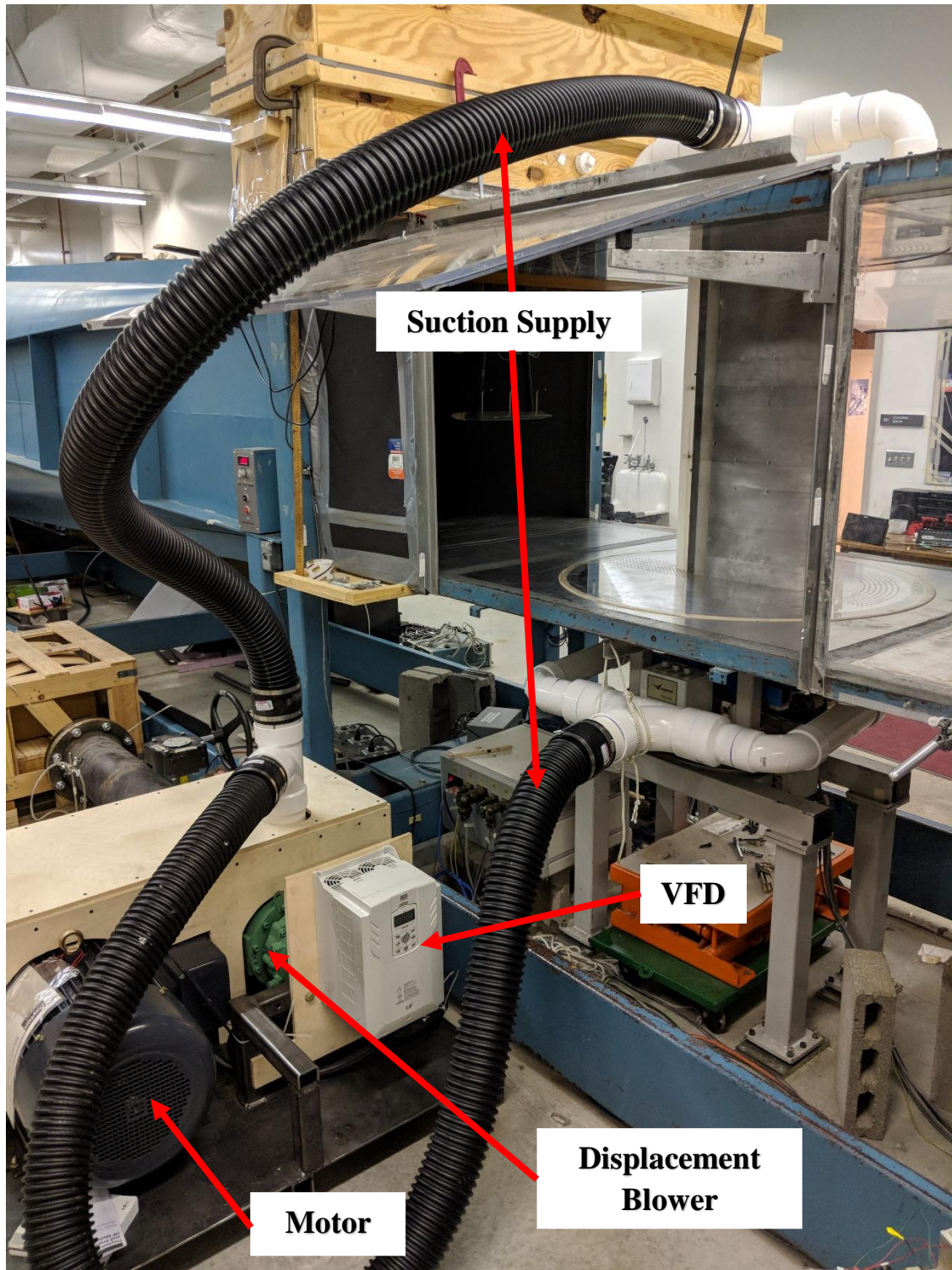


Fig. 2.12 Vacuum suction system with ducting attached to the plenum boxes on the top and bottom of the test section.

Chapter 3

Results and Discussion

This chapter details the results from the experimental and theoretical investigation performed during this study. The findings from the parametrically-surveyed theoretical design space are discussed, as well as the performance parameters used to select the alternative aft-element positions to test experimentally. The results from experimentally-tested alternative aft-element positions are also presented.

3.1 Theoretical Results

3.1.1 S414 Theoretical Characterization

In order to provide greater insights into the effects of the alternative aft-element riggings, MSES was used to generate baseline performance predictions with the aft element in its nested configuration and the plain flap undeflected. The resulting polars are shown in Fig. 3.1. At $Re = 1.5 \times 10^6$, $M = 0.17$, the flow conditions used for all aft element positioning routines, the theoretical maximum lift coefficient was found to be $C_{l,max} = 1.82$ at $\alpha_{stall} = 13^\circ$. The theoretical analysis was performed at these conditions due to the ease of convergence of MSES and their proximity to predicted experimental conditions. These polar values were used as a baseline of comparison when evaluating the theoretical performance of the various high-lift rigging configurations.

3.1.2 Slot-Based Approach

The slot-based approach was programmed by iteratively rotating the aft element from its nested configuration of $\delta_{aft} = -3^\circ$ to $\delta_{aft} = 17^\circ$ in 1° increments and computing a C_l vs α polar at each flap position at each increment. The results for $Re = 1.5 \times 10^6$, $M = 0.17$ can be seen in Fig. 3.2. It was found that $C_{l,max}$ increased with increasing aft-element deflection up until $\delta_{aft} = 10^\circ$. In this position a maximum lift coefficient of $C_{l,max} = 1.95$ was achieved, marking a 7% increase from the baseline configuration. It can also be seen that there were several δ_{aft} cases which have higher C_l values at $\alpha = 0^\circ$ that did not fully converge. The difficulty with obtaining converged solutions for these cases was attributed to the emergence of confluent boundary layers. As the aft element was rotated to a higher deflection angle, the flow off the trailing edge of the fore element was observed to begin impinging upon the aft element. This confluence in the boundary layers makes it increasingly difficult to resolve the flow interactions produced in this region using MSES and is even known to be problematic to fully resolve with many Navier-Stokes solvers.

The slot-based approach routine was also run with the aft element flap deflection angle set to $\delta_f = 5^\circ$ and $\delta_f = 10^\circ$. The results can be seen in Fig. 3.3. As expected, when the flap is deflected on the aft element, the C_l curves shift in the positive C_l and negative α direction, resulting in a higher $C_{l,max}$ but lower α_{stall} . When $\delta_f = 5^\circ$, the highest predicted maximum lift coefficient produced was $C_{l,max} = 2.0$ at $\alpha_{stall} = 11.5^\circ$ and $\delta_{aft} = 13^\circ$. When $\delta_f = 10^\circ$, the highest predicted maximum lift coefficient produced was $C_{l,max} = 2.1$ at $\alpha = 11.5^\circ$ and $\delta_{aft} = 15^\circ$. These points correspond to increases in $C_{l,max}$ of 4.6% and 7.7%, respectively, when compared to the highest $C_{l,max}$ achieved in the baseline ($\delta_f = 0^\circ$) slot-based approach configurations and increases of 12% and 15.4% with respect to the unmodified S414 airfoil. These increases can be attributed to the increased circulation provided by the deflected flap.

3.1.3 Dumping Velocity-Based Approach

A dumping velocity-based approach was programmed and executed with the aft element tangency point enforced at $x_{aft}/c_{aft} = 3/8$. The sensitivity of variation in the aft element position was then analyzed by translating and rotating the aft element such that the tangency point was swept between $x/c = 0.83$ to $x/c = 0.9$ of the full airfoil chord at increments of $\Delta x/c = 0.1$. The results for $Re = 1.5 \times 10^6$, $M = 0.17$ can be seen in Fig. 3.4. The maximum lift coefficient was observed to increase with increasing flow tangency streamwise location until a maximum of $C_{l,max} = 2.25$ was

achieved when the aft-element flow tangency point was located at $x/c = 0.9$ at $\alpha_{stall} = 11^\circ$. This condition corresponds to a 24% increase in $C_{l,max}$ relative to the baseline configuration. Orienting the aft element such that there is a point upon which the high-speed flow discharged off the fore element trailing edge is tangent to the aft element upper surface greatly increases the effectiveness of the aft element by taking advantage of the broader low-pressure region produced across the aft element leading edge. Additionally, the fore element dumping velocity increases, which reduces the pressure recovery requirements of the fore element and increases the local C_l of the aft element, which in turn drives an increase in the total C_l of the multielement airfoil assembly. The downside of moving the aft element away from the cove, however, is that in its nested configuration the aft element acts to keep the flow attached in the cove region of the fore element. With the aft element now downstream, the flow separates across the cove region of the forward element lower surface, slightly reducing the fore element C_l .

The dumping velocity-based approach routine was also run with the aft element flap deflection angle set to $\delta_f = 5^\circ$ and $\delta_f = 10^\circ$. Lift predictions can be seen in Fig. 3.5. Interestingly enough, there was not significant variation in either $C_{l,max}$ or α_{stall} across the different δ_f values. When $\delta_f = 5^\circ$, a maximum lift coefficient of $C_{l,max} = 2.19$ occurred at $\alpha_{stall} = 11.5^\circ$, and when $\delta_f = 10^\circ$, a maximum lift coefficient of $C_{l,max} = 2.21$ occurred at $\alpha_{stall} = 10.5^\circ$. These slight decreases in $C_{l,max}$ are a result of the flow separating at the flap hinge. Given that the aft element is already at an aggressive δ_{aft} , causing large adverse pressure gradients, deflecting the flap results in early separation across the aft element before the added circulation benefits can be fully exploited.

Some convergence challenges can clearly be seen in the MSES predictions for the smaller streamwise flow tangency point locations, which is believed to be produced by the confluent boundary layer problem discussed previously. Additionally, it is observed that MSES had greater difficulty capturing the nonlinear portion of the polar, which is a common difficulty with many flow simulation approaches. The pressure distribution across the sharp leading edge of the aft element also becomes increasingly difficult to resolve at higher angles of attack, further exacerbating convergence challenges.

3.1.4 Expanded Dumping Velocity-Based Approach

An expanded dumping velocity-based aft element repositioning routine was also executed as a parametric optimization scheme. The initial flow-line offset distance was $\Delta x/c = 0.0125$, with

five positions captured with enforced tangency points between $x/c = 0.85$ to $x/c = 0.95$. The multielement airfoil angle of attack was set to $\alpha = 3^\circ$ for all cases. Once a parametric sweep at a fixed aft-element deflection was completed, a contour map of C_l was created for varying aft-element position. The positioning boundary of the aft element was then reduced to a range between $x/c = 0.85$ to $x/c = 0.90$, and ten positions were captured to provide greater resolution of C_l vs aft element location, as demonstrated in Fig. 3.6. This approach allowed the rigging configuration that produced maximum lift to be better resolved. Additionally, aft-element effectiveness plots were created for varying aft-element deflection angle by plotting ΔC_l vs δ_{aft} . As seen in Fig. 3.7, ΔC_l increases with increasing δ_{aft} until a local maximum occurs. The curve then begins to decrease until an abrupt drop in ΔC_l occurs. This decrease is a result of the aft element beginning to separate and losing lift production as δ_{aft} increases. C_l isocontours and flap effectiveness curves were generated for every δ_{aft} and aft element location respectively. Flap deflections were not analyzed in this routine due to convergence challenges within MSES, as well as the fact that the flap deflections would have little impact on the desirable aft element positioning schemes attained from this routine.

3.2 Selection of Aft Element Positions for Experimental Testing

After completing a theoretical analysis on the S414 aft element, 4 alternate riggings were selected for experimental evaluation. The first was generated from the slot-based approach. From this approach, the configuration in which $\delta_{aft} = 11^\circ$ was consistently able to produce the largest maximum lift coefficient across the range of analysis performed, including alternate run conditions and various δ_f values. While the $C_{l,\alpha=0^\circ}$ was the highest when $\delta_{aft} = 15^\circ$, the convergence issues present at higher α and marginal increase in lift compared to the $\delta_{aft} = 11^\circ$ case resulted in the selection of the configuration in which $\delta_{aft} = 11^\circ$ as the alternate slot-based rigging. From the dumping velocity-based approach, an aft-element tangency point of $x_{aft}/c_{aft} = 3/8$ located at a streamwise position of $x/c = 0.87$ was chosen. This arrangement was observed to produce the maximum lift for this positioning scheme and was also selected due to geometric constraints. The significant decrease of the slot width with tangency points at values less than $x/c = 0.85$ was also factored into the decision, as maintaining the benefits of the slot was preferred. There were two alternate riggings also selected from the expanded dumping velocity-based approach. The first was identified based on consideration of aft-element effectiveness, C_l , and geometric constraints. While

there were several promising candidate positions, a slightly offset aft element in which $\delta_{aft} = 8^\circ$ showed the most promise in both the C_l contours and aft element effectiveness plot. With an enforced tangency point at $x/c = 0.87$, this configuration showed large amounts of lift production across wide δ_{aft} ranges. Its effectiveness plot also indicated that when $\delta_{aft} = 8^\circ$, the aft-element effectiveness reached a maximum ΔC_l . The second expanded dumping-velocity rigging was also chosen to have a tangency point of $x/c = 0.87$, but with $\delta_{aft} = 18^\circ$. This rigging was selected to be intentionally aggressive to allow more insightful active flow control (AFC) testing in the future. All rigging positions can be seen in Fig. 3.8. Additionally, a summary of the gap, overhang, and aft element deflections produced by these four cases are provided in Table 3.1.

3.3 Sidewall Suction System

Theoretical calculations indicated that running the sidewall suction system with a VFD frequency of 45 Hz would be sufficient to provide the necessary suction for flow uniformity across the model span. In order to experimentally validate the sidewall suction system, tests were performed at $Re = 1.8 \times 10^6$ with angle of attack varied from $\alpha = 5^\circ$ to $\alpha = 20^\circ$ at 1° increments, and the VFD operating frequency was swept from 30 Hz to 50 Hz at 5 Hz after each run. The resulting spanwise pressure distributions at $\alpha = 5^\circ$ and $\alpha = 15^\circ$ can be seen in Fig. 3.9. At $\alpha = 5^\circ$, the flow uniformity increases with increasing suction power. As the sidewall suction system removes the boundary layer off the floor and ceiling, the spanwise C_p distribution flattens to be almost linear across the span, aside from the regions of high pressure at the tips of the airfoil model most likely caused by sidewall interactions. The region of near constant C_p across the span indicates that the suction system is successfully removing the wind tunnel floor and ceiling boundary layers, resulting in very little spanwise flow, similar to an infinite wing. At $\alpha = 15^\circ$, right before stall, the C_p is lowest near the tips and pressure increases near the center of the airfoil model ($y/b = 0.5$). In this case, the sidewall suction system is most likely delaying stall near the tips of the airfoil model, resulting in regions of lower pressure. However, near the center of the airfoil model, the flow begins to separate, causing the pressure to increase. The spanwise pressure distributions also demonstrate that around 45 Hz, a high enough mass flow percentage has been achieved such that there is little additional boundary-layer suction benefit seen when the VFD is run at a higher frequency, similar to Catalano et al.²⁶ As such, the sidewall suction system was operated at a VFD frequency of 45 Hz for all testing.

This setting was tested by running an α polar at $Re = 1.0 \times 10^6$, $M = 0.10$ with suction and without. The results can be seen in Fig. 3.10 and Fig 3.11. The lift-curve slope increased slightly with suction to $C_{l,\alpha} = 0.110 /^\circ$ from the no suction case where $C_{l,\alpha} = 0.108 /^\circ$. The maximum lift coefficient also increased to $C_{l,max} = 1.919$ ($\alpha_{stall} = 16^\circ$) from the no suction case where $C_{l,max} = 1.843$ ($\alpha_{stall} = 15^\circ$). In addition, the spanwise pressures are distributed across a smaller C_p band, indicating reduced spanwise flow when compared to the no suction case.

3.4 Experimental Validation of the S414 Airfoil Model

Before the alternative riggings were tested experimentally, the S414 airfoil model was validated against prior work. However, there were no data in the literature for the S414 at $Re = 1.8 \times 10^6$. As such, the S414 airfoil model was validated at $Re = 1.0 \times 10^6$, $M = 0.10$, where there was more data readily available. The results from this test were compared to experimental data from Somers and Maughmer⁸, as well as theoretical predictions from MSES¹⁴. To more closely match test conditions from the literature, the suction system was run at 45 Hz.

The airfoil polar results can be seen in Fig. 3.12. The model shows good agreement with the previously-corroborated test data and MSES predictions. The lift curves are virtually identical to up to roughly $\alpha = 12^\circ$, where the current model maintains a slightly higher $C_{l,\alpha}$ until stall. $C_{l,max}$ for both occurs at $\alpha = 16^\circ$, but the current model achieves a maximum lift coefficient of $C_{l,max} = 1.917$ whereas the Penn State model achieves $C_{l,max} = 1.855$. This difference is most likely due to the suction system preventing aggressive pressure gradients from causing separation of the wall boundary layer and introducing 3D flow effects, which results in a reduced lift curve slope and a lower $C_{l,max}$. There is relatively good agreement between the drag data as well. Both low drag buckets begin at approximately $\alpha = -3^\circ$, and end at around $\alpha = 2^\circ$. However, the Penn State model achieves a minimum profile drag of $C_{d,min} = 0.0059$ at $\alpha = -3^\circ$, as opposed to $C_{d,min} = 0.0077$ at $\alpha = 0.5^\circ$ for the model used in the current study. The variations in the low drag bucket are attributed to physical differences in the model and freestream turbulence intensity. Given that the airfoil in the current study was configured for high-lift testing, the model was developed to sustain exceedingly high loads. As a result, the S414 airfoil model used in the current study was constructed using a series of joined spanwise segments attached to a steel frame to carry these loads and prevent aeroelastic deformation. In contrast, the airfoil model used by Somers & Maughmer⁸ was constructed from solid aluminum using a CNC mill, and features an overall

improved surface quality as compared to that used in the current study. Additionally, the S414 airfoil model used in the current study was built with various 3D printed components and a simple flap integrated into the aft element. While steps were taken to reduce the increased drag produced by the seams built into the model used in the current study, a slight increase in drag was expected across the low-drag bucket region due to the additional excrescences. In addition, the Penn State wind tunnel is capable of much lower turbulence intensities, which explains the shift in α for minimum profile drag, as well as the lack of formation of a “horn”¹² in the beginning of the low drag bucket in their data. It should, however, be emphasized that the purpose of the current study is to evaluate the maximum lift capabilities of the S414 airfoil in various alternate aft element positions and simple flap deflections. As a result, the discrepancy in the absolute drag values across the laminar bucket do not detract from the conclusions of the present research.

Fig. 3.13 shows a comparison of the C_p distributions at $\alpha = 0^\circ$, $\alpha = 5^\circ$, $\alpha = 10^\circ$, and $\alpha = 15^\circ$. The S414 airfoil model used in the current study once again shows good agreement with previous data and MSES predictions for all angles of attack. At $\alpha = 5^\circ$, $C_{p,min} = -1.68$, which is identical to that measured by Somers and Maughmer. However, downstream of the leading edge suction peak, the current study predicts slightly lower C_p values, starting around $x/c = 0.1$. This continues to the fore element trailing edge, where $C_p = -0.529$, as opposed to $C_p = -0.335$ as reported by Somers & Maughmer. This phenomenon is most likely caused by the influence of the physical junction between the 3D printed fore element trailing edge and the aluminum fore element pieces. The flow accelerates over this seam, resulting in the favorable pressure gradient beginning at $x/c = 0.67$. This change in trailing edge flow behavior produces a consistent artificial decrease in C_p across both the fore and aft element of the airfoil model used in the current study. This effect can be seen at all angles of attack. Both MSES and Somers & Maughmer indicate the presence of a laminar separation bubble (LSB) on the aft elements upper surface beginning at approximately $x/c = 0.84$. The model used in the current study did not have sufficient surface pressure tap density to capture an LSB in this location. As such, flow visualization was used to investigate the presence of an LSB instead.

Fluorescent oil surface flow visualization³² was performed on the S414 airfoil model in its baseline configuration. Experiments were performed at $Re = 1.0 \times 10^6$, $M = 0.10$, and $\alpha = 3^\circ$ in order to directly compare to a study done by Maughmer et al.¹³, which demonstrated the formation of an LSB on the aft element using both fluorescent oil surface flow visualization and a sufficiently

fine surface pressure tap distribution. Fig. 3.14 contains an image of the surface oil flow visualization compared to the corresponding C_p distribution at these flow conditions. Several flow features can be identified from this visualization by careful inspection of the fluorescent oil flow patterns. Before roughly $x/c = 0.55$, the oil droplets appear speckled, indicating lower shear-stress on the airfoil surface produced by the flow, which is characteristic of a laminar boundary layer. However, after approximately $x/c = 0.60$, the droplets are more streaked, indicating higher shear-stress on the airfoil surface produced by the flow, which is associated with the increased mixing present in a turbulent boundary layer. These two distinct regions of the flowfield imply that the flow transitions between $x/c = 0.51$ and $x/c = 0.60$. A buildup of oil can be seen at $x/c = 0.70$, which is the location of the juncture between the 3D printed trailing edge and the aluminum fore element pieces. Steps were taken to reduce the surface imperfections caused by this juncture, however there is still accumulation of oil at this location, signifying the presence of a physical seam. The trailing edge of the fore element causes an additional spanwise accumulation of oil, seen at $x/c = 0.80$. An LSB can also be seen from roughly $x/c = 0.83$ to $x/c = 0.89$. At $x/c = 0.83$, the oil appears to accumulate, and is immediately followed by a region of seemingly unmoved oil droplets. At $x/c = 0.89$, the oil droplets become heavily streaked, similar to the flowfield downstream of the assumed flow transition point on the fore element. These features indicate that the flow separates at $x/c = 0.83$, resulting in a slight accumulation of oil and stagnant, unmoved droplets until $x/c = 0.89$, where the now turbulent boundary layer reattaches. Downstream of this reattachment point, the oil droplets remain heavily streaked until the trailing edge of the aft element.

While the S414 fore element is designed to maintain laminar flow across its entire upper surface⁸, the S414 airfoil model used in the current study appears to have premature transition. This is most likely caused by the physical attributes of the model discussed above. Despite this fact, an LSB forms across of the aft element upper surface in the same location as demonstrated by previous work^{8,12,13}, demonstrating good agreement with historical data for this airfoil.

3.5 Alternative Aft Element Rigging Experiments

The following section details the results of the experimental tests of the S414 airfoil model, including the theoretically-determined alternative aft-element positions. All tests were performed at $Re = 1.8 \times 10^6$ and $M = 0.18$.

3.5.1 Baseline Case

The S414 was first tested in its original design configuration. The S414 was designed to exhibit a high maximum lift coefficient and low profile drag⁸. The low-drag constraint was satisfied by shaping the airfoil geometry such that an extensive favorable pressure gradient forms on the fore element upper and lower surface, allowing for significant regions of laminar flow. A typical disadvantage of utilizing laminar flow to reduce drag is the severe adverse pressure gradients that form near the trailing edge of the airfoil, which are needed to provide the necessary pressure recovery. In addition, this rapid pressure recovery near the trailing edge generally results in decreased maximum lift due to the early onset of trailing-edge separation. To solve both these problems simultaneously, the S414 uses multi-element airfoil approach with a slot between the two elements. The S414 aft element handles the majority of the pressure recovery burden, allowing the fore element to maintain laminar flow across the entirety of the upper surface. Because the flow discharged off the trailing edge of the fore element does not directly impinge upon the aft element upper surface, the aft element is also capable of maintaining a significant portion of laminar flow. The two element nature of the design also incorporates a constant-width slot between the fore element and the aft element, which serves as a form of passive flow control. By providing an injection of high momentum air to the upper surface of the aft element, the slot allows the aft element to maintain attached flow at high angles of attack. Thus, both low profile drag and high maximum lift can be achieved.

Airfoil performance plots can be seen in Fig. 3.15. Using the techniques discussed previously, both high maximum lift and low profile drag were achieved. A high maximum lift coefficient of $C_{l,max} = 2.00$ was achieved at $\alpha_{stall} = 16.4^\circ$. The airfoil has a zero-lift angle of attack of $\alpha_{zL} = -3.3^\circ$ and an $\alpha = 0^\circ$ lift coefficient of $C_{l,\alpha=0^\circ} = 0.38$. Additionally, the S414 airfoil model exhibits abrupt stall behavior as predicted by MSES. Because the aft element is used to ameliorate the rapid pressure recovery at the trailing edge typically associated with NLF airfoils, the S414 becomes leading edge stall limited. At about $\alpha = 10^\circ$, the boundary layer begins to thicken, resulting in a viscous decambering of the airfoil, and a gradual decrease in $C_{l,\alpha}$ until stall. The S414 also achieves its goal of low profile drag, with a laminar drag bucket that has a minimum drag coefficient of $C_{d,min} = 0.00803$ at $C_l = 0.38$. The laminar drag bucket begins at $C_l = 0.091$ ($\alpha = -2.65^\circ$) and continues until $C_l = 0.496$ ($\alpha = 0.96^\circ$). Fig. 3.16 shows the result of deflecting the plain flap. As δ_f increases, the lift curve shifts in the positive C_l and negative α direction. The

largest maximum lift coefficient produced by deflecting the plain flap was $C_{l,max} = 2.29$ at $\alpha_{stall} = 15.4^\circ$ and $\delta_f = 20^\circ$, marking an increase in the maximum lift coefficient of ΔC_l of 0.29 over the $\delta_f = 0^\circ$ baseline case.

Fig. 3.17 shows the C_p distribution of the S414 airfoil model for $\alpha = 0^\circ, 5^\circ, 10^\circ, 15^\circ,$ and 20° . As the angle of attack increases, a large suction peak forms at the leading edge, with a minimum pressure coefficient of $C_{p,min} = -10.2$ just before stall. The adverse pressure gradient becomes severe enough that the flow separates off the leading edge, explaining the abrupt stall behavior seen in the performance plots. It was also observed that the C_p distribution of the aft element does not vary significantly with α . The fore element acts as a turning vane, such that the aft element sees the same flow conditions independent of α until stall. However, after stall the C_p distribution across the aft element shifts in the negative C_p direction as a direct result of the loss of lift produced by the fore element.

Fluorescent oil surface flow visualization³² was also performed on the S414 airfoil model in its baseline configuration at $Re = 1.8 \times 10^6$, and $M = 0.18$ at $\alpha = 0^\circ$ and $\alpha = 15^\circ$. At $\alpha = 0^\circ$, the flowfield is fairly uniform, indicating the presence of a laminar boundary layer across most of the fore element upper surface. At roughly $x/c = 0.75$, the change in the oil droplet patterns indicate transition has occurred on the fore element upper surface. The LSB can also be seen quite clearly on the aft element upper surface, in the same location identified at $Re = 1.0 \times 10^6$, $M = 0.10$ in Fig. 3.14. At $\alpha = 15^\circ$, the flowfield has well defined streaking oil droplet structures, indicating turbulent flow across most of the fore-element upper surface. The effects of the large leading edge suction peak from $x/c = 0.0$ to approximately $x/c = 0.20$ can also be seen. The LSB can be seen once again on the aft-element upper surface, with turbulent flow present downstream. It should be noted that for both $Re = 1.8 \times 10^6$, $M = 0.18$ oil surface flow visualization cases, a portion of contact paper was prone to slight separation off the aft element leading edge. This resulted in the typically laminar boundary layer being immediately tripped to turbulent, which can be seen to disrupt the LSB. Due to the location of the contact paper separation and the geometric constraints of the slot between the fore and aft element, the contact paper could not be reapplied in between tests. Both the oil flow visualization images and the C_p distribution at each respective angle of attack can be seen in Fig. 3.18 and Fig. 3.19.

3.5.2 Case 1

The S414 aft element was repositioned into the Case 1 configuration and the plain flap was deflected from $\delta_f = 0^\circ$ to $\delta_f = 20^\circ$ in 5° intervals. Fig. 3.20 shows a performance comparison between the S414 airfoil model and the Case 1 airfoil rigging. For this configuration, $C_{l,max}$ increased by 0.145 (7.3%) relative to the baseline configuration to reach 2.15, and the stall angle of attack decreased to $\alpha_{stall} = 15.4^\circ$. The zero-lift angle of attack was found to be $\alpha_{zl} = -7.1^\circ$. The lift curve slope also decreased due to separation off the aft element present throughout the α schedule, as demonstrated by a plot of the C_p distribution at $\alpha = 5^\circ$ in Fig. 3.20. The sharp leading edge of the aft element results in the formation of a large suction peak along with an aggressive adverse pressure gradient. While the flow remained attached along the aft-element upper surface throughout the slot due to the turning vane influence mentioned previously, at the exit of the slot a constant-pressure plateau was produced across the aft element upper surface, indicating separated flow. The result of deflecting the plain flap in this configuration can be seen in Fig. 3.20. Similar to the baseline case, the plain flap works to shift the lift curve in the positive C_l and negative α direction. The $\delta_f = 20^\circ$ case resulted in the highest lift coefficient of $C_{l,max} = 2.32$, a $\Delta C_{l,max}$ of 0.32 and 16% increase in $C_{l,max}$ when compared to the baseline S414 configuration.

3.5.3 Case 2

Tests were also performed with the aft element in the Case 2 configuration. As seen in Fig. 3.21, $C_{l,max}$ greatly increased to 2.43, marking a 0.43 (21.5%) improvement over the baseline S414 configuration. The stall angle of attack was $\alpha_{stall} = 15.4^\circ$ and the zero-lift angle of attack was $\alpha_{zl} = -6.0^\circ$. At about $\alpha = 5^\circ$, the lift curve slope increased then remained constant until stall. Fig. 3.21 also shows the C_p distribution at $\alpha = 5^\circ$ compared to the S414 baseline configuration. Similar to the aft-element pressure distribution of the Case 1 rigging, there is a pressure drop at the leading edge of the aft element. The air flowing over the aft element begins to recover from the leading-edge suction peak until it encounters and mixes with the flow discharged off the fore element trailing edge. This provides a momentum injection to the air flowing over the aft element upper surface, which creates a favorable pressure gradient sufficient to keep the flow attached across the entire aft element. In addition, the air discharged off the fore element trailing edge flowed into a region of low pressure, allowing the dumping velocity of the fore element to be increased. This effect led to large gains in ΔC_p on the fore element, resulting in greater lift production. Typical

plain flap deflection behavior is observed in the lift curve slopes; however, the plain flap became marginally effective after $\delta_f = 10^\circ$. The highest $C_{l,max}$ is still observed at $\delta_f = 20^\circ$, where $C_{l,max} = 2.57$, a $\Delta C_{l,max} = 0.57$ (28.5%) increase over the S414.

3.5.4 Case 3

The aft element was repositioned into the Case 3 rigging and tested. The lift curve and C_p distribution were plotted against the S414 baseline configuration and can be seen in Fig. 3.22. The maximum lift coefficient was observed to be $C_{l,max} = 2.45$ and occurred at $\alpha_{stall} = 15.4^\circ$. This marks an increase in $C_{l,max}$ of 0.45 (22.5%) over the original configuration. The zero lift angle of attack decreased to $\alpha_{zL} = -7.1^\circ$. At approximately $\alpha = 5^\circ$, the lift curve becomes nonlinear until stall, which was observed to be more abrupt than the original S414. The C_p distribution is nearly identical to that observed for Case 2. This case also increased the dumping velocity of the fore element, resulting in an increased ΔC_p across the fore element and a favorable pressure gradient across the upper surface of the aft element. Deflecting the plain flap resulted in similar trends as observed in Case 2, with each deflection providing a gradual decrease in flap effectiveness. The largest maximum lift coefficient, $C_{l,max} = 2.64$, occurred when $\delta_f = 20^\circ$, marking a 0.64 (32%) increase over the baseline.

3.5.5 Case 4

The Case 4 configuration was also tested. As seen in Fig. 3.23, this case provided the greatest $C_{l,max}$ with no flap deflection, reaching $C_{l,max} = 2.54$. This marks a 0.54 (27%) increase over the S414 $C_{l,max}$. The stall angle of attack and zero lift angle of attack both decreased, with $\alpha_{stall} = 14.4^\circ$ and $\alpha_{zL} = -7.8^\circ$. The lift curve is observed to exhibit multiple nonlinear breaks, most likely as a result of flow separation and attachment. Before $\alpha = -4.7^\circ$, the flow has not attached to the airfoil model lower surface. After $\alpha = -4.7^\circ$, the flow is fully attached across the fore element, but has a region of separation across the aft element upper surface beginning at roughly $x/c = 0.95$. At $\alpha = 4.1^\circ$, the lift curve becomes nonlinear again until $\alpha = 9.2^\circ$, after which it returns to its original lift curve slope until stall. The C_p distribution mimics the previous Case 3 configuration, but the higher δ_{aft} resulted in greater ΔC_p across both the fore and aft element. The plain flap deflections drive $C_{l,max}$ to the highest in any setting of all the riggings tested, with $C_{l,max}$ reaching 2.68 at $\alpha_{stall} = 13.4^\circ$ and $\delta_f = 20^\circ$. This condition corresponds to a 0.68 (0.34%) increase in $C_{l,max}$ compared to the S414.

3.5.5 Case 5

After testing Cases 1 through 4, it was found that even the most aggressive rigging, Case 4, continued to generate performance gains compared to the other configurations. Thus, a fifth and even more aggressive alternative aft element rigging was designed using knowledge gained from the experimental data acquired through testing Cases 1 through 4. In order to reduce or eliminate completely the region of pressure recovery at the leading of the aft element for Case 4, the aft element overhang was decreased. In addition, the aft element deflection angle was increased to values resembling typical small to medium-sized commercial aircraft take-off flap settings. The aft element repositioned into the Case 5 setting can be seen in Fig. 3.8, and geometric values are listed in Table 3.1.

Performance plots for Case 5 can be seen in Fig. 3.24. The maximum lift coefficient achieved by Case 5 with no flap deflection was $C_{l,max} = 2.47$, an increase of 0.47 (23.5%) compared to the baseline case, but a slight decrease in performance when compared to Case 4. The stall angle of attack was $\alpha_{stall} = 14.4^\circ$, which was the same as Case 4. The zero lift angle of attack decreased to $\alpha_{zl} = -8.3^\circ$. The lift curve exhibits nonlinear behavior before $\alpha = -4.7^\circ$, after which it remains linear until stall. The reduced overhang did not decrease the adverse pressure gradient at the leading edge of the aft element, but rather increased it. The presence of a larger adverse pressure gradient at the leading edge resulted in a slight decrease in ΔC_p across the aft element. This resulted in a decrease in the dumping velocity of the fore element, explaining the decrease in $C_{l,max}$ observed in the lift curve.

3.6 Chapter 3 Tables and Figures

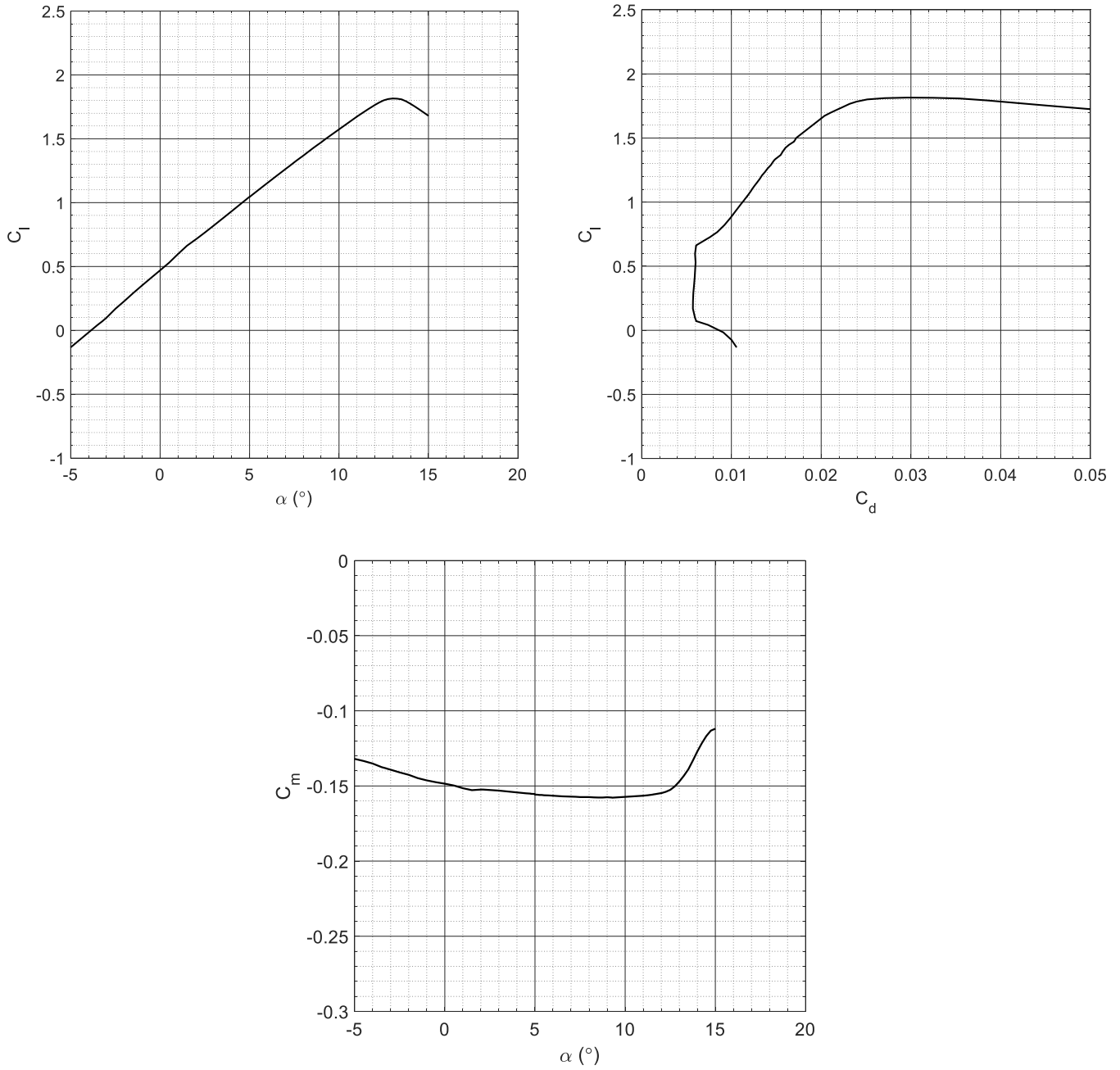


Fig. 3.1 Theoretical performance predictions generated by MSES at $Re = 1.5 \times 10^6$, $M = 0.17$.

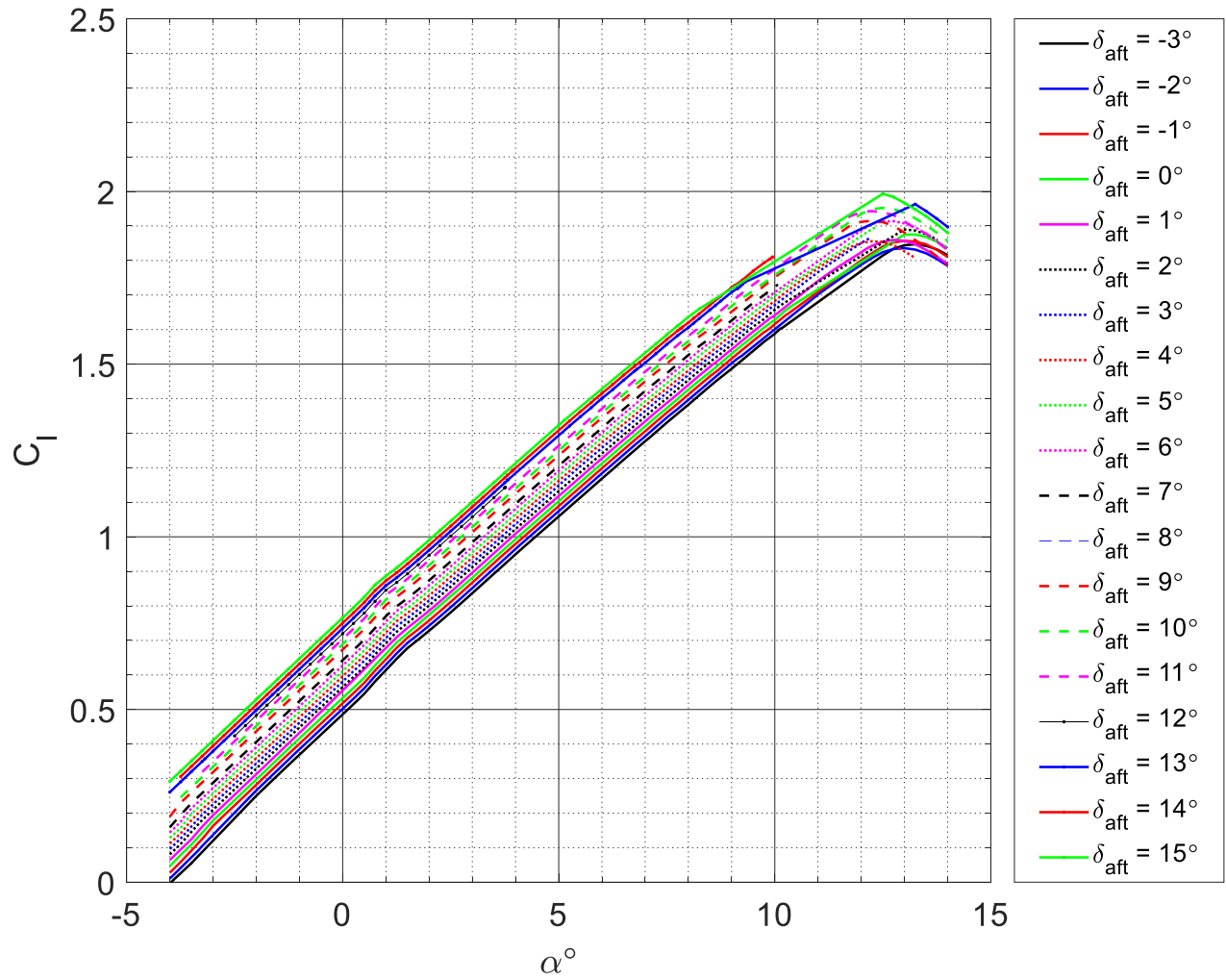


Fig. 3.2 MSES results for the slot-based approach at $Re = 1.5 \times 10^6$, $M = 0.17$, $\delta_f = 0^\circ$.

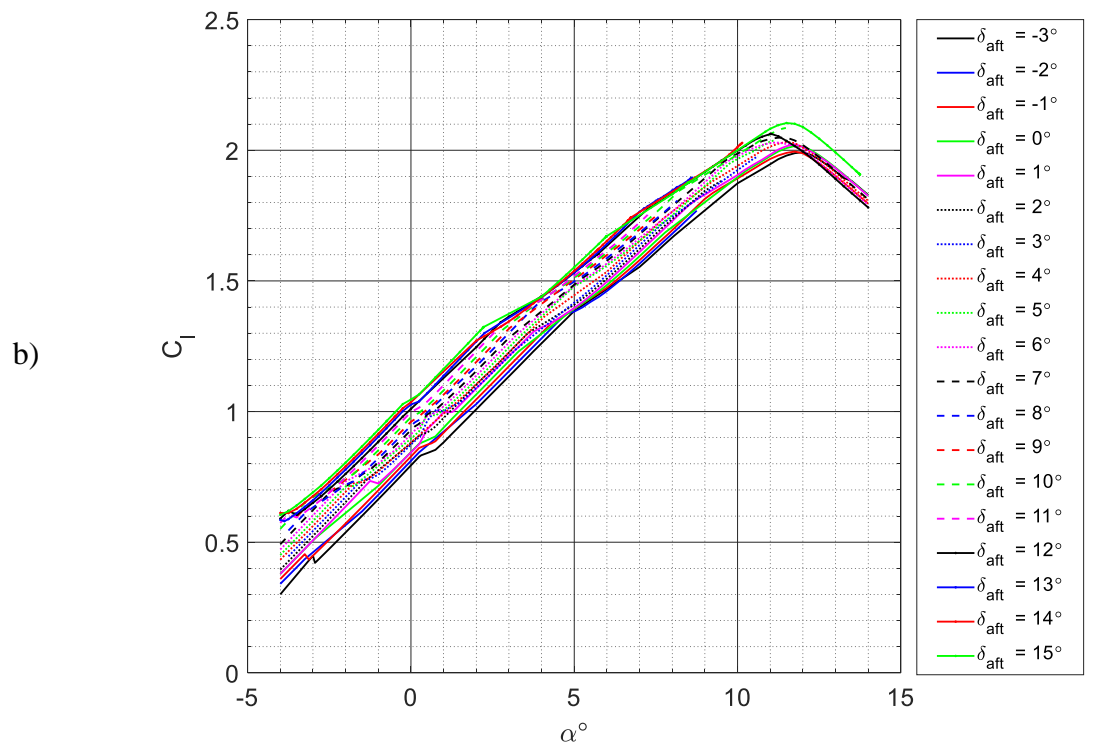
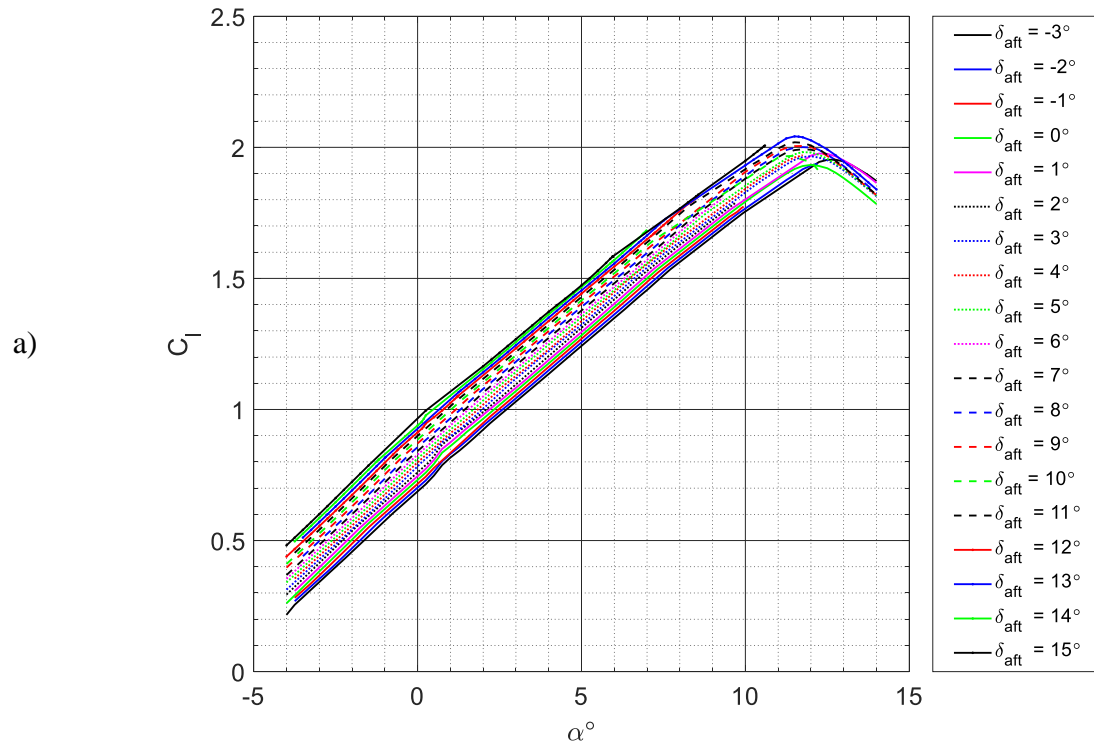


Fig. 3.3 MSES results for the slot-based approach for a) $\delta_f = 5^\circ$ and b) $\delta_f = 10^\circ$ at $Re = 1.5 \times 10^6$, $M = 0.17$.

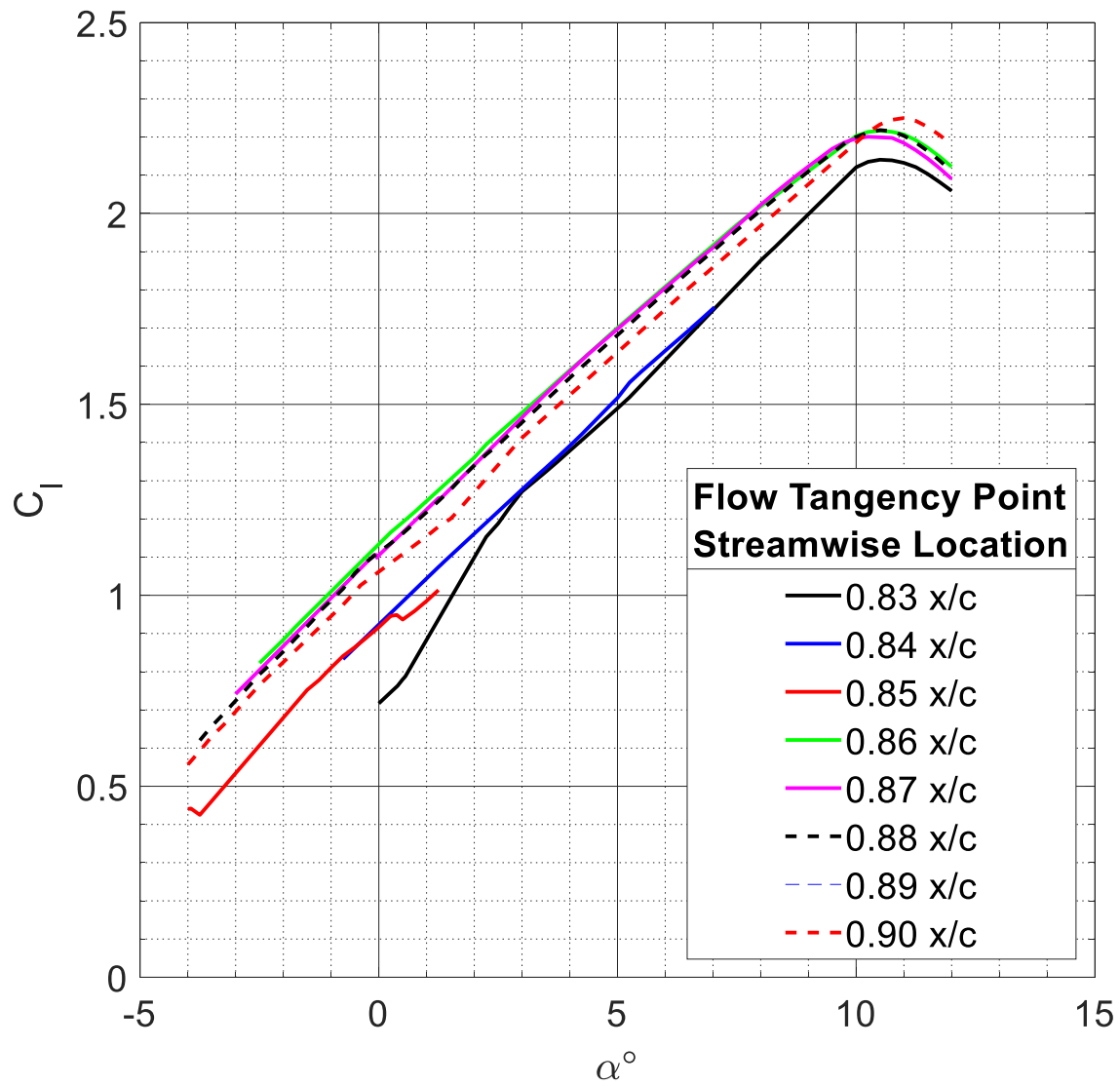
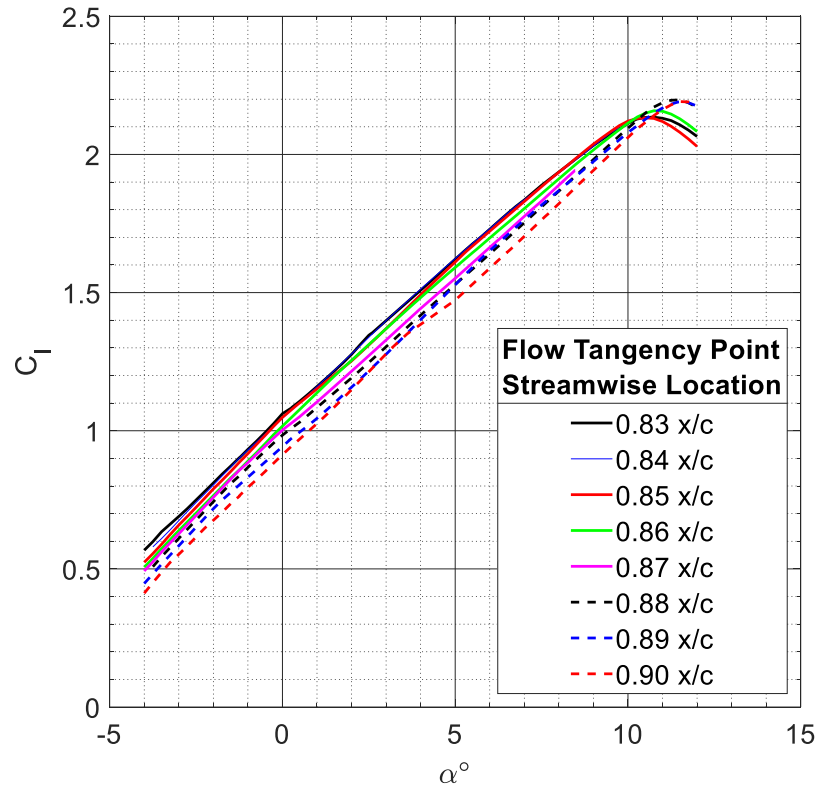


Fig. 3.4 MSES results for the dumping velocity-based approach at $Re = 1.5 \times 10^6$, $M = 0.17$, $\delta_f = 0^\circ$.

a)



b)

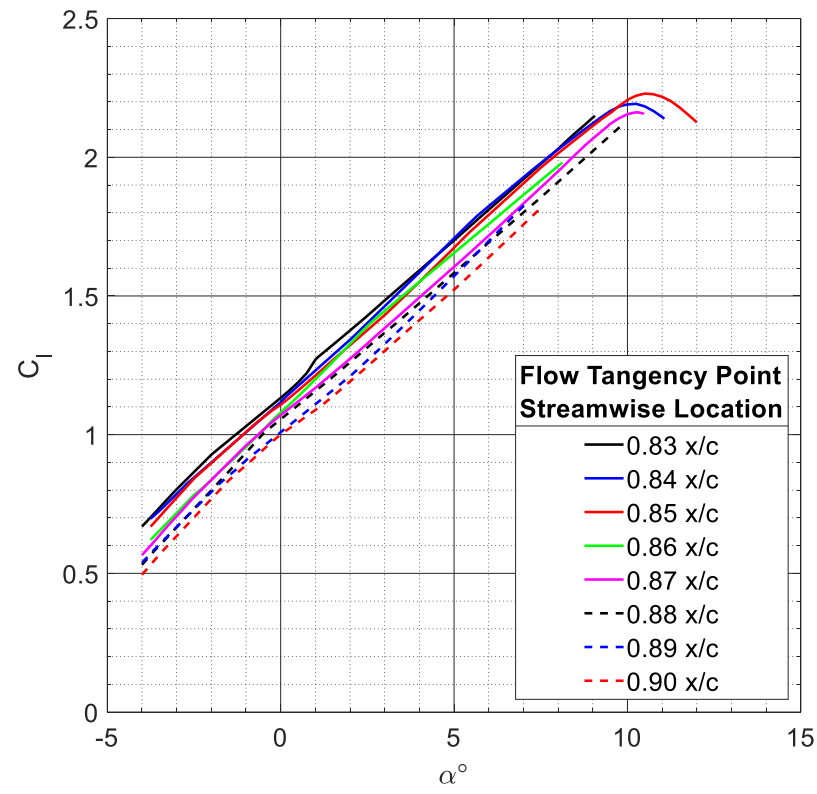


Fig. 3.5 MSES results for the dumping velocity-based approach for a) $\delta_f = 5^\circ$ and b) $\delta_f = 10^\circ$ at $Re = 1.5 \times 10^6$, $M = 0.17$.

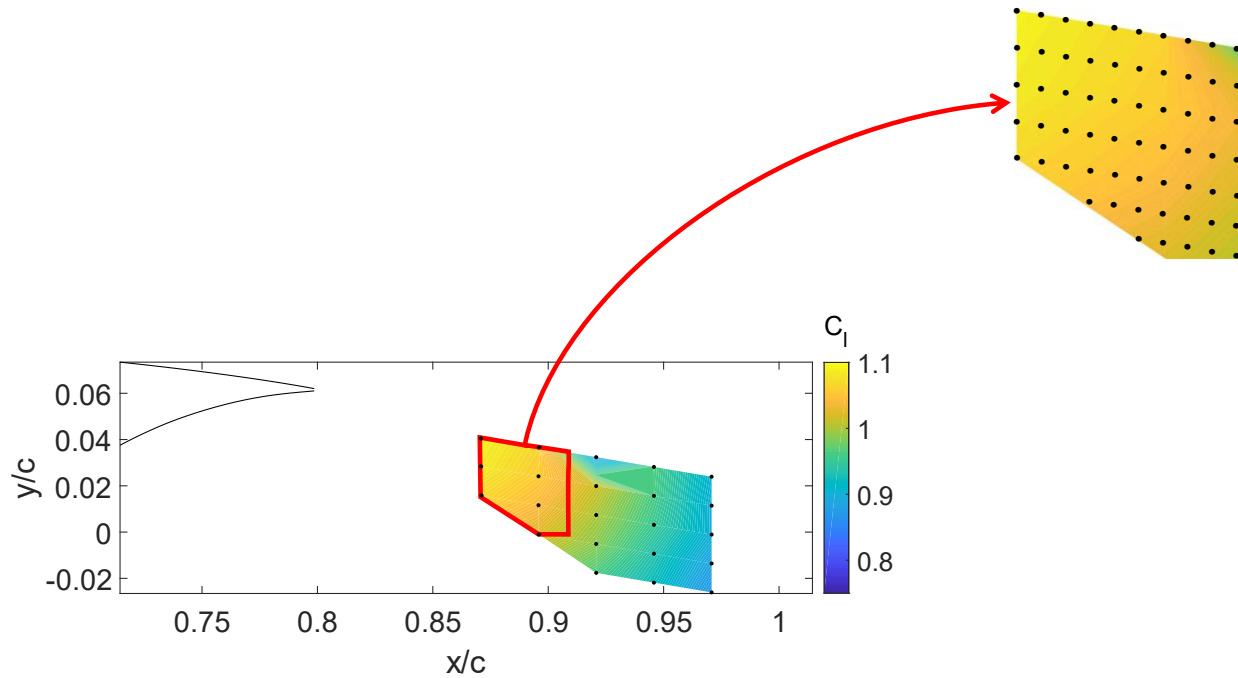


Fig. 3.6 Sample C_l contour map generated using the expanded dumping-velocity approach that demonstrates how regions of high performance were iteratively identified.

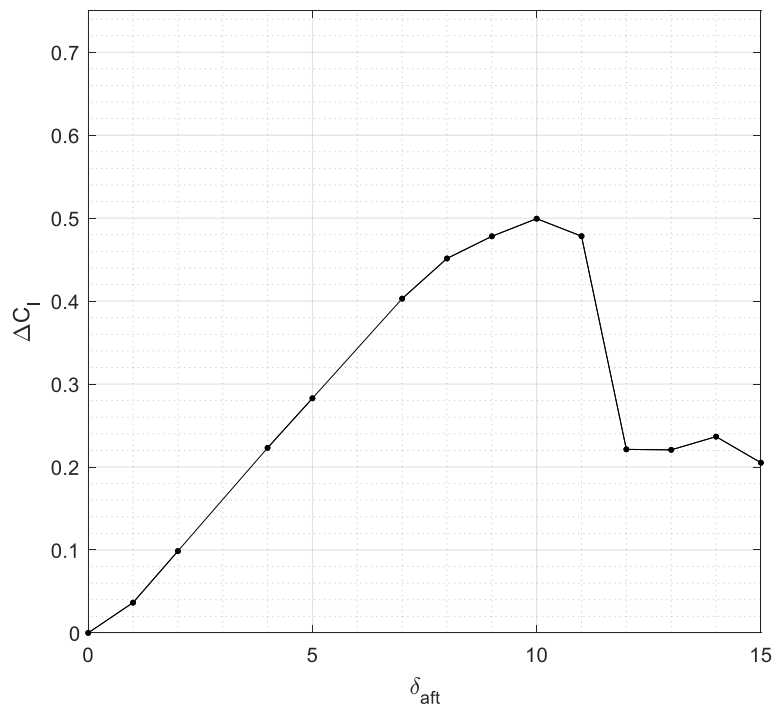


Fig. 3.7 Sample aft-element effectiveness plot generated by the expanded dumping-velocity approach.

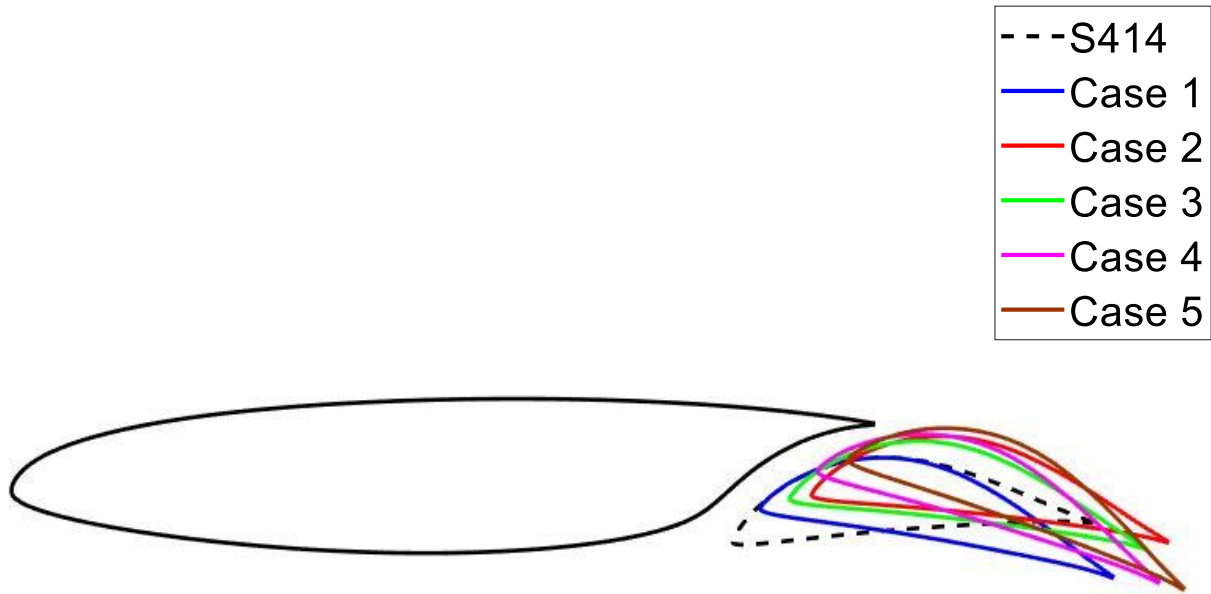


Fig. 3.8 Alternate positions for the S414 aft element.

Table 3.1 Alternate aft-element positions compared to the gap (x/c), overhang (x/c), and aft-element deflection angle ($^\circ$) of the S414.

	Approach	Gap	Overhang	δ_{aft}
S414	-	0.304	0.132	-3.0°
Case 1	Slot	0.031	0.106	11.0°
Case 2	Dumping Velocity	0.021	0.059	7.4°
Case 3	Expanded Dumping Velocity	0.020	0.079	8.0°
Case 4	Expanded Dumping Velocity	0.014	0.054	18.0°
Case 5	Empirical	0.015	0.025	21.0°

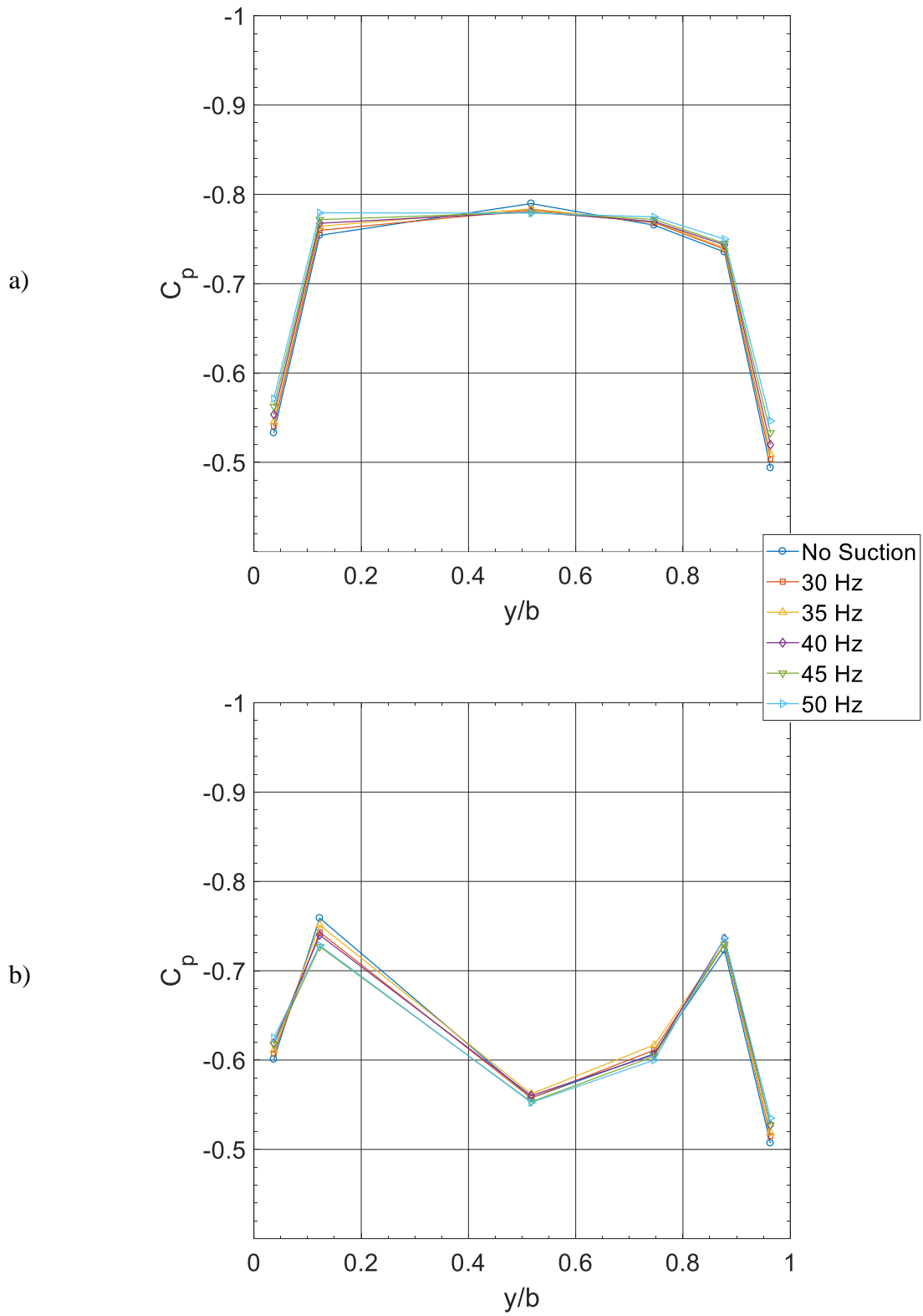


Fig. 3.9 Aft element spanwise pressure distributions for various VFD operating frequencies for a) $\alpha = 5^\circ$ and b) $\alpha = 15^\circ$ at $Re = 1.8 \times 10^6$, $M = 0.18$.

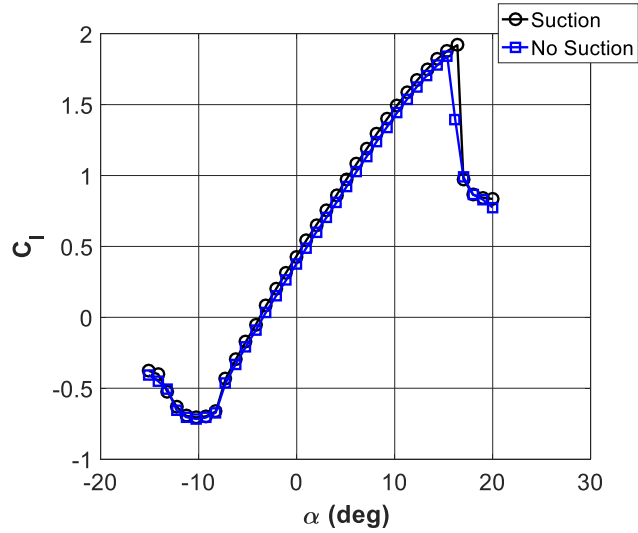


Fig. 3.10 Lift-curve comparison with the suction system on (VFD at 45 Hz) and off at $Re = 1.0 \times 10^6$, $M = 0.10$

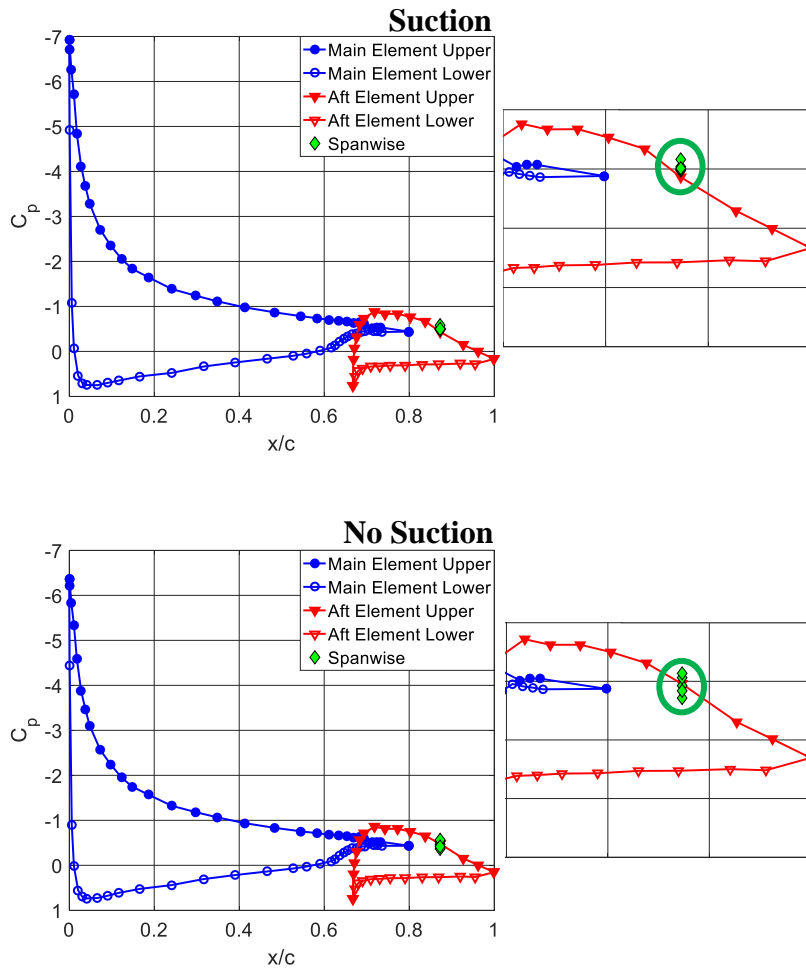


Fig. 3.11 C_p comparison with the suction system on (VFD at 45 Hz) and off at $Re = 1.0 \times 10^6$, $M = 0.10$.

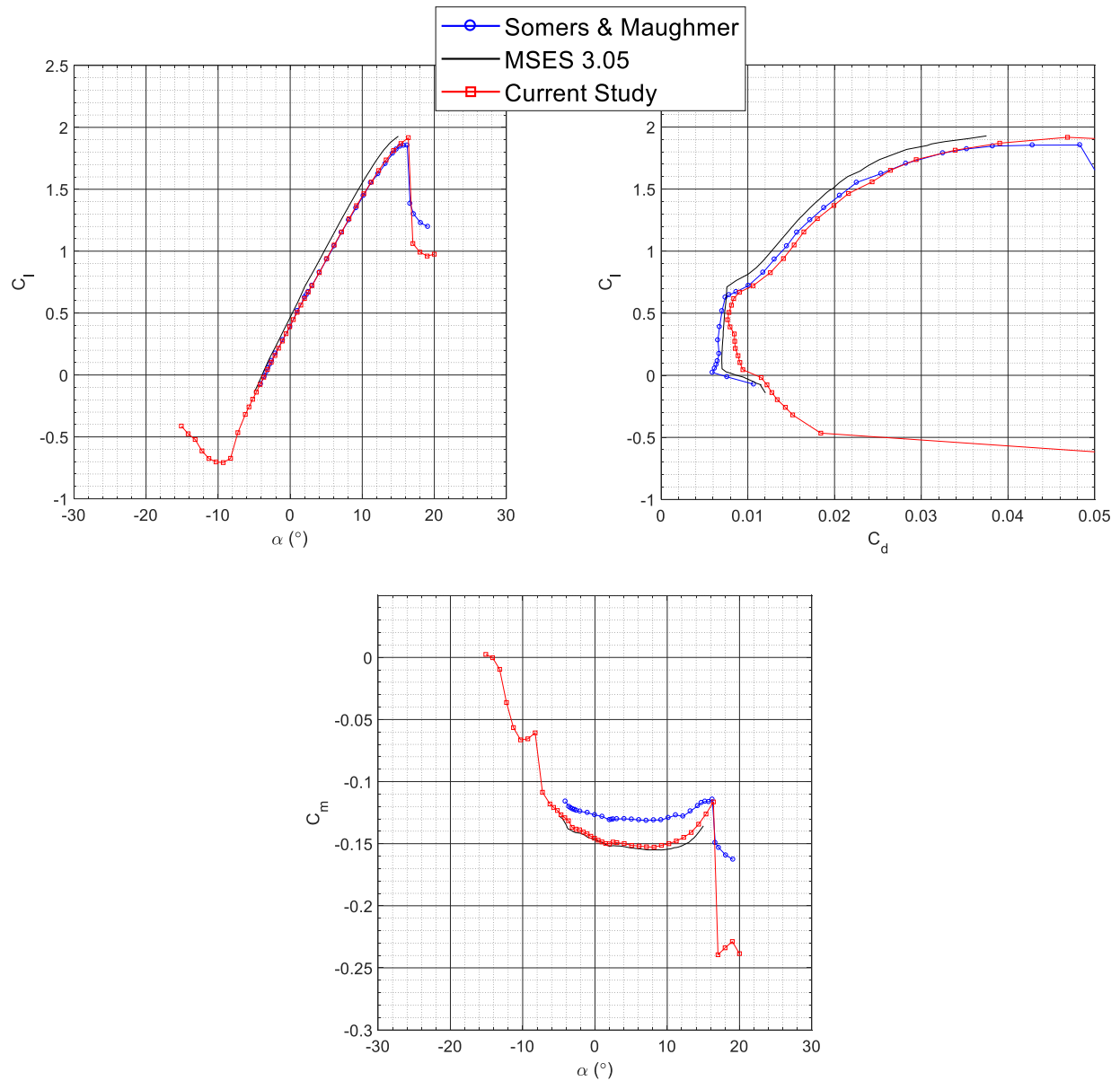


Fig. 3.12 Comparison of S414 performance data from the current study to Somers & Maughmer⁸ and MSES 3.05¹⁴ at $Re = 1.0 \times 10^6$, $M = 0.10$.

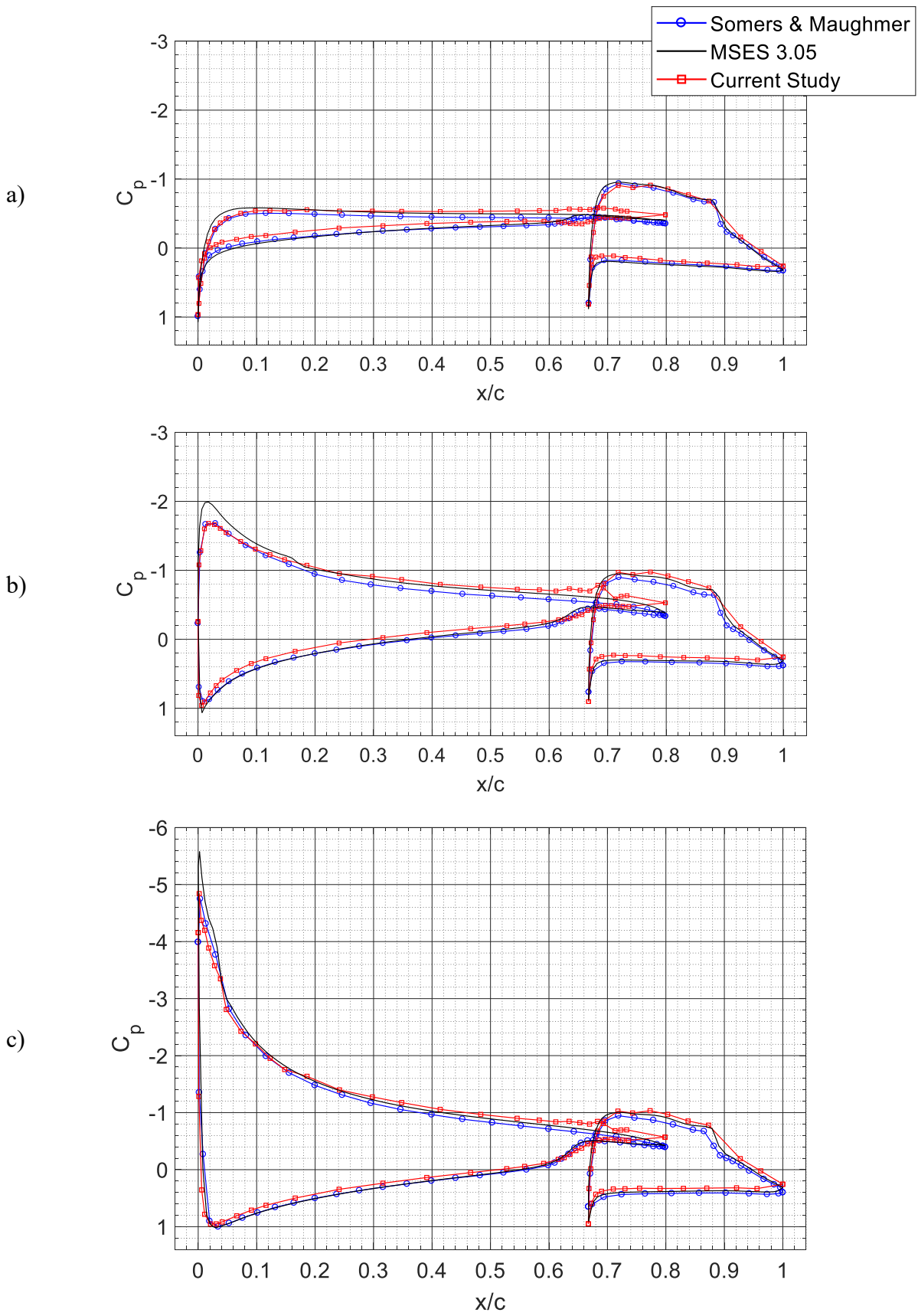


Fig. 3.13 Comparison of S414 C_p data from the current study to Somers & Maughmer⁸ and MSES 3.05¹⁴ for a) $\alpha = 0^\circ$, b) $\alpha = 5^\circ$, c) $\alpha = 10^\circ$, d) $\alpha = 15^\circ$ at $Re = 1.0 \times 10^6$, $M = 0.10$.

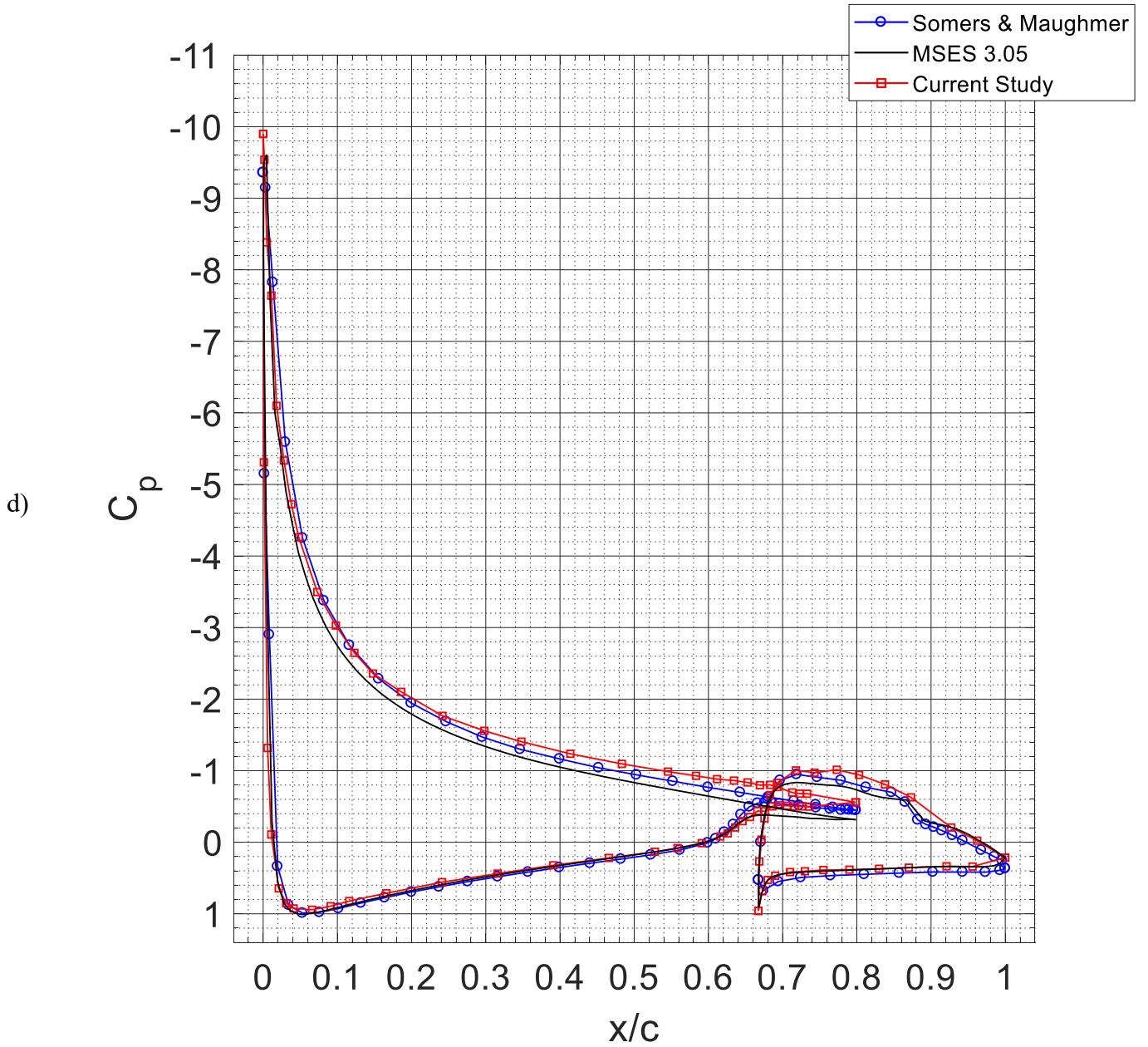


Fig. 3.13 (cont.) Comparison of S414 C_p data from the current study to Somers & Maughmer⁸ and MSES 3.05¹⁴ at a) $\alpha = 0^\circ$, b) $\alpha = 5^\circ$, c) $\alpha = 10^\circ$, d) $\alpha = 15^\circ$ at $Re = 1.0 \times 10^6$, $M = 0.10$.

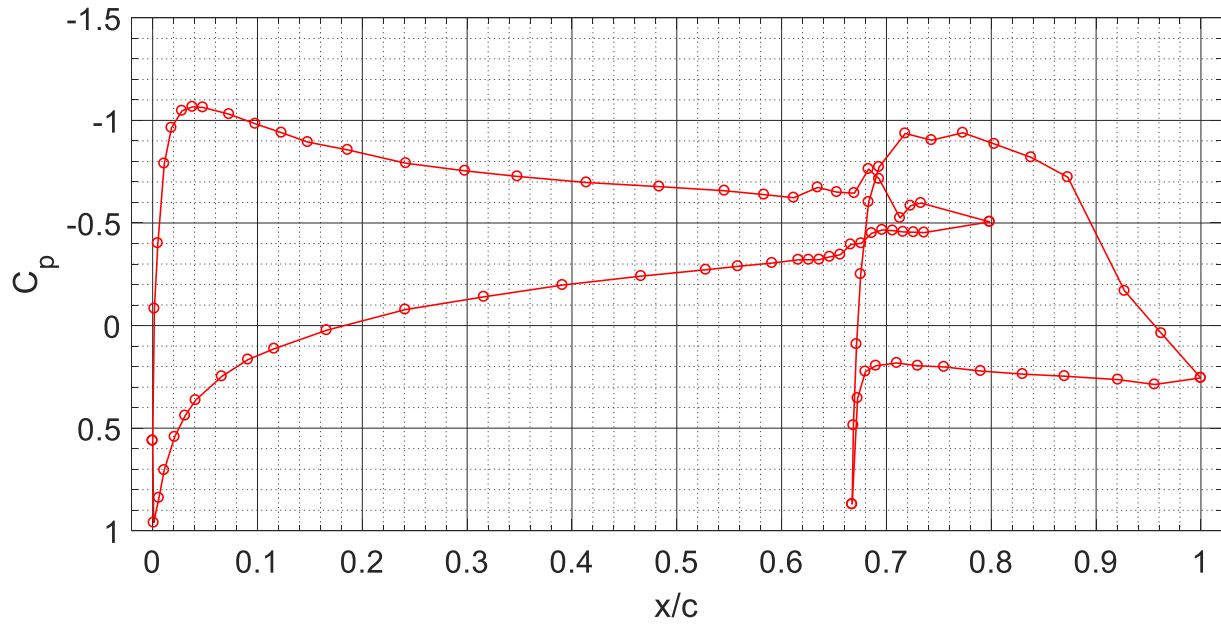
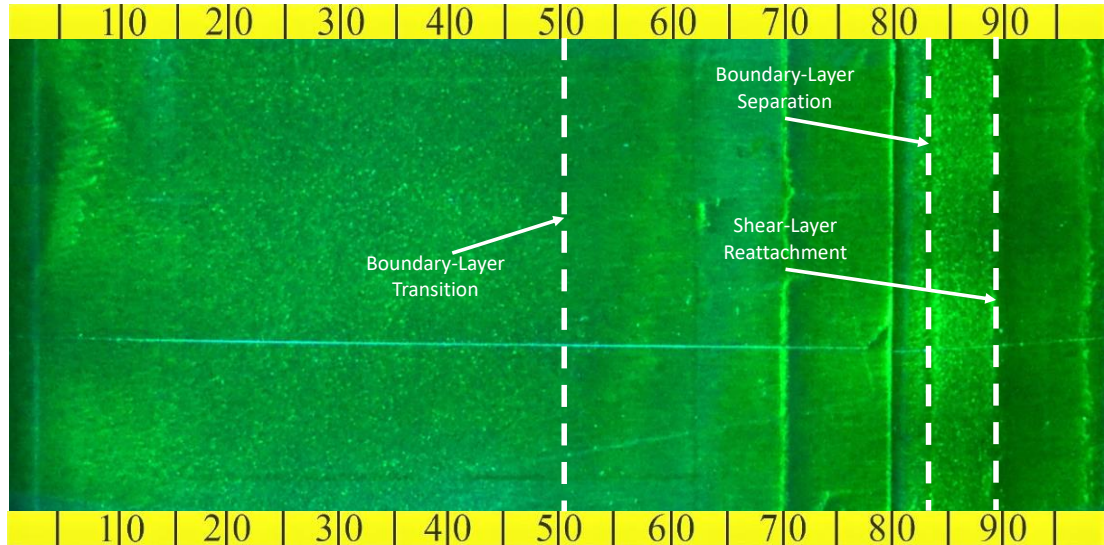


Fig. 3.14 Surface oil flow visualization and the corresponding C_p distribution for $\alpha = 3^\circ$ at $\text{Re} = 1.0 \times 10^6$, $M = 0.10$.

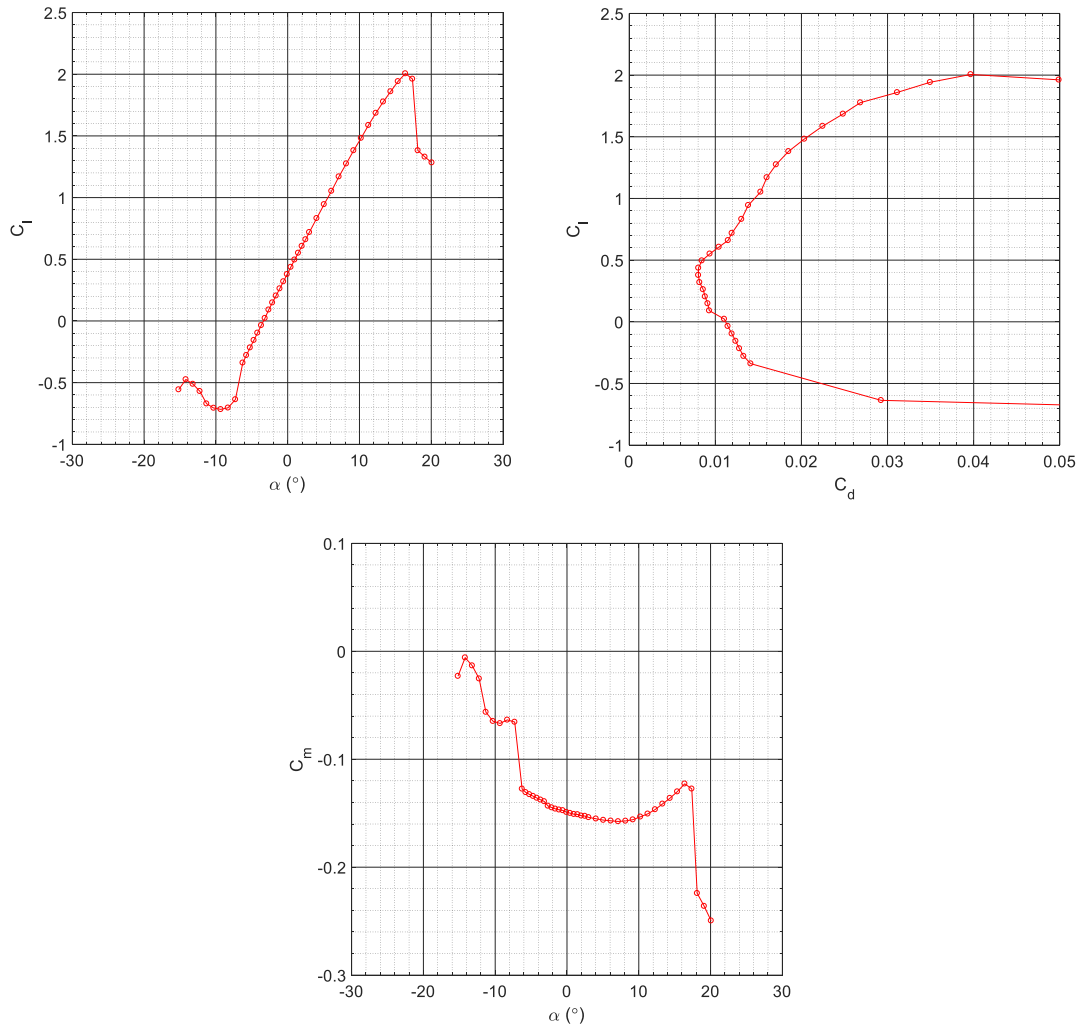


Fig. 3.15 Performance of the S414 airfoil model at $Re = 1.8 \times 10^6$, $M = 0.18$.

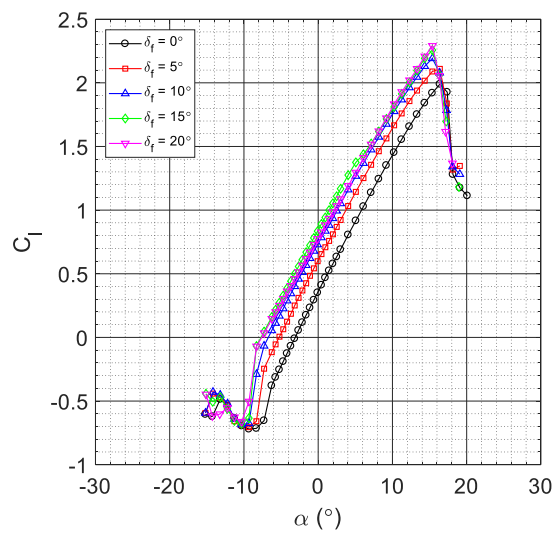


Fig. 3.16 Effect of deflecting the aft element plain flap on C_l at $Re = 1.8 \times 10^6$, $M = 0.18$.

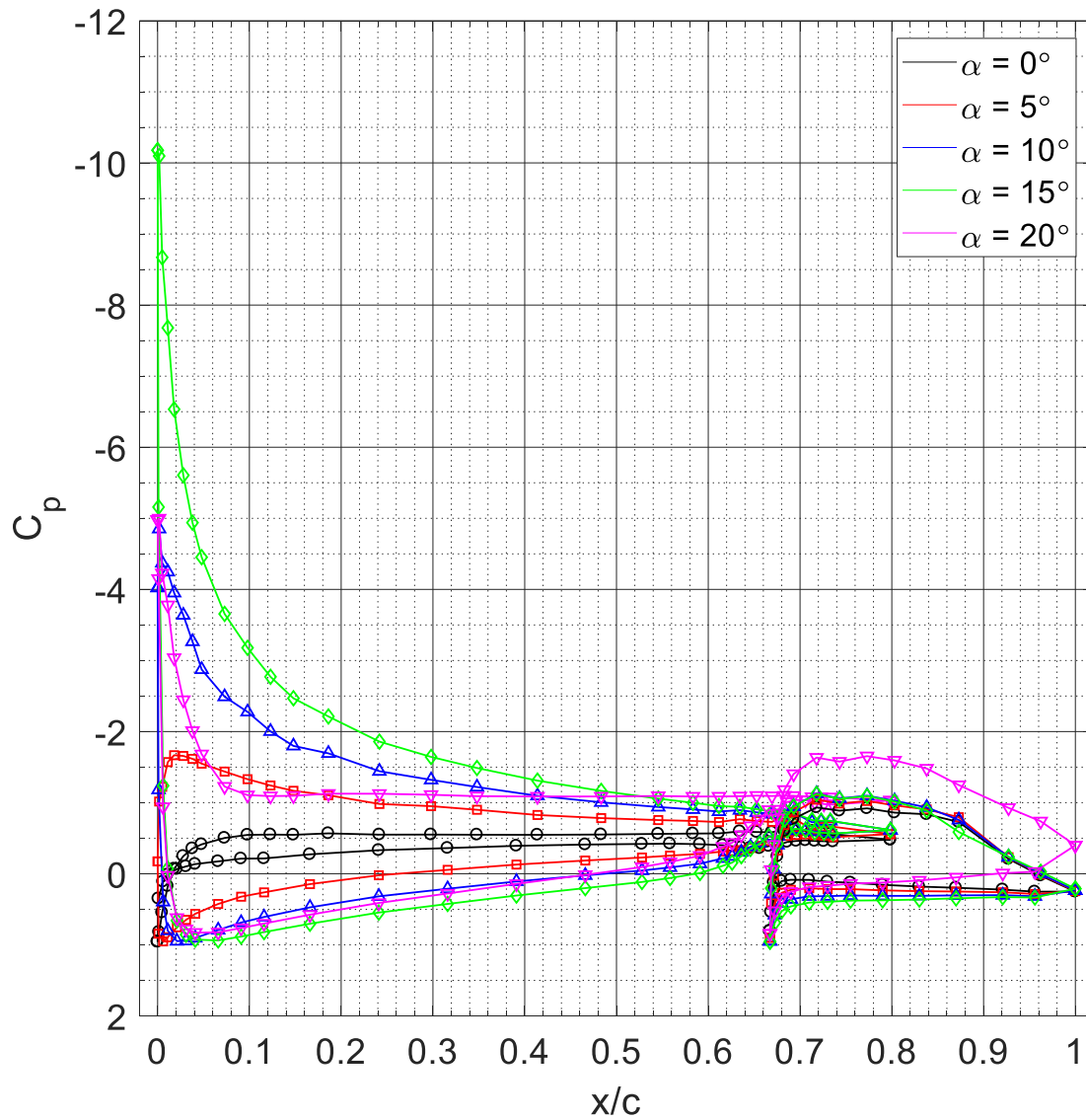


Fig. 3.17 C_p distributions for the S414 at various angles of attack at $Re = 1.8 \times 10^6$, $M = 0.18$.

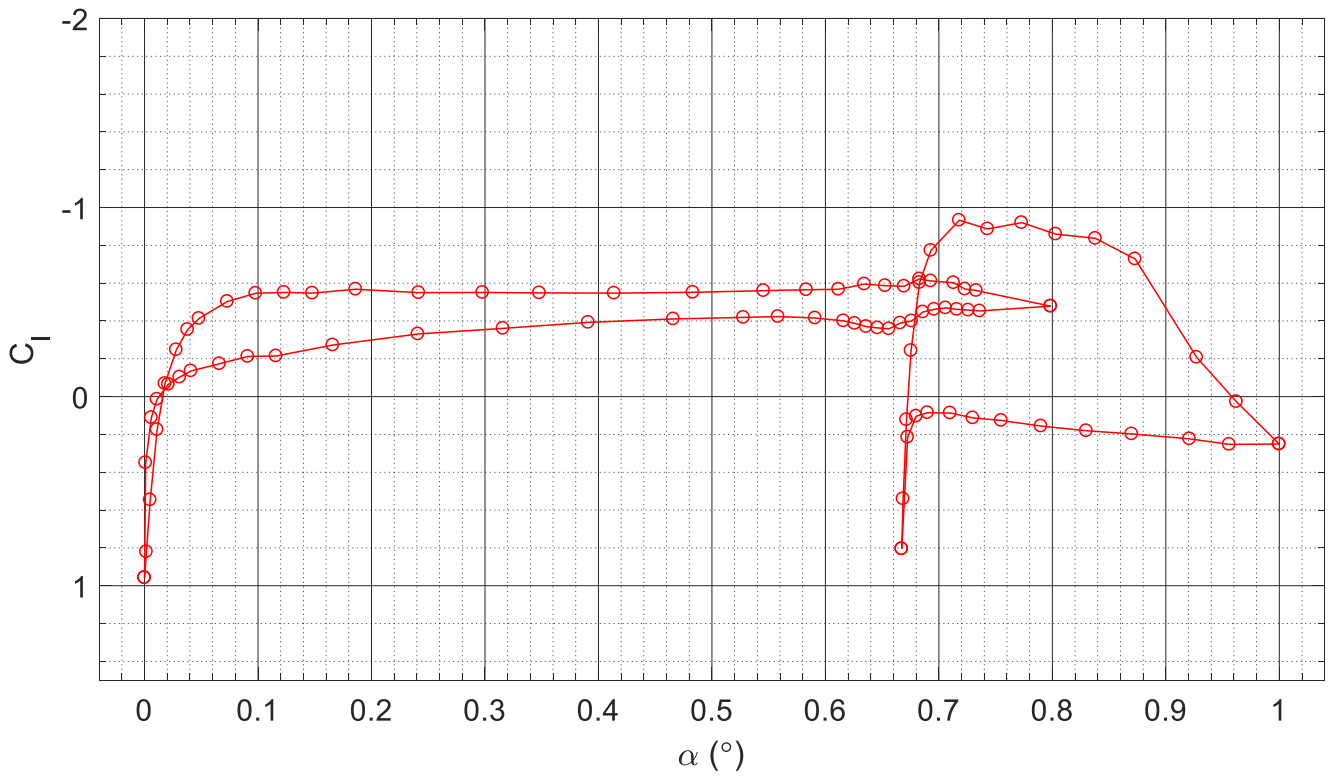
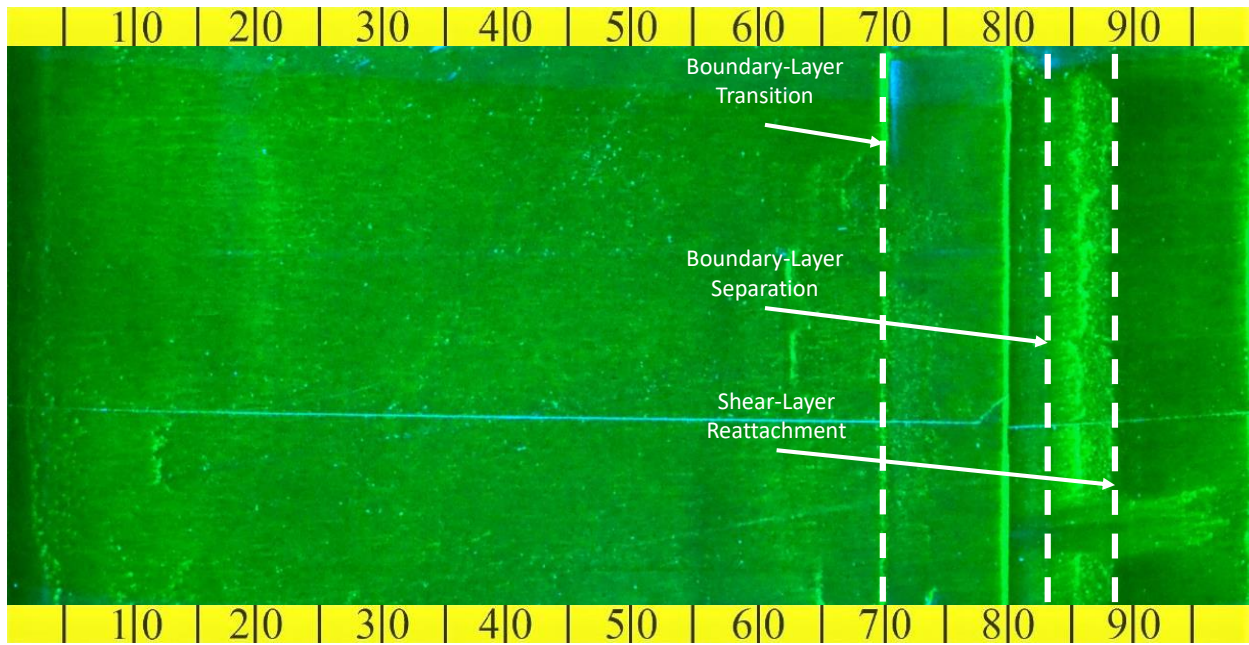


Fig. 3.18 Surface oil flow visualization and the corresponding C_p distribution for $\alpha = 0^\circ$ at $Re = 1.8 \times 10^6$, $M = 0.18$.

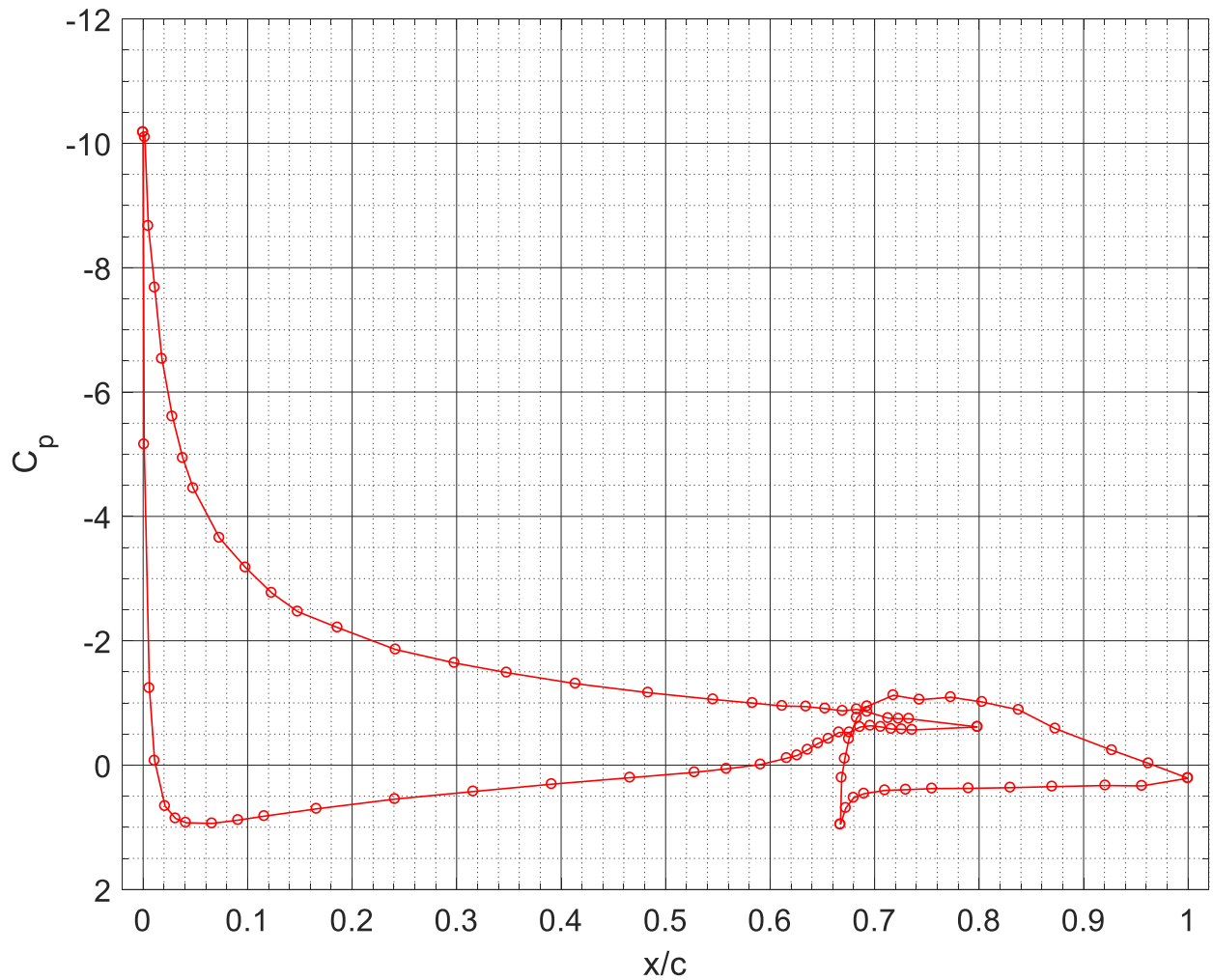
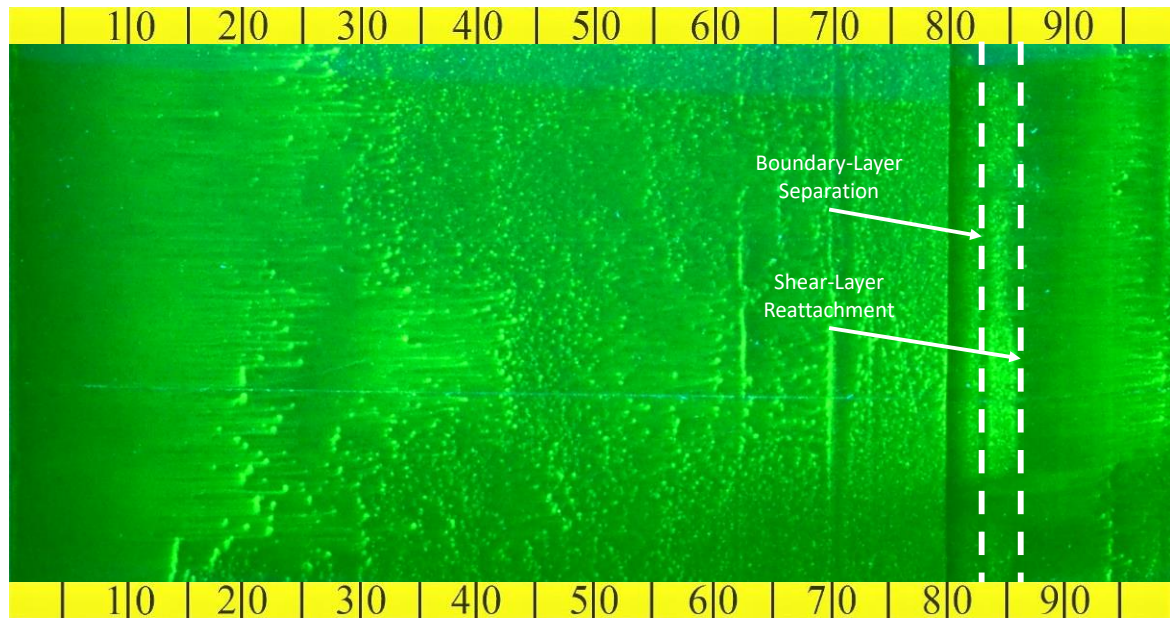


Fig. 3.19 Surface oil flow visualization and the corresponding C_p distribution for $\alpha = 15^\circ$ at $Re = 1.8 \times 10^6$, $M = 0.18$.

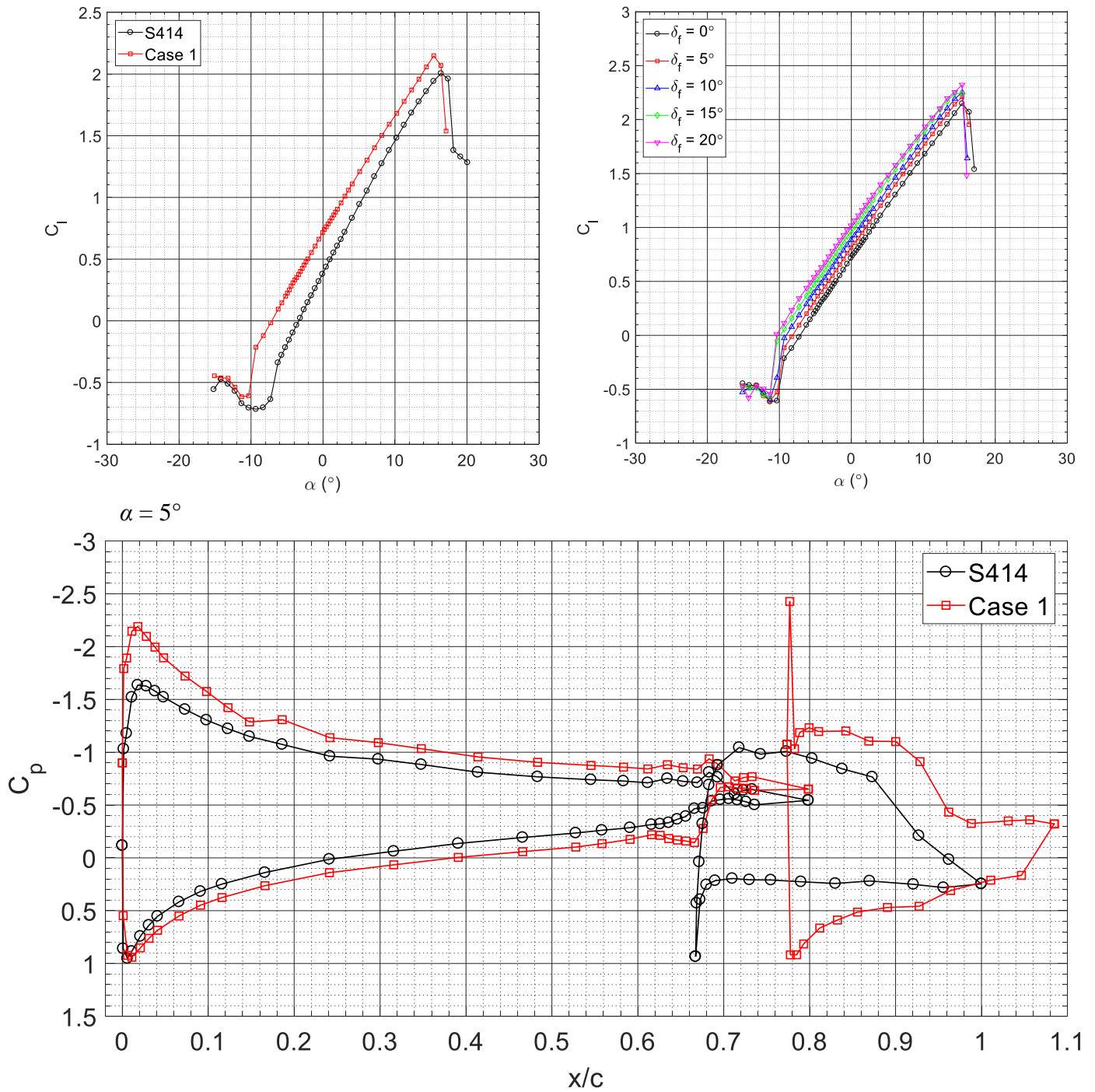


Fig. 3.20 Performance comparison between the S414 airfoil and the Case 1 rigging at $Re = 1.8 \times 10^6$, $M = 0.18$.

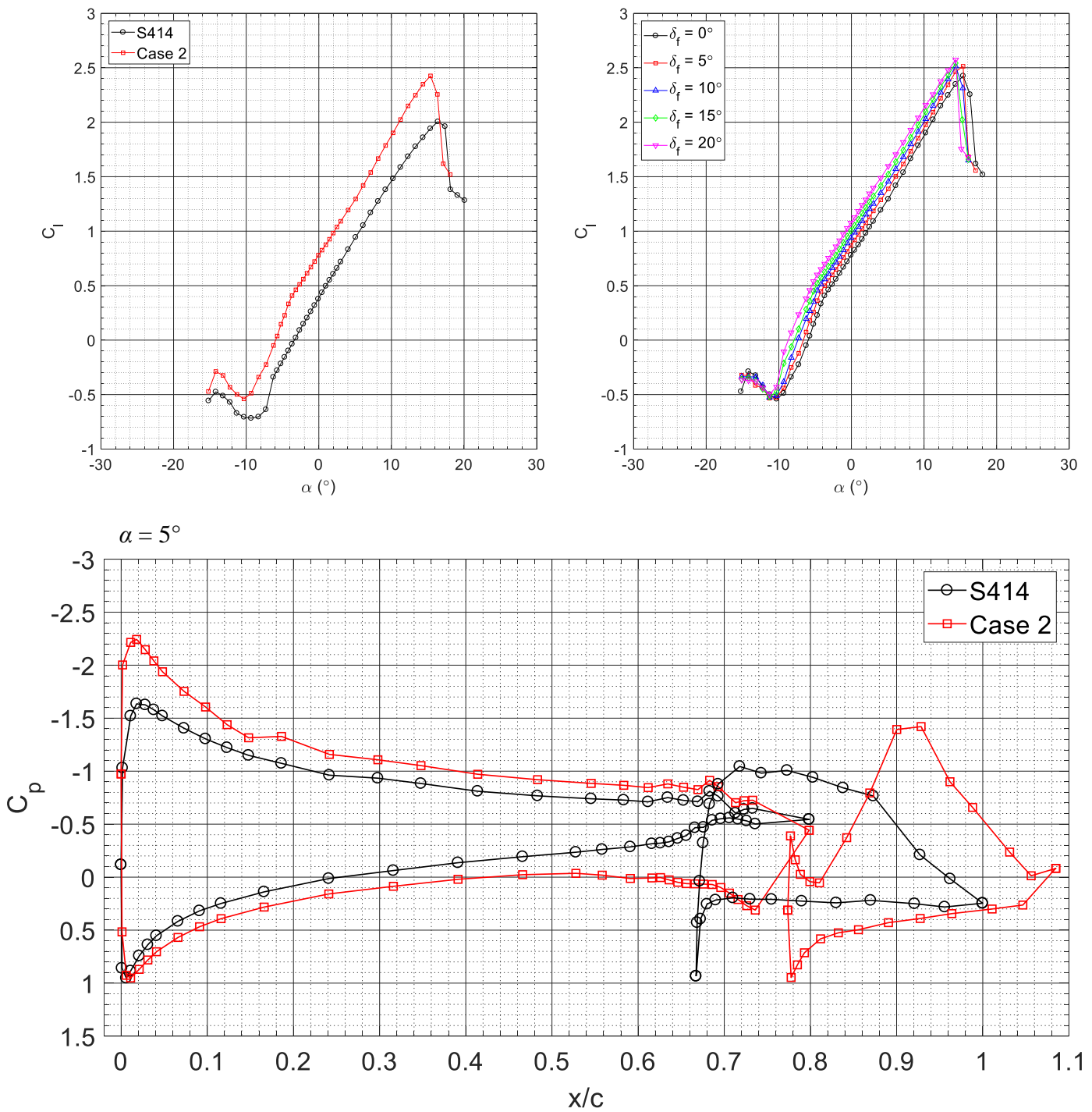


Fig. 3.21 Performance comparison between the S414 airfoil and the Case 2 rigging at $Re = 1.8 \times 10^6$, $M = 0.18$.

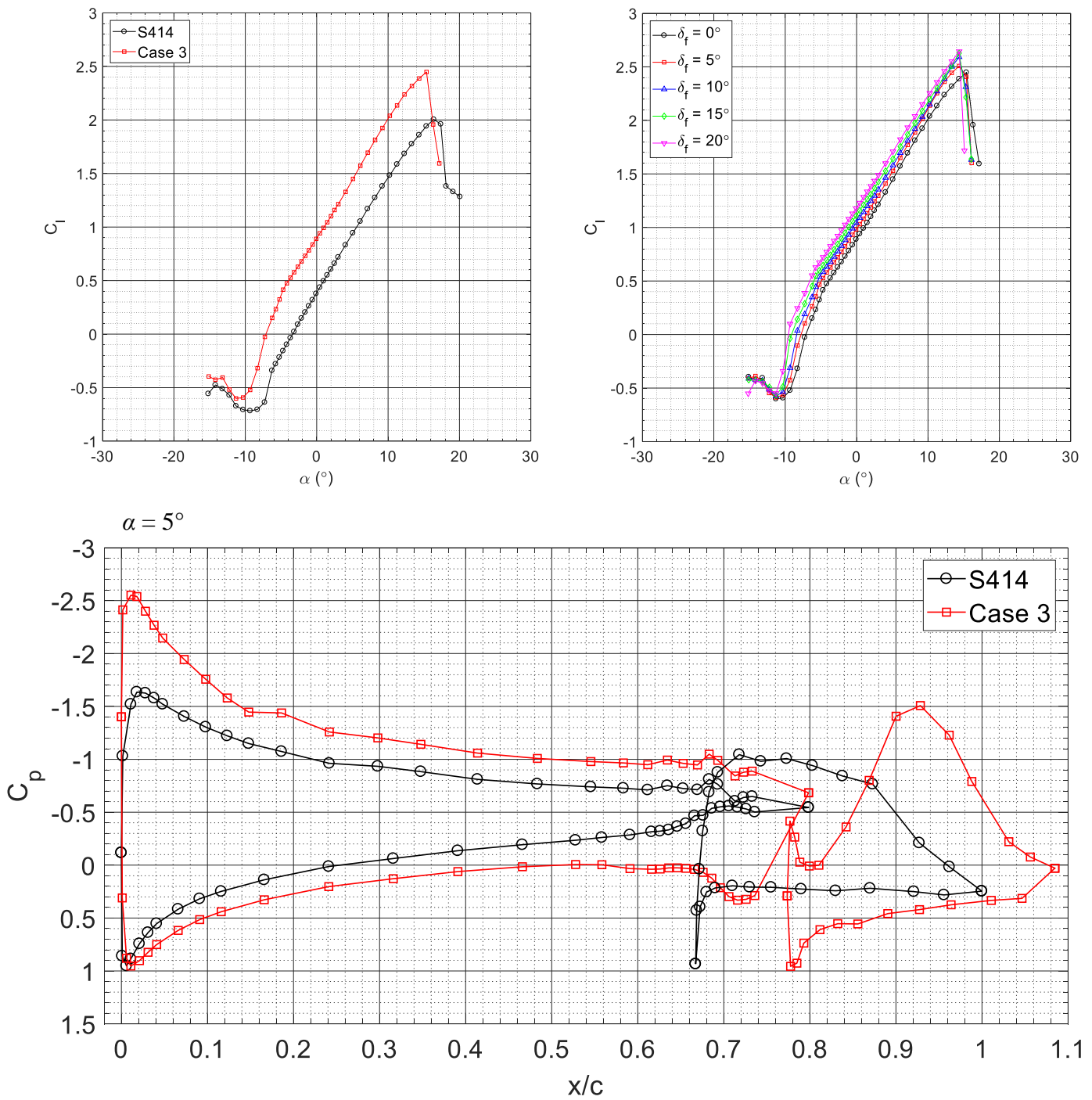


Fig. 3.22 Performance comparison between the S414 airfoil and the Case 3 rigging at $Re = 1.8 \times 10^6$, $M = 0.18$.

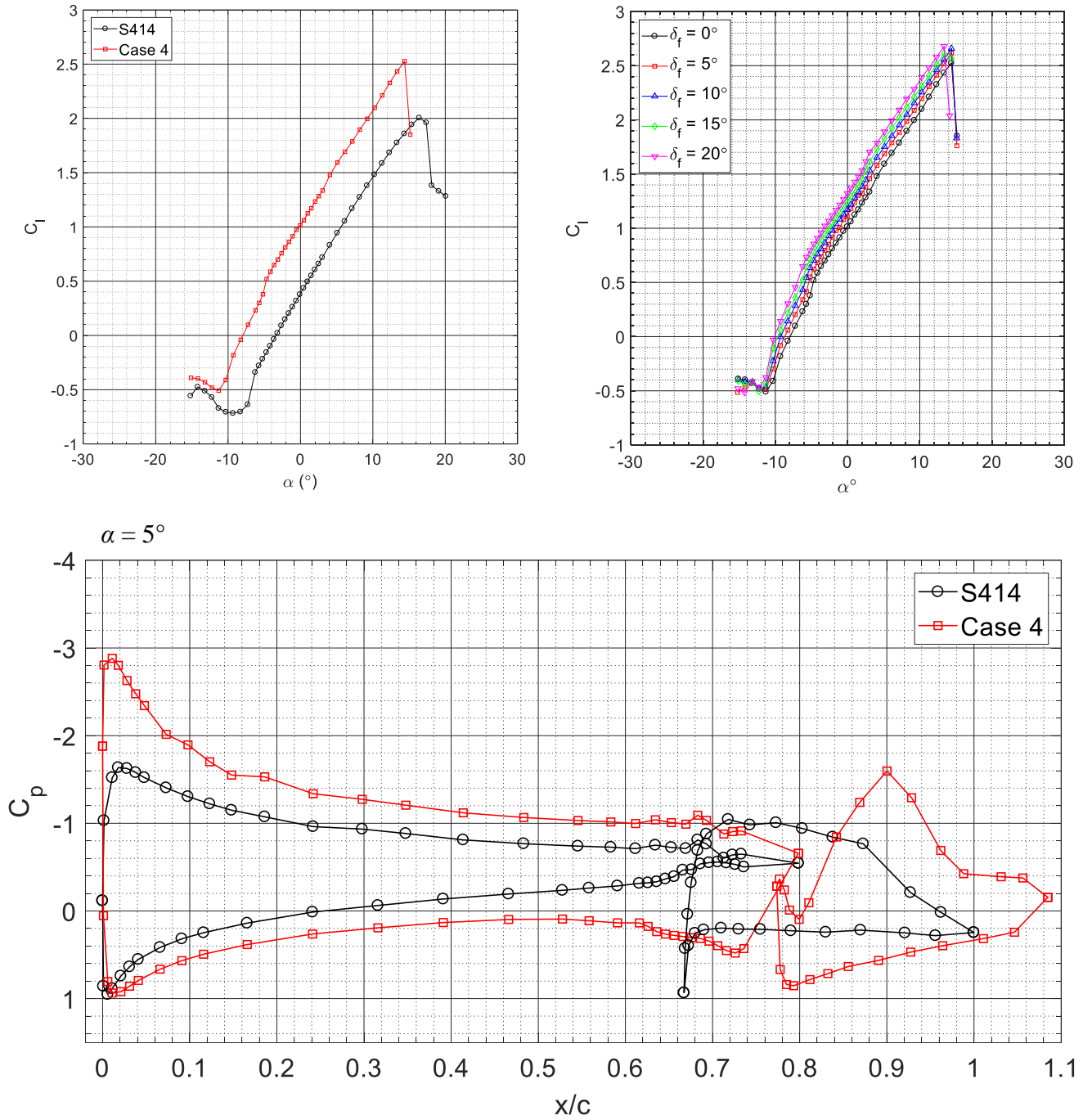


Fig. 3.23 Performance comparison between the S414 airfoil and the Case 4 rigging at $Re = 1.8 \times 10^6$, $M = 0.18$.

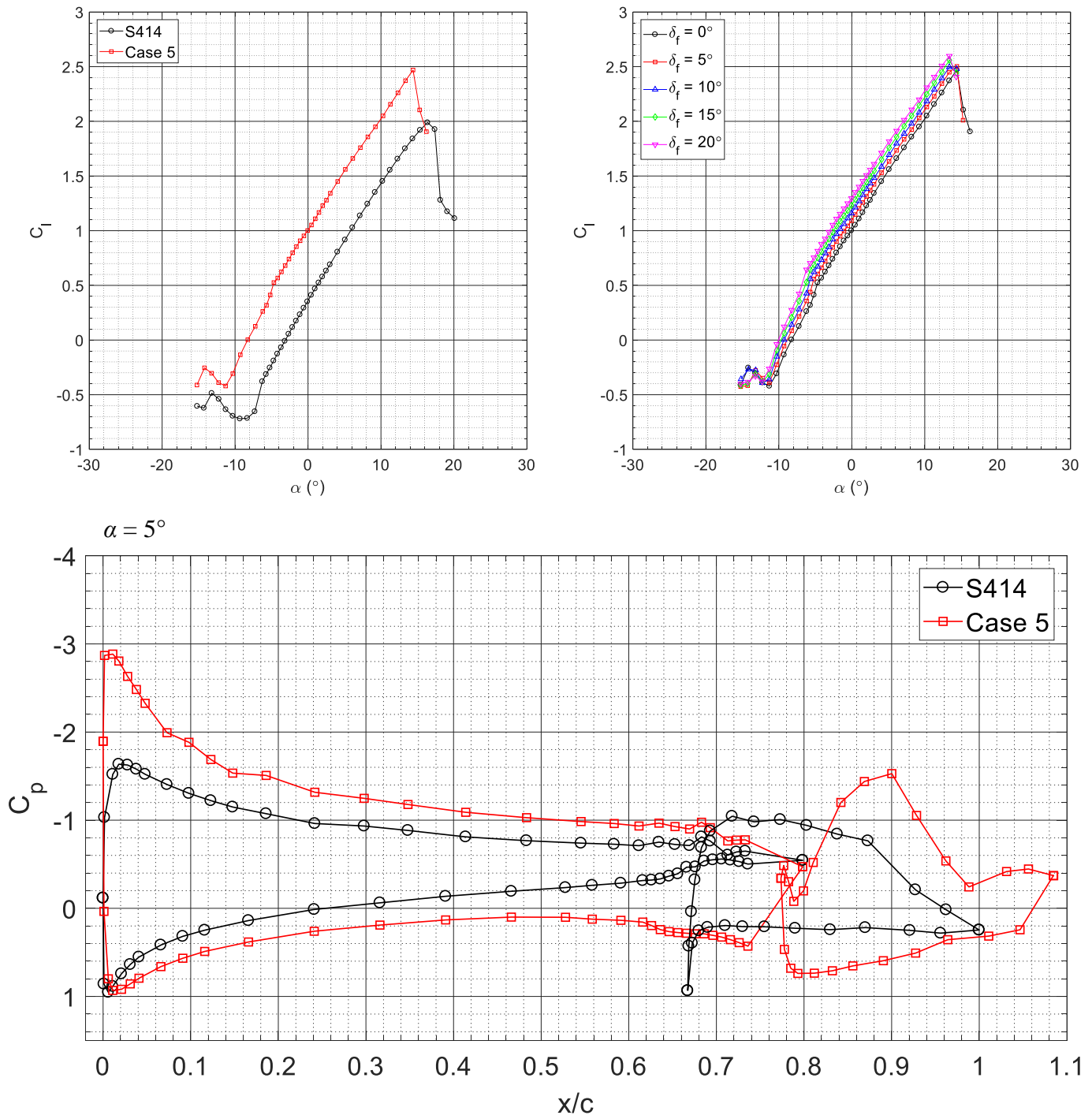


Fig. 3.24 Performance comparison between the S414 airfoil and the Case 5 rigging at $Re = 1.8 \times 10^6$, $M = 0.18$.

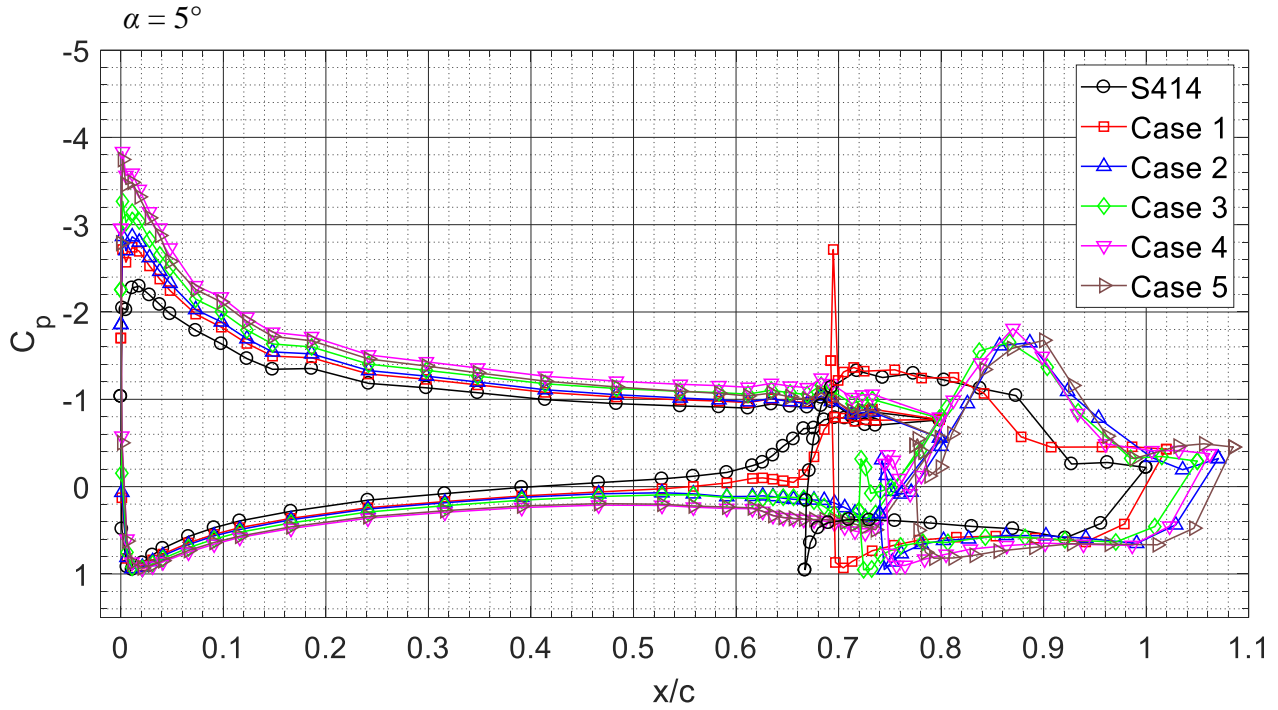
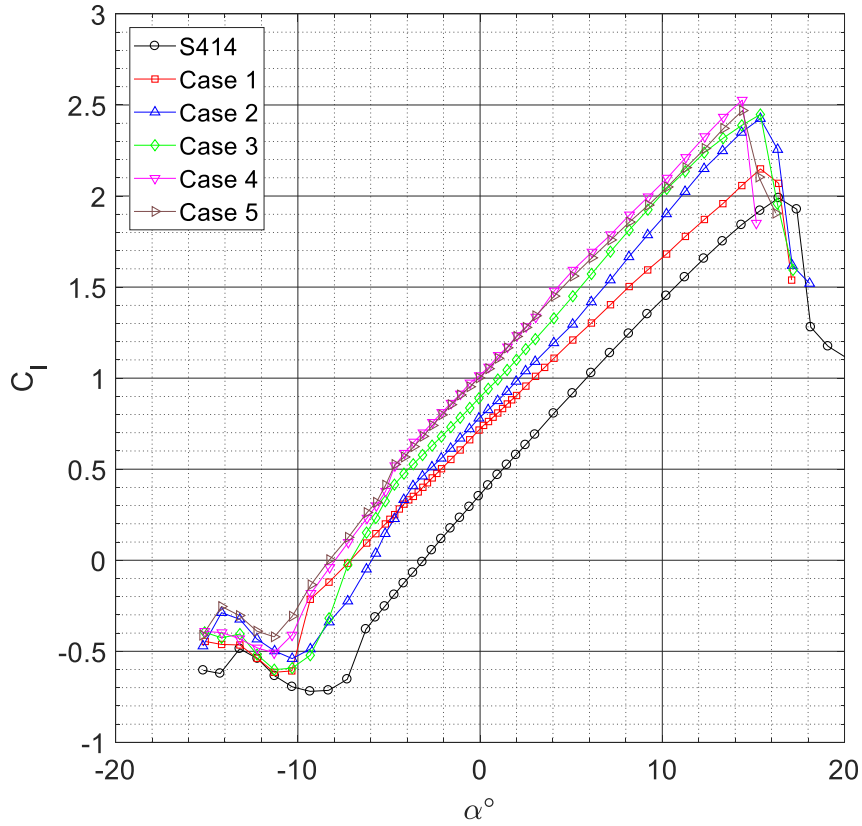


Fig. 3.25 Performance between the S414 and the alternate rigging cases for $\delta_f = 0^\circ$ at $Re = 1.8 \times 10^6$, $M = 0.18$.

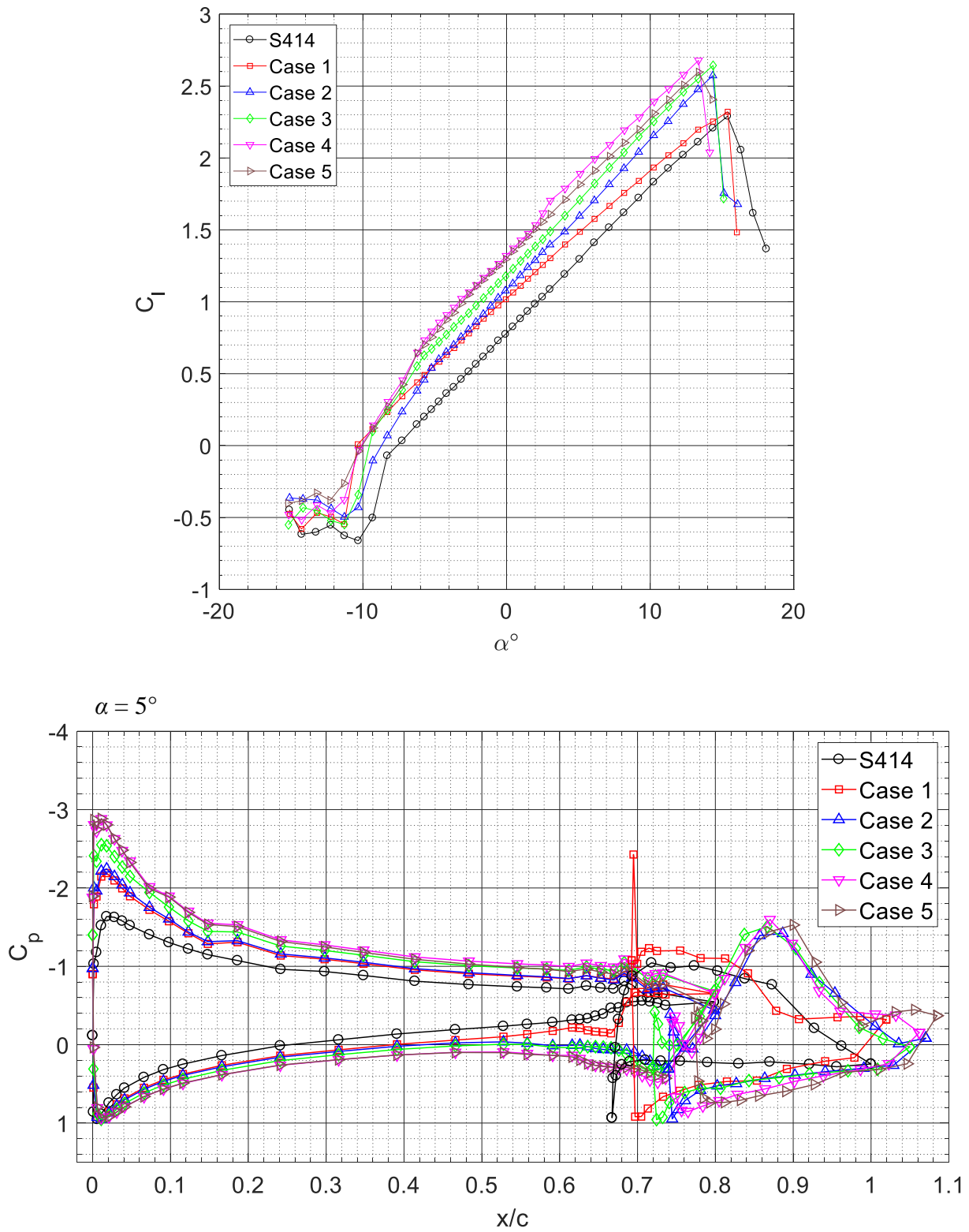


Fig. 3.26 Performance between the S414 and the alternate rigging cases for $\delta_f = 20^\circ$ at $Re = 1.8 \times 10^6$, $M = 0.18$.

Chapter 4

Summary and Conclusions

An experimental and computational study was performed to develop a high-lift configuration of the S414 airfoil model through manipulation of the aft-element position and implementation of a 10% full airfoil chord plain flap on the aft-element trailing edge. The S414 is a slotted natural laminar flow airfoil designed to maintain low profile drag at design conditions and a high $C_{l,max}$. As a result of the geometric airfoil shaping required to achieve these design goals, the S414 has an abrupt leading-edge stall. This study was motivated by a desire to explore the feasibility of using the aft element as an unconstrained high-lift device by investigating the governing physics behind the flow interactions between the fore and aft element.

The effects of repositioning the S414 aft element were first analyzed computationally. The two parameters targeted by the repositioning of the aft element were the slot geometry and the dumping velocity, which were found to have the greatest impact on high-lift performance. Parametric and physics-based repositioning schemes were developed using MATLAB, and the computational flow solver MSES was used to generate theoretical performance predictions throughout this investigation. This theoretical study indicated that while both a slot-based and dumping velocity-based repositioning approach improved performance, the alternative aft element positions that targeted the dumping velocity resulted in the largest high-lift performance gains. It was also observed that $C_{l,max}$ generally increased with increasing plain flap deflection for all

alternative aft-element positions. However, MSES predicted separation off the hinge point of the plain flap, resulting in lower high-lift performance gains than expected. Four alternative aft element positions were identified from the theoretical results, one that targeted the slot geometry to improve high-lift performance, and three that targeted the fore-element dumping velocity.

An S414 airfoil model was designed and manufactured to experimentally test these alternative rigging cases. All tests were performed in the University of Illinois 2.8 ft × 4 ft low-speed low-turbulence wind tunnel at $Re = 1.8 \times 10^6$, $M = 0.18$. As predicted by MSES, the aft-element positions that targeted the dumping velocity produced the largest gains in high lift performance. When the aft element is positioned such that the flow off the trailing edge of the fore element is discharged into a region of low pressure, the pressure recovery burden of the fore element is lessened, resulting in greater ΔC_p across the fore element. In addition, the air flowing over the aft-element upper surface receives a momentum injection from the air discharged off the fore-element trailing edge, allowing the flow to overcome the adverse pressure gradients present on the aft-element upper surface and remain attached. The aft element is also at a significantly higher angle of attack in these configurations, which also greatly increased ΔC_p across the aft element. The slot-based aft element configuration also resulted in a higher $C_{l,max}$, however separation across the aft element upper surface decreased the lift-curve slope, resulting in a lower $C_{l,max}$ than any dumping velocity-based configuration. The effects of deflecting the plain flap were well predicted by MSES. In general, as plain flap deflection increased, $C_{l,max}$ increased. However, diminishing returns were seen as the flap deflection angle increased until the $C_{l,max}$ values appeared to converge. This was most likely a result of separation increasing with plain flap deflection until the entire plain-flap upper surface was separated. For all cases and plain flap settings, the abrupt leading edge stall characteristic was only amplified, and never became more docile.

A fifth case was developed based on the experimental results of the first four cases. Using empirical methods, the gap and overhang of the aft element were modified with the goal of reducing the adverse pressure gradient seen on the leading edge of the aft element when configured in the Case 4 setting. The resulting fifth case was tested experimentally and demonstrated similar performance gains to the dumping-velocity based riggings. However, the fifth case only marginally decreased the adverse pressure gradient on the leading edge of the aft element when compared to Case 4, and as such was outperformed by Case 4.

Chapter 5

Uncertainty Analysis

This chapter summarizes the procedure used to calculate the experimental uncertainties associated with the results from the current investigation and presents example uncertainty values for experimentally-acquired data. Kline & McClintock³³ and Airy³⁴ describe a measurement's uncertainty as a “possible value that an error may have”. In order to properly assess the scatter associated with experimental results over multiple trials, uncertainty analysis is essential³⁵. To provide more informative experimental results, two forms of uncertainty are typically assessed. The first is precision (or “random”) error, which occurs randomly and provides inconsistent and irregular deviation from the mean. The second is bias (or “fixed”) error, which occurs as a result of uncertainty associated with the measurement capabilities of the equipment or the accuracy of calibration. These errors are typically repeatable and consistent.

The precision uncertainty (U_X) in a set of N measurements of the variable X having a mean (\bar{X}_N) can be calculated as described in Moffat³⁵ by using,

$$U_X = \frac{tS_{(N)}}{\sqrt{N}} \quad (5.1)$$

where t is the Student's t statistic associated with the desired confidence interval and the number of samples N , and S_N is the standard deviation of the measurement set used to calculate the mean value X_N . Note that Eq. (5.12) assumes that N measurements of variable X create a Gaussian distribution. For this investigation, N was sufficiently large such that the precision uncertainty was small and could be ignored.

Experimental results (R) that are not directly measured can be calculated from several independently measured variables (x_i) as follows,

$$R = R(x_1, x_2, \dots, x_n) \quad (5.2)$$

The bias uncertainty (U_R) associated with this experimental result can be expressed by taking the square root of the sum of the squares of the corresponding uncertainty components of each variable³³ using,

$$U_R = \sqrt{\left(\frac{\partial R}{\partial x_1} U_{x_1}\right)^2 + \left(\frac{\partial R}{\partial x_2} U_{x_2}\right)^2 + \dots + \left(\frac{\partial R}{\partial x_n} U_{x_n}\right)^2} \quad (5.3)$$

The resulting uncertainties associated with the experimentally derived flow conditions, pressure coefficients, and performance coefficients were calculated using this method.

5.1 Uncertainty in Performance Measurements

5.1.1 Uncertainty in Flow Conditions

The following section outlines the equations used to calculate the uncertainties associated with the flow conditions at which the experiments were run. These parameters include freestream dynamic pressure, atmospheric density, dynamic viscosity, freestream velocity, and Reynolds number. A detailed derivation of the subsequent equations generated from these expressions can be found in Ansell³⁶. Example uncertainty values for these variables computed at a 95% confidence level can be seen in Table 5.1.

$$U_{q_\infty} = \sqrt{\left(\frac{\partial q_\infty}{\partial(P_{ss} - P_{ts})} U_{(P_{ss} - P_{ts})}\right)^2} \quad (5.4)$$

$$U_{\rho_{amb}} = \sqrt{\left(\frac{\partial \rho_{amb}}{\partial P_{amb}} U_{P_{amb}}\right)^2 + \left(\frac{\partial \rho_{amb}}{\partial T_{amb}} U_{T_{amb}}\right)^2} \quad (5.5)$$

$$U_{\mu_{amb}} = \sqrt{\left(\frac{\partial \mu_{amb}}{\partial T_{amb}} U_{T_{amb}}\right)^2} \quad (5.6)$$

$$U_{U_\infty} = \sqrt{\left(\frac{\partial U_\infty}{\partial q_\infty} U_{q_\infty}\right)^2 + \left(\frac{\partial U_\infty}{\partial \rho_{amb}} U_{\rho_{amb}}\right)^2} \quad (5.7)$$

$$U_{Re} = \sqrt{\left(\frac{\partial Re}{\partial U_\infty} U_{U_\infty}\right)^2 + \left(\frac{\partial Re}{\partial \rho_{amb}} U_{\rho_{amb}}\right)^2 + \left(\frac{\partial Re}{\partial \mu_{amb}} U_{\mu_{amb}}\right)^2 + \left(\frac{\partial Re}{\partial c} U_c\right)^2} \quad (5.8)$$

5.1.2 Uncertainty in Pressure and Performance Coefficients

Uncertainty analysis was also performed on the pressure and performance coefficients using the equations detailed in this section. These coefficients include C_p , C_l , C_d , and C_m . A detailed derivation of the subsequent equations generated from these expressions can be found in Collazo³⁷. Example uncertainty values for these variables computed at a 95% confidence level can be seen in Table 5.2.

$$U_{C_p} = \sqrt{\left(\frac{\partial C_p}{\partial(P_s - P_{ts})} U_{(P_s - P_{ts})}\right)^2 + \left(\frac{\partial C_p}{\partial q_\infty} U_{q_\infty}\right)^2} \quad (5.9)$$

$$U_{C_l} = \sqrt{\left(\frac{\partial C_l}{\partial C_n} U_{C_n}\right)^2 + \left(\frac{\partial C_l}{\partial C_a} U_{C_a}\right)^2 + \left(\frac{\partial C_l}{\partial \alpha} U_\alpha\right)^2} \quad (5.10)$$

$$U_{C_d} = \sqrt{\left(\frac{\partial C_d}{\partial q_\infty} U_{q_\infty}\right)^2 + \left(\frac{\partial C_d}{\partial c} U_c\right)^2 + \left(\frac{\partial C_d}{\partial P_{0,\infty}} U_{P_{0,\infty}}\right)^2 + \sum_{i=1}^{n_{rake}-1} \left(\frac{\partial C_d}{\partial P_{0,w}} U_{P_{0,w}}\right)^2} \quad (5.11)$$

$$U_{C_{m_c/A}} = \sqrt{\left(\frac{\partial C_{m_c/A}}{\partial C_{mLE}} U_{C_{mLE}}\right)^2 + \left(\frac{\partial C_{m_c/A}}{\partial C_l} U_{C_l}\right)^2} \quad (5.12)$$

5.1.3 Chapter 5 Tables

Table 5.1 Example uncertainties for the test conditions of the S414 airfoil model experiments at $Re = 1.8 \times 10^6$ and $\alpha = 5^\circ$

Parameter	Reference Value	Absolute Uncertainty	Relative Uncertainty (%)
c	18 in	± 0.005 in	± 0.0278
α	4.984°	$\pm 0.02^\circ$	± 0.4013
$q_{\infty,Setra}$	0.32108 psi	± 0.000771 psi	± 0.2400
$q_{\infty,PSI}$	0.3227 psi	± 0.001425 psi	± 0.4417
P_{amb}	14.49 psi	± 0.008 psi	± 0.0552
T_{amb}	$536.6^\circ R$	$\pm 1.8^\circ R$	± 0.3355
ρ_{amb}	2.267×10^{-3} slugs/ft ³	$\pm 7.604 \times 10^{-6}$ slugs/ft ³	± 0.3355
μ_{amb}	3.837×10^{-7} lb-s/ft ²	$\pm 1.259 \times 10^{-9}$ lb-s/ft ²	± 0.3281
U_∞	202.0 ft/sec	± 0.3388 ft/sec	± 0.1677
Re_c	1789819	± 8934	± 0.4991

Table 5.2 Example uncertainties for the airfoil pressure and performance coefficients of the S414 airfoil model experiments at $Re = 1.8 \times 10^6$ and $\alpha = 5^\circ$

Parameter	Reference Value	Absolute Uncertainty	Relative Uncertainty (%)
C_p 5 psi ($x/c = 0.12$)	-1.2714	± 0.012489	± 0.9823
C_p 1 psi ($x/c = 0.61$)	-0.7443	± 0.005443	± 0.7314
C_l	0.9879	± 0.003847	± 0.3894
C_m	-0.1679	± 0.000886	± 0.5279
C_d	0.01324	± 0.000295	± 2.2319

Appendix A

Additional MSES Material

The computational flow solver MSES was used quite heavily throughout this investigation. This appendix contains additional information and details about the use and practices of the MSES suite of programs as experienced by the author.

A.1 Sample Input/Run Files

This section contains sample run files and input files used throughout this study. As MSES was mostly interfaced with using MATLAB, several functions were developed within MATLAB to assist in the operation and execution of MSES. One such function was created that accepted airfoil coordinates, flow conditions (Re , M , etc.), and boundary conditions, directly interfaced with MSES to generate single point performance predictions, then returned desired airfoil performance coefficients such as C_l , C_d , and C_m . Another function accepted similar inputs, but instead would run a polar sweep across multiple values of a given parameter. These MATLAB functions were used in all analysis programs used to study the alternate rigging configurations. Sample input files created by these functions when performing the slot-based re-rigging analysis are seen in Fig. A.1 - Fig. A.5. Note that the input files have been annotated for clarity.

A.2 MSES Tips

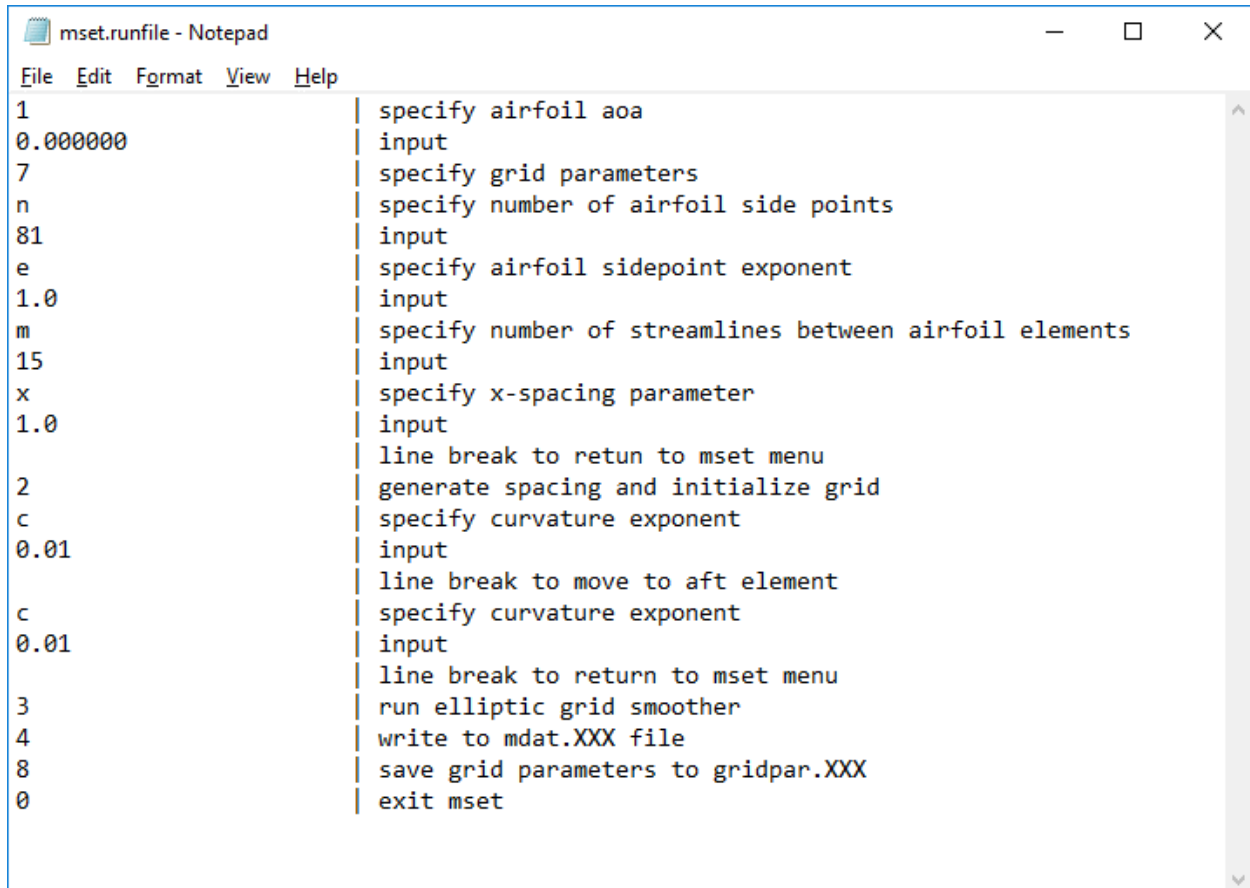
The following list contains tips for operating the MSES suite of programs based on the author's experience, as well as recommendations provided by other individuals consulted with throughout the research program. This list is not claimed to be comprehensive or robust, but is instead a compilation of observations and knowledge obtained throughout this study.

- Like all flow solvers, MSES is sensitive to variations in Reynolds number. Sometimes finely adjusting the Reynolds number to values close to desired flow conditions will result in a converged solution that can still provide valuable computational insights.
- Due to the use of an intrinsic grid, boundary conditions are applied directly to the streamlines. Troubleshooting the MSES runs for boundary condition issues can be quite challenging, but Ref 14 provides a good overview of how to properly condition the `mSES.XXX` input file.
- Generally speaking, convergence problems usually can be addressed through the gridding menu in MSET. If the user is certain the boundary conditions have been properly configured, then MSET can be used to vary grid parameters to push MSES to its maximum capability.
 - Within the MSET gridding menu, varying the grid point number generally has the greatest impact on solution convergence. MSES is sensitive to the number of nodes (n) used on each airfoil element. If an airfoil has a leading-edge bubble, a fine gridding ($n > 150$) may be required to fully resolve its impact on the airfoil performance. Likewise, complicated multielement geometries seem to converge more readily with a coarse gridding ($n < 100$).
 - The E spacing parameter controls how the airfoil side points are distributed across each element of the airfoil. When $E = 1.0$, the grid point number per element is proportional to the element chord. When $E = 0.0$, the number of grid points on each element is equal. The current study maintained $E = 1.0$ throughout.

- The X -spacing parameter controls the orthogonality of the quasi-normal grid lines. A high X value ($X \geq 0.8$) results in more orthogonal grid lines, which is better suited for transonic simulations. A lower X value results in less orthogonal grid lines, which is better suited for high lift applications.
- If working with a multielement airfoil, it may be necessary to adjust the maximum streamlines between each element. Airfoils with larger gap and overhang generally require more streamlines between each element.
- MSET generates grids based on the airfoil coordinate distribution. If a case has difficulty converging, adding or removing airfoil coordinate points and then redistributing the coordinates may fix the issue.
- When generating the initial inviscid grid in MSET, it is best practice to choose an initial α that does not have a large minimum pressure spike to avoid excursions in the initial solution. If running MSES at an α that would result in a high $C_{p,min}$ is desired, it may be better to create the initial grid at a lower α and converge a solution in MSES, then gradually increase α until the desired setting is reached.
- In this study, it was observed that more uniform airfoil grid point spacing ($C < 1.0$) reduced convergence issues. This can be done using the curvature exponent C in the MSET menu through the “generate spacing and initialize grid” option. Higher C values concentrate the grid points near regions of high curvature.
- When running MSES, its best to start by coarsening the grid, then refining, especially for transonic cases. Doing so can greatly reduce computational expense. It should be noted that the number of grid lines over each element must be odd for coarsening to work.

A final word on MSES – MSES is an extremely useful low order flow solver but can be very challenging to use. There is no substitute for experience and experimentation to use MSES well, and there will be no shortage of frustration and failure. However, once the user becomes more familiar with the unique features and methods of MSES, much can be accomplished.

A.3 Appendix A Tables and Figures



```
mset.runfile - Notepad
File Edit Format View Help
1 | specify airfoil aoa
0.000000 | input
7 | specify grid parameters
n | specify number of airfoil side points
81 | input
e | specify airfoil sidepoint exponent
1.0 | input
m | specify number of streamlines between airfoil elements
15 | input
x | specify x-spacing parameter
1.0 | input
| line break to return to mset menu
2 | generate spacing and initialize grid
c | specify curvature exponent
0.01 | input
| line break to move to aft element
c | specify curvature exponent
0.01 | input
| line break to return to mset menu
3 | run elliptic grid smoother
4 | write to mdat.XXX file
8 | save grid parameters to gridpar.XXX
0 | exit mset
```

Fig. A.1 Annotated MSET run file used to automate grid generation and MSES set up.

```
gridpar.airfoil - Notepad
File Edit Format View Help
81
1.0000000000000000
37
37
21
15
15
1.3000000000000000
2.5000000000000000
1.0000000000000000
0.0000000000000000
0.40000000000000002 0.80000000000000004 1.00000000000000002E-002
0.40000000000000002 0.80000000000000004 1.00000000000000002E-002
1.000000 1.000000 1.000000 1.000000 0.000000 0.000000
1.000000 1.000000 1.000000 1.000000 0.000000 0.000000
```

Fig. A.2 Grid parameter file generated using MSET.

```

m ses.airfoil - Notepad
File Edit Format View Help
3 4 5 7 | Boundary Conditions
3 4 5 7 | Boundary Conditions
0.170 2.0 -5.0 | MACH CL ALFA
4 2 | ISMOM IFFBC
1.50e+06 9.000 | REYN NCRIT KTRTYP
1.0 1.0 1.0 1.0 | XTR1 XTR2 ...
0.990 1.200 | MCRIT MUCON

```

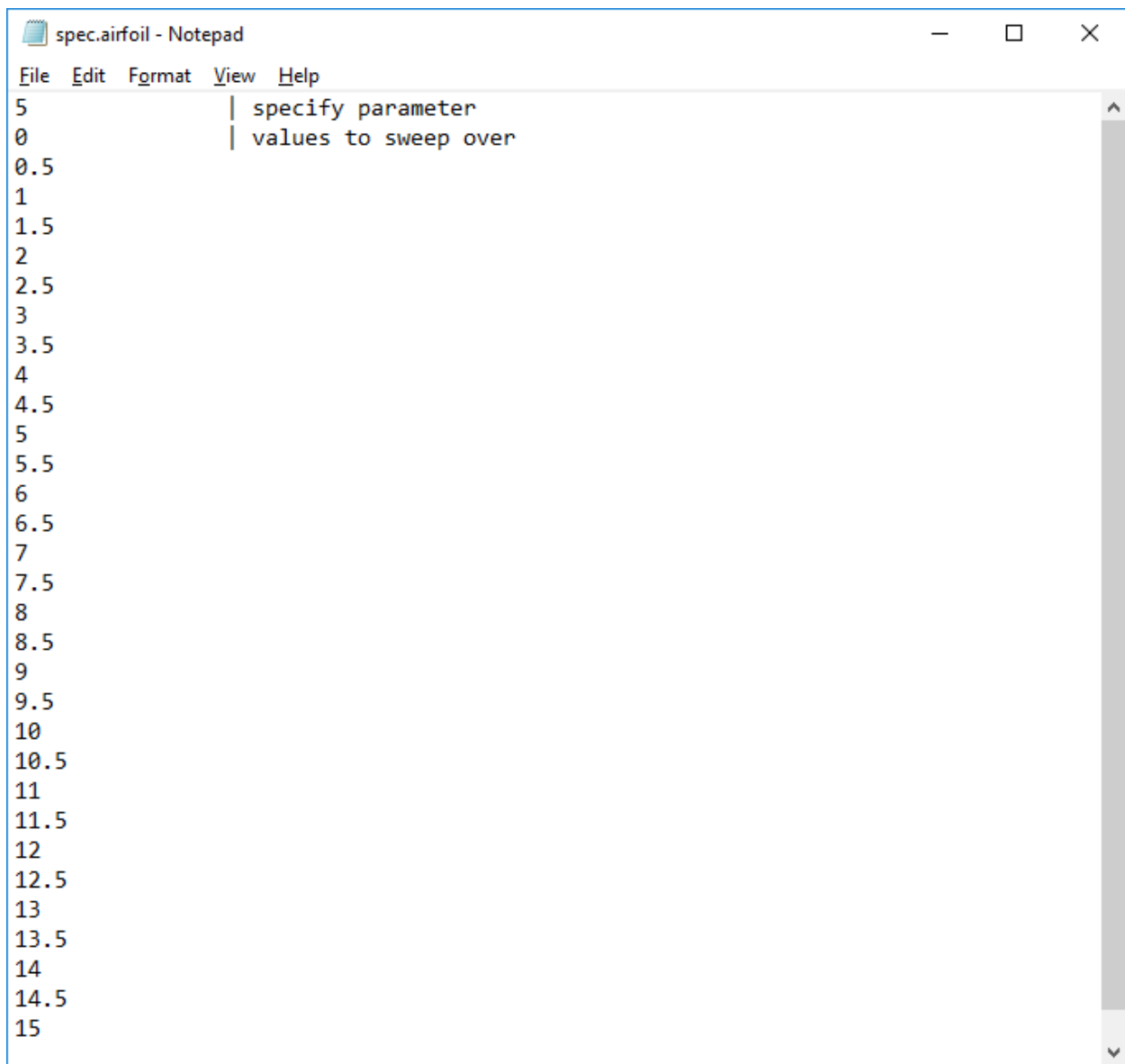
Fig. A.3 Sample mses.XXX input file containing example boundary conditions.

```

m ses.runfile - Notepad
File Edit Format View Help
-15 | coarsen grid
+20 | refine grid
50 | iterate 50 times
50 | iterate 50 times
50 | iterate 50 times
50 | iterate 50 times
0 | exit mses

```

Fig. A.4 Annotated run file used to execute the flow solver MSES.



```
spec.airfoil - Notepad
File Edit Format View Help
5           | specify parameter
0           | values to sweep over
0.5
1
1.5
2
2.5
3
3.5
4
4.5
5
5.5
6
6.5
7
7.5
8
8.5
9
9.5
10
10.5
11
11.5
12
12.5
13
13.5
14
14.5
15
```

Fig. A.5 Sample spec.XXX input file used to specify the parameter to sweep in MPOLAR.

polar.airfoil - Notepad

File Edit Format View Help

MSES Version 3.08

Calculated polar for: S414_test

1 1 Reynolds number fixed Mach number fixed

xtrf = 1.000 (top) 1.000 (bottom)
Mach = 0.170 Re = 1.500 e 6 Ncrit = 9.000
pi_p = 1.0000 eta_p = 1.0000

alpha	CL	CD	CM	CDw	CDv	CDp	Mach	Re	Top_Xtr	Bot_Xtr		
-2.000	0.4698	0.01425	-0.1927	0.00000	0.01425	0.00951	0.1700	0.150E+07	0.7986	0.7986	0.6939	1.0145
-1.500	0.5173	0.01471	-0.1914	0.00000	0.01471	0.00995	0.1700	0.150E+07	0.7986	0.7986	0.6927	1.0145
-1.000	0.5644	0.01519	-0.1900	0.00000	0.01519	0.01044	0.1700	0.150E+07	0.7986	0.7986	0.6920	1.0145
-0.500	0.6136	0.01560	-0.1890	0.00000	0.01560	0.01085	0.1700	0.150E+07	0.7986	0.7986	0.6915	1.0145
0.000	0.6633	0.01599	-0.1882	0.00000	0.01599	0.01127	0.1700	0.150E+07	0.7986	0.7986	0.6912	1.0145
0.500	0.7325	0.01575	-0.1904	0.00000	0.01575	0.01106	0.1700	0.150E+07	0.7890	0.7986	0.6914	1.0145
0.516	0.7350	0.01573	-0.1905	0.00000	0.01573	0.01104	0.1700	0.150E+07	0.7885	0.7986	0.6914	1.0145
0.546	0.7389	0.01572	-0.1906	0.00000	0.01572	0.01104	0.1700	0.150E+07	0.7873	0.7986	0.6914	1.0145
1.000	0.7997	0.01567	-0.1921	0.00000	0.01567	0.01088	0.1700	0.150E+07	0.7188	0.7986	0.6917	1.0145
1.500	0.8417	0.01762	-0.1900	0.00000	0.01762	0.01175	0.1700	0.150E+07	0.5074	0.7986	0.6913	1.0145
2.000	0.8907	0.01896	-0.1894	0.00000	0.01896	0.01241	0.1700	0.150E+07	0.3679	0.7986	0.6910	1.0145
2.500	0.9413	0.01989	-0.1888	0.00000	0.01989	0.01298	0.1700	0.150E+07	0.2881	0.7986	0.6908	1.0145
3.000	0.9921	0.02075	-0.1883	0.00000	0.02075	0.01353	0.1700	0.150E+07	0.2271	0.7986	0.6907	1.0145
3.500	1.0430	0.02153	-0.1876	0.00000	0.02153	0.01410	0.1700	0.150E+07	0.1828	0.7986	0.6905	1.0145
4.000	1.0939	0.02230	-0.1869	0.00000	0.02230	0.01469	0.1700	0.150E+07	0.1465	0.7986	0.6904	1.0145
6.000	1.2821	0.02570	-0.1828	0.00000	0.02570	0.01784	0.1700	0.150E+07	0.0729	0.7986	0.6882	1.0145
6.500	1.3316	0.02648	-0.1821	0.00000	0.02648	0.01859	0.1700	0.150E+07	0.0619	0.7986	0.6881	1.0145
7.000	1.3806	0.02737	-0.1815	0.00000	0.02737	0.01947	0.1700	0.150E+07	0.0528	0.7986	0.6880	1.0145
7.250	1.4052	0.02771	-0.1812	0.00000	0.02771	0.01984	0.1700	0.150E+07	0.0501	0.7986	0.6880	1.0145
7.500	1.4292	0.02822	-0.1809	0.00000	0.02822	0.02031	0.1700	0.150E+07	0.0453	0.7986	0.6879	1.0145
8.000	1.4774	0.02910	-0.1801	0.00000	0.02910	0.02123	0.1700	0.150E+07	0.0404	0.7986	0.6878	1.0145
8.500	1.5261	0.02989	-0.1795	0.00000	0.02989	0.02209	0.1700	0.150E+07	0.0355	0.7986	0.6878	1.0145
8.750	1.5491	0.03066	-0.1791	0.00000	0.03066	0.02282	0.1700	0.150E+07	0.0304	0.7986	0.6877	1.0145
8.875	1.5608	0.03094	-0.1789	0.00000	0.03094	0.02313	0.1700	0.150E+07	0.0292	0.7986	0.6877	1.0145
9.000	1.5726	0.03113	-0.1787	0.00000	0.03113	0.02334	0.1700	0.150E+07	0.0285	0.7986	0.6877	1.0145
9.250	1.5960	0.03155	-0.1783	0.00000	0.03155	0.02379	0.1700	0.150E+07	0.0273	0.7986	0.6876	1.0145
9.313	1.6018	0.03166	-0.1782	0.00000	0.03166	0.02391	0.1700	0.150E+07	0.0269	0.7986	0.6876	1.0145
9.336	1.6040	0.03170	-0.1781	0.00000	0.03170	0.02395	0.1700	0.150E+07	0.0268	0.7986	0.6876	1.0145
9.377	1.6077	0.03177	-0.1781	0.00000	0.03177	0.02404	0.1700	0.150E+07	0.0266	0.7986	0.6876	1.0145
9.408	1.6112	0.03186	-0.1779	0.00000	0.03186	0.02411	0.1700	0.150E+07	0.0263	0.7986	0.6876	1.0145
9.500	1.6194	0.03204	-0.1777	0.00000	0.03204	0.02430	0.1700	0.150E+07	0.0258	0.7986	0.6876	1.0145
9.750	1.6418	0.03251	-0.1770	0.00000	0.03251	0.02483	0.1700	0.150E+07	0.0240	0.7986	0.6876	1.0145
9.766	1.6431	0.03254	-0.1770	0.00000	0.03254	0.02487	0.1700	0.150E+07	0.0238	0.7986	0.6876	1.0145
9.824	1.6484	0.03267	-0.1768	0.00000	0.03267	0.02500	0.1700	0.150E+07	0.0230	0.7986	0.6876	1.0145
9.846	1.6504	0.03272	-0.1768	0.00000	0.03272	0.02506	0.1700	0.150E+07	0.0225	0.7986	0.6876	1.0145

Fig. A.5 Sample polar.XXX file containing results from polar sweep program MPOLAR.

References

- ¹ Somers, D. M., “*Design of a Slotted, Natural-Laminar-Flow Airfoil for Business Jet Applications*,” NASA CR-2012-217559, 2012.
- ² Pfenninger, W., “*Investigations on Reductions of Friction on Wings, in Particular by Means of Boundary Layer Suction*,” NACA TM 1181, 1947. (Translated from Mitteilungen aus dem Institut für Aerodynamik an der Eidgenössischen Technischen Hochschule Zürich, Nr. 13, 1946.)
- ³ Somers, D. M., “*An Exploratory Investigation of a Slotted, Natural-Laminar-Flow Airfoil*,” NASA CR-2012-217560, 2012.
- ⁴ Michael S. Selig, Mark D. Maughmer, and Dan M. Somers. “*Natural-Laminar-Flow Airfoil for General-Aviation Applications*”, Journal of Aircraft, Vol. 32, No. 4 (1995), pp. 710-715.
- ⁵ Michimasa Fujino. “*Natural-Laminar-Flow Airfoil Development for the Honda Jet*”, 20th AIAA Applied Aerodynamics Conference, Fluid Dynamics and Co-located Conferences, 2002.
- ⁶ Smith, A. M. O., “*High-Lift Aerodynamics*,” Journal of Aircraft, Vol. 12, No. 6, 1975, pp. 501–530.
- ⁷ Rudolph, P.K.C, “*High-Lift Systems on Commercial Subsonic Airlines*”, NASA CR-4746, 1996.
- ⁸ Somers, D. M., and Maughmer, M. D., “*Design and Experimental Results for the S414 Airfoil*,” U.S. Army Research, Development and Engineering Command TR-10-D-112, Aberdeen Proving Ground, MD, 2010.
- ⁹ Eppler, R., “*Airfoil Design and Data*” Springer-Verlag (Berlin), 1990.
- ¹⁰ Eppler, R., “*Airfoil Program System ‘PROFIL07’ User’s Guide*,” Richard Eppler, c.2007.
- ¹¹ Drela, M., “*Design and Optimization Method for Multi-Element Airfoils*,” AIAA Paper 93-0969, Feb. 1993.
- ¹² Coder, J.G., Maughmer, M.D., and Somers, D.M., “*Theoretical and Experimental Results for the S414, Slotted, Natural-Laminar-Flow Airfoil*,” Journal of Aircraft, Vol. 51, No. 6, 2014, pp. 1883-1890.
- ¹³ Maughmer, M.D., Premi, A., Somers, D.M., “*Exploration of a Slotted Laminar-Flow-Control Airfoil Concept*,” NASA grant NNX13AB86A.
- ¹⁴ Drela, M., “*A User’s Guide to MSES 3.05*,” Massachusetts Inst. of Technology, Cambridge, MA, 2007.
- ¹⁵ Neal J. Pfeiffer. “*Slotted Airfoil with Control Surface*”, 2018 Applied Aerodynamics Conference, AIAA AVIATION Forum, (AIAA 2018-3958).

- ¹⁶ Whitcomb, R.T., Clark, L. R., “*An Airfoil Shape for Efficient Flight at Supercritical Mach Numbers*,” Langley Research Center, Langley Station Hampton VA, 1965.
- ¹⁷ Page, C.G., “*Professional Programmer’s Guide to Fortran77*”, University of Leicester, UK, 2001
- ¹⁸ Perry, A.T., and Pomeroy, B.W., “*Geometric Effects on the Performance and Wake Development of a Multielement Airfoil System*,” AIAA Region 3 Student Paper Competition.
- ¹⁹ Drela, M. and Youngren, H., “*XFOIL 6.94 User Guide*,” Massachusetts Institute of Technology, Cambridge, MA, 2001.
- ²⁰ Terry, E.L.N, “*Extension of the Aerodynamic Design Program MSES for the Simulation of Boundary Layer Suction* (Masters Thesis),” Delft University of Technology, 2004.
- ²¹ Drela, Mark, “*Flight Vehicle Aerodynamics*,” MIT Press, 2014.
- ²² White, F.M., “*Viscous Fluid Flow*,” McGraw-Hill International Editions, second edition, 1991.
- ²³ Drela, M., Giles, M.B., “*Viscous-Inviscid Analysis of Transonic and Low Reynolds Number Airfoils*,” AIAA Journal, Vol. 25, No. 10, October 1987.
- ²⁴ Drela, M., “*Implicit Implementation of the Full en Transition Criterion*,” AIAA Paper 2003-4066, 21st Applied Aerodynamics Conference, Orlando, Florida, June 2003.
- ²⁵ Maughmer, M.D., and Coder, J.G, “*Comparisons of Theoretical Methods for Predicting Airfoil Aerodynamic Characteristics*,” U.S. Army Research, Development and Engineering Command TR-10-D-106, Aberdeen Proving Ground, MD, 2010.
- ²⁶ Catalano, F.M., et al., “*Wind Tunnel Wall Boundary Layer Control for 2D High Lift Wing Testing*,” 24th International Congress of the Aeronautical Sciences, 29 Aug - 3 Sept 2004, Yokohama Japan.
- ²⁷ Paschal, K., Goodman, W., McGhee, R., Walker, B., NASA-LaRC, Wilcox, Peter A., “*Evaluation of Tunnel Sidewall Boundary-Layer Control Systems for High-Lift Airfoil Testing*,” AIAA 9th Applied Aerodynamics Conference 23-25 September 1991, Baltimore MD, AIAA Paper 91-3243.
- ²⁸ Jones, B. M., “*Measurement of Profile Drag by the Pitot-Traverse Method*,” Tech. Rep. 1688, Aeronautical Research Council R&M, 1936.
- ²⁹ Schlichting, H., “*Boundary-Layer Theory*,” McGraw-Hill Book Company, New York, 1979.
- ³⁰ Loving, D. L., and Katzoff, S., “*The Fluorescent-Oil Film Method and Other Techniques for Boundary-Layer Flow Visualization*,” NASA Memorandum 3-17-59L, 1959.
- ³¹ Barlow, J.B., Rae, W.H. Jr. and Pope, A., “*Low-Speed Wind Tunnel Testing*,” 3rd Edition, John Wiley & Sons, Inc., New York, 1999.

³² Loving, D. L., and Katzoff, S., “*The Fluorescent-Oil Film Method and Other Techniques for Boundary-Layer Flow Visualization*,” NASA Memorandum 3-17-59L, 1959.

³³ Kline, S. J., and McClintock, F. A., “*Describing Uncertainties in Single Sample Experiments*,” Mech. Eng., 3-8 Jan. 1953.

³⁴ Airy, Sir George Biddle, “*Theory of Errors of Observations*,” Macmillan, London, 1879.

³⁵ Moffat, R.J., “*Describing the Uncertainties in Experimental Results*,” Experimental and Thermal Fluid Sciences, Vol. 1, No. 1, 1988, pp. 3–17.

³⁶ Ansell, P.J., “*Unsteady Modes in the Flowfield about an Airfoil with a Leading-Edge Horn-Ice Shape* (Doctoral Dissertation),” University of Illinois at Urbana-Champaign, Urbana, IL, 2014.

³⁷ Collazo Garcia III, A. R., “*Aerodynamic Characterization of a Griffith-Type Transonic, Laminar Flow Airfoil* (Masters Thesis),” University of Illinois at Urbana-Champaign, Urbana, IL, 2019.